

Chapter 4

Atomization and Granulation

Oleg D. Neikov

Frantsevich Institute for Problems of Materials Science (IPMS), Kiev, Ukraine

Chapter Outline

Introduction	125	Other Methods	173
Water Atomization	128	Impact Atomization	173
Water Atomization Technique	128	Vibrating Electrode Atomization	173
Atomization Mechanism	132	Melt Drop Orifice Technique	173
Powder Characteristics	134	Roller Atomization	175
Particle Size Distribution	135	Plasma Atomization Process	175
Oil Atomization	142	Explosive Atomization	176
Gas Atomization	143	Granulation	177
Gas-Atomizing Units	144	Spray Granulation	177
Process Parameters	148	Spray Drying	178
Models of Gas Atomization	149	Control of Powder Properties	178
Gas-Atomized Powders	158	Water Granulation	179
Other Gas-Atomization Methods	162	Applications	179
Vacuum-Dynamic Atomization	167	References	181
Centrifugal Atomization	167	Further Reading	185
Models of Centrifugal Atomization	167		
Centrifugal Atomization Methods	169		

INTRODUCTION

Because of the ease with which a liquid can be broken up into fine droplets, atomization has become the prevailing mode of powder production of nonferrous metals and their alloys [1]. Atomization allows the manufacture of rapidly solidified metal alloys. The use of rapid solidification of melts to produce new structural and other materials with a complex of properties unachievable by traditional metallurgy is not only a very popular subject of investigation, but also finds a wide industrial application nowadays.

The basic types of atomization processes include (Fig. 4.1):

- Jet atomization of the melt, where a liquid metal is dispersed into droplets by the impingement of high-pressure jets of gas, water, or oil (Fig. 4.1A and B) and plasma torch atomization (Fig. 4.1C).
- Melt spinning centrifugal atomization, where a liquid stream is dispersed into droplets, flakes, or ribbons by the centrifugal force effect of a rotating disc, spinning cup, or spinning roller (Fig. 4.1D).
- Rotating of a consumable electrode (Fig. 4.1E).
- Plasma-transferred arc (Fig. 4.1F).
- Disintegration of liquid metal (Fig. 4.1G).
- Impact atomization of a liquid stream (Fig. 4.1H).
- Ultrasonic atomization, where a liquid metal film is subjected to ultrasonic vibration (Fig. 4.1I).
- Impulse atomization, where impulses are mechanically applied to the melt (Fig. 4.1J).
- Vacuum atomization, where heavily saturated molten metal with a gas is atomized in the vacuum (Fig. 4.1K).
- Drop explosion (Fig. 4.1L).

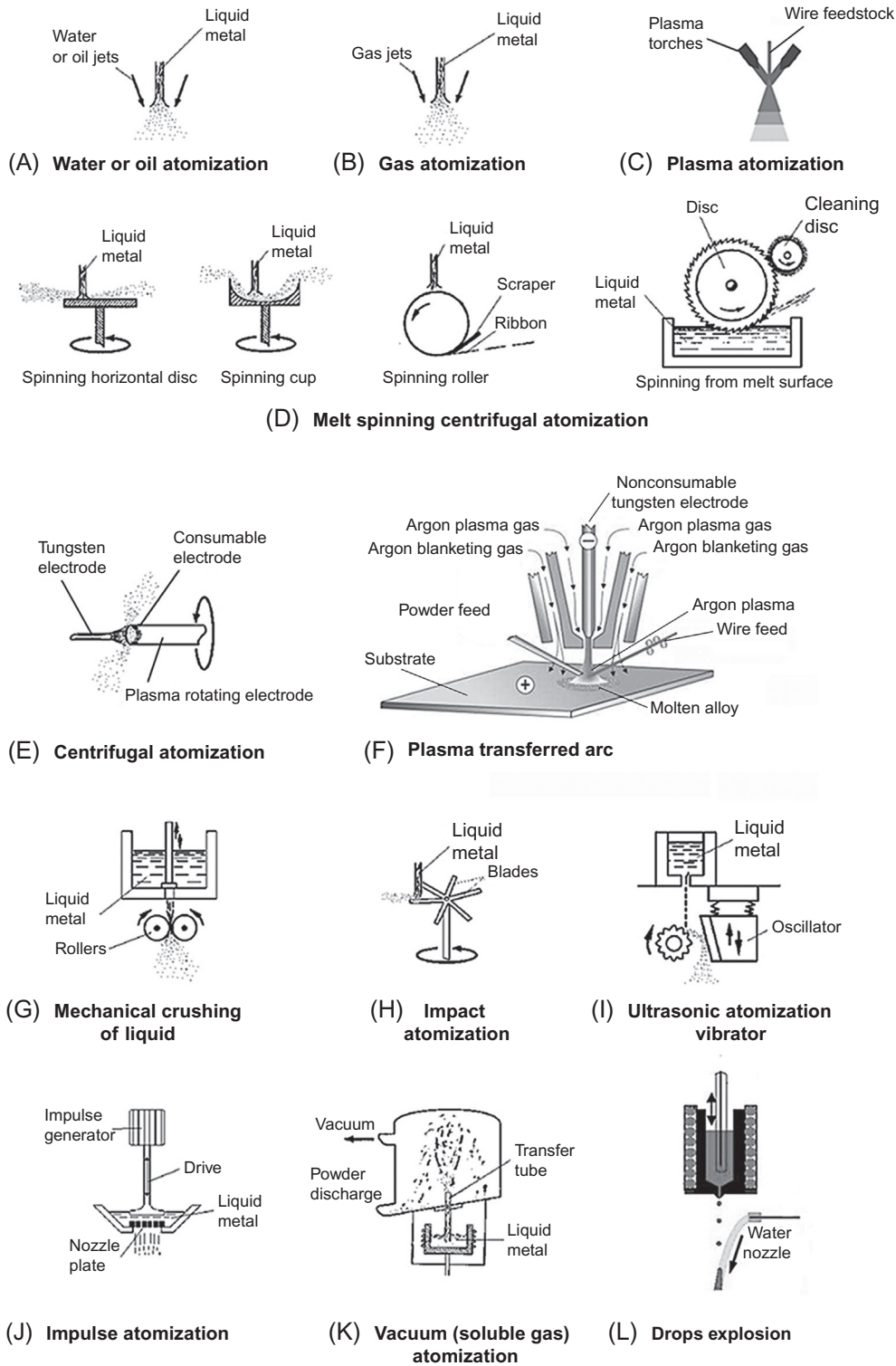


FIG. 4.1 Schematic drawing of atomization processes.

Particle size distribution is one of the most important parameters of powders. The particle size distribution of atomized powders generally follows the lognormal law. This signifies that the particle size distributions form straight or nearly straight lines on the log-probability paper (Fig. 4.2).

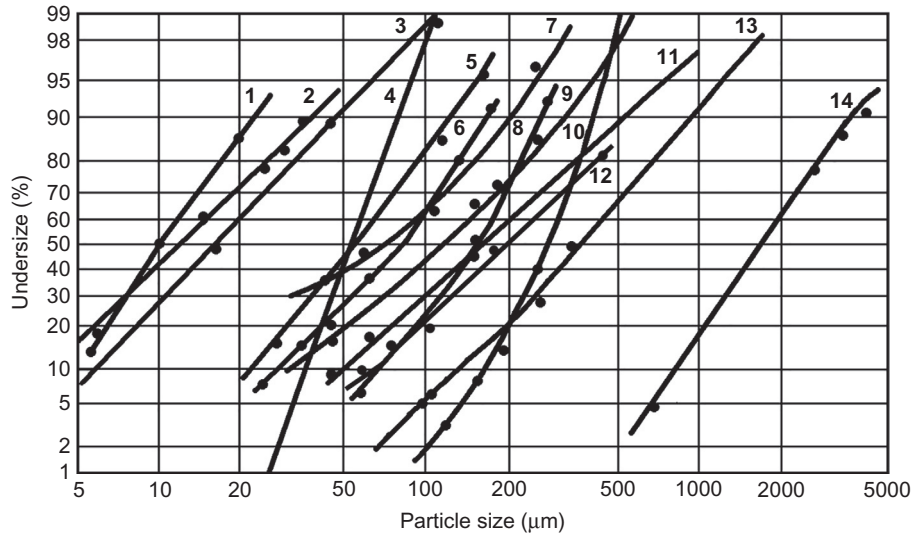


FIG. 4.2 Typical particle size distribution of atomized powders:

Curve No.	Powder	Median Mass Diameter (d_m), μm	Geometric Standard Deviation (σ_g)	References
1	Copper, hot-gas atomized at 4.5 MPa in nitrogen at 500°C	10	2.0	[2]
2	Copper, water atomized at 54 MPa	12.5	2.4	[3]
3	Zinc, gas atomized at 2 MPa	16	2.1	[3]
4	67Pb-33Sn ultrasonically atomized	64	1.31	[3]
5	44.85Al-13.7Fe-28.55Cu-12.9Cr, water atomized at 10 MPa	55	1.83	A*
6	43Al-40Cu17Fe, argon atomized at 0.6 MPa	87	2.48	A*
7	60Pb-40Sn solder, gas atomized at 0.8 MPa	70	2.5	[3]
8	Aluminum, water atomized at 4.8 MPa	150	2.0	A*
9	Bronze, air atomized at 0.5 MPa	120	2.33	[3]
10	Zinc, centrifugally atomized	270	1.4	[3]
11	Zinc, water atomized at 5.5 MPa	170	2.58	[3]
12	Aluminum, water atomized at 2.0 MPa	168.8	2.0	[4]
13	Copper shot, water atomized at 2.0 MPa	280	2.1	[3]
14	Phosphor shot, water atomized at 0.05 MPa	1950	1.9	[3]

A*, author's data.

Granulation of a melt is realized by means of free fall into cold liquid, usually water. During the free fall and by impact with the water surface, the melt stream is broken up into droplets, which then solidify. The melt is caused to flow through a nozzle plate (Fig. 4.1J) in order to obtain granules of a pellet shape. Particulate materials coarser than 1 mm in diameter are conventionally referred to as granules (see Introduction). Thus, several types of conventional atomization processes are useful for granule production.

WATER ATOMIZATION

Water atomization (WA) is used for commercial production of copper, copper alloys, nickel-base alloys, and zinc powders. Water-atomized precious metals are used in dental techniques, sintered electrical contacts, and brazing pastes. WA is less expensive than other methods of atomization. It allows the production of powders within wide yield limits from 1 to 500 kg/min for a single nozzle. The main limitation of WA is powder purity, especially for metals and alloys inclined to oxidation. However, owing to the higher cooling rate of the melt by WA, the average thickness of surface oxides is similar to that in gas-atomized powders. This is realized, in particular, in water-atomized aluminum alloys [5] (discussed in chapter 16 in this book).

Water Atomization Technique

The major components of a conventional water-atomization system are a melting unit, a tundish, an atomizing chamber, a water pumping/recycling system, and the dewatering and drying units. A flow diagram of the typical WA process for copper and copper alloy powder production is shown in chapter 19.

Conventional installations usually operate with water pressure in the range of 5–20 MPa, producing the powders with mass median particle sizes of 30–150 μm . Significantly higher water pressures of 50–150 MPa are used to manufacture finer powders with mass median particle sizes of 1–20 μm . These powders are used for the injection molding process, binders in diamond tools, sintered bearings, paints, coatings, and pastes.

Generally, water atomizer designs are based on “V” configurations with some nozzles (at the minimum two) located symmetrically about the axis of the liquid metal stream (Fig. 4.3).

A representation of the overall processing stages in water atomization is shown in Fig. 4.3. The associated melting process variables include the charge ingredients, atmosphere, and superheat of the melt; the associated atomization stage variables are nozzle diameter, metal stream length, density of metal, surface tension of the melt, viscosity of the melt, water pressure, jet geometry, and apex angle; key variables in the particle solidification stage are the melting point, droplet size, heat transfer, quenching medium, temperature of suspended solid in atomization chamber, and flight path. Basic water-jet configurations are shown in Fig. 4.4.

Typical range of operating conditions in water atomization are as follows [3]:

- Metal flow rate (single nozzle), 1–90 kg/min.
- Water flow rate, 20–380 L/min.

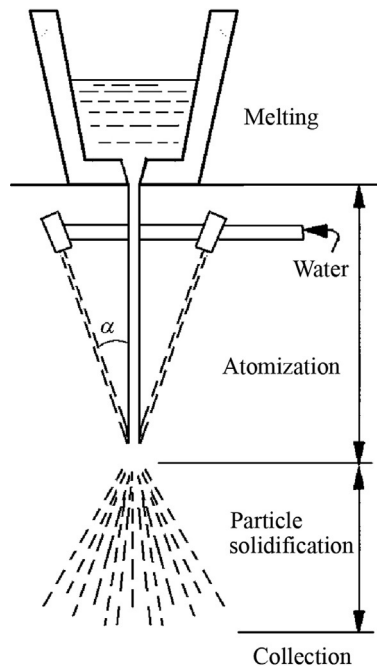


FIG. 4.3 Stages in water atomization.

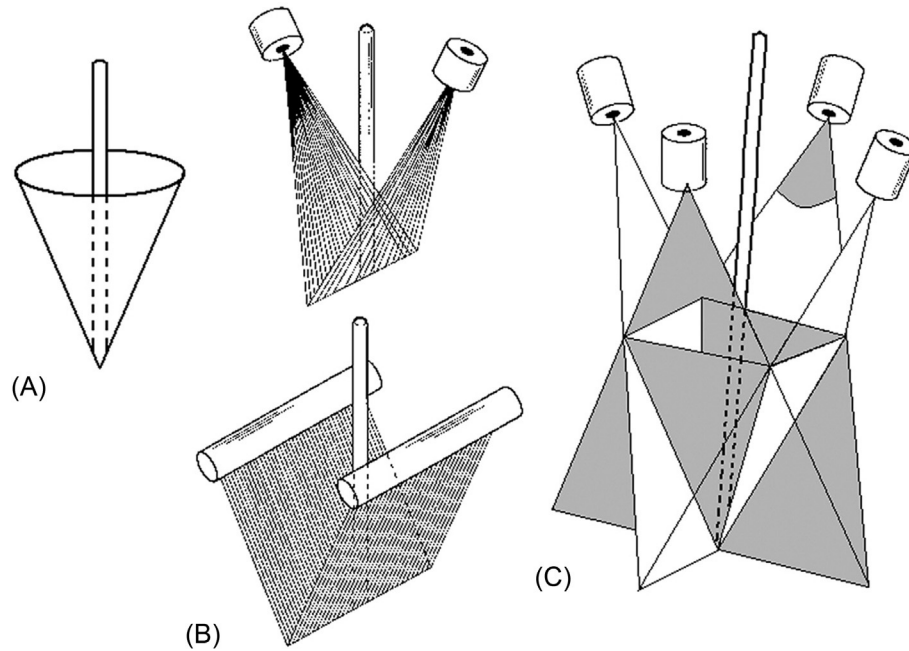


FIG. 4.4 Water jet configurations: (A) annular jet; (B) open V-jets; (C) closed V-jets.

TABLE 4.1 Properties of Several Water-Atomized Powders

Alloy	Operating Parameters				Powder Properties		
	Metal Flow (M) (kg/min)	Water Flow (W) (L/min)	W/M Ratio	Water Pressure (MPa)	Median Diameter r (μm)	Apparent Density (g/mL)	Oxygen (ppm)
Ag ^a	18	100	5.5	50	21	3.4 ^b	—
Al-5Zn-3Mg-0.49Fe ^c	6.5	90	13.8	10	60	0.9 ^d	—
Al-1.3Fe-1.5Cr ^c	7.0	90	12.8	15	45	0.98 ^d	600
Cu-5Cr ^a	27	180	6.7	20	24	3.18 ^b	—
Co ^a	27	180	6.7	20	29	3.28 ^b	—
Au-2Cu ^a	7	40	5.7	13.7	88	—	—
Ag-22Cu-3Zn ^a	9	42	4.7	17.2	72	3.95 ^b	110
Ni-B-Si ^a	24	160	6.7	17.2	51	4.26 ^b	—

^aAll data from V-jet atomizer with 40–50 degrees apex angle, nitrogen purged [3].

^bApparent density for fractions under size 250 μm [3].

^cIPMS atomizer equipped with eight discrete nozzles (details might find below, in this article) (IPMS).

^dApparent density for fractions under size 63 μm (IPMS).

- Water velocity (at nozzle exit), 10–500 m/s.
- Water pressure (at exit or in manifold), 5–150 MPa.
- Metal superheat, 75–170 (above melting point).

Commercial WA plants typically operate with water flow to metal flow ratios between 2/1 and 15/1. Table 4.1 shows the operating conditions for specific powders and their properties.

Atomizers

The atomizers play the main role in ensuring the efficiency of the disintegration of a liquid metal stream. In the literature on atomization, the terms nozzles and jets are often used interchangeably. However, the jet is the stream of liquid or gas that flows out from the nozzle whereas the nozzle is one part of the atomizer. As far as possible, the use of these terms throughout the book is consistent with these definitions.

Though numerous patents for the atomizer design have been filed, only a few types of atomizers are used in most commercial water-atomization units. Atomizer design in most commercial water-atomization units is a variant of either V-jet nozzles (Fig. 4.4) or annular cone-jet nozzles that are concentric with the metal stream. Annular ring nozzles are utilized in some large-capacity plants, but are rarely used elsewhere because they are less flexible and difficult to make than designs based on V-nozzle configurations with two or more discrete openings located symmetrically about the axis defined by the metal stream.

The liquid metal stream typically falls a certain distance (usually about 15–25 cm) before meeting the water jets. A partial vacuum is often created above the impingement point where the water and gas/air sucked by the water streams can disrupt the liquid metal before it actually meets the water jets [6].

A swirl water atomizer for fine powder production has been developed [7]. Fig. 4.5 shows a schematic of high pressure water atomization by “free fall” design and a swirl water jet. This unit allows the production of bronze (Cu-10 mass% Sn) powder with median particle size $7.5\ \mu\text{m}$ and apparent density $2.8\ \text{g/cm}^3$ by water pressure of 83.3 MPa.

Fig. 4.6 shows the effect of the jet configuration apex angle (θ) on the median diameter of swirl water-atomized copper powder (δ_{50}) [8]. The water jets are generated at water pressure 90 MPa with flow rate 5 L/s on the jet swirl angle, $\omega = 0.2\ \text{rad}$

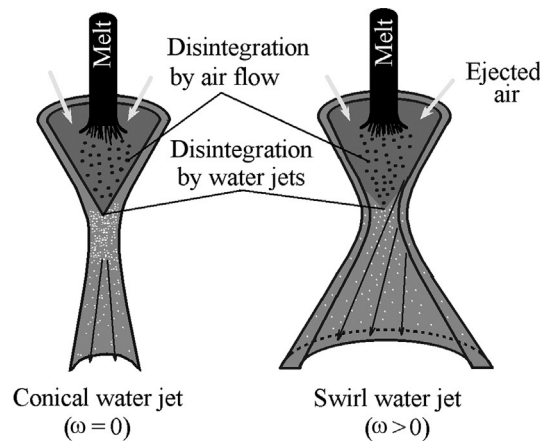


FIG. 4.5 High-pressure water atomization using conical swirl water jet.

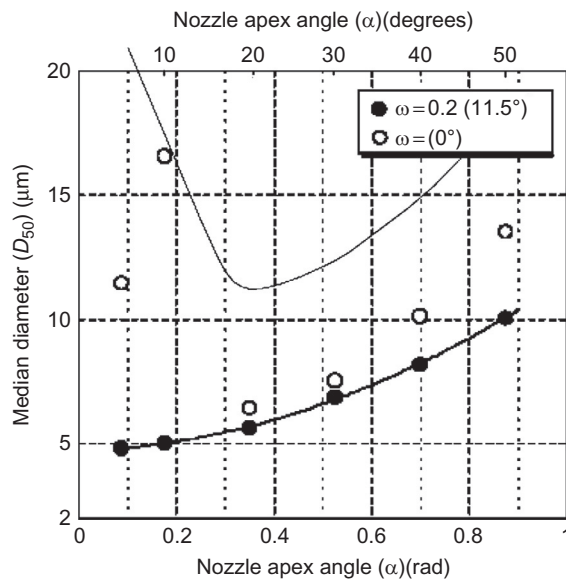


FIG. 4.6 Dependence of powder median diameter on jet apex angle of conical swirl water jet atomizer.

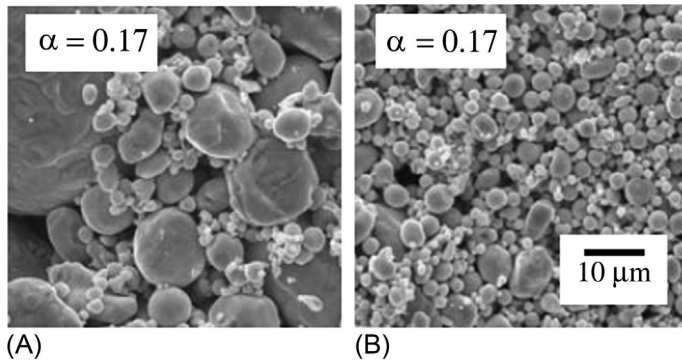


FIG. 4.7 SEM micrographs of copper powders produced by the high-pressure water atomization using conical swirl water jet with apex angle 0.17 rad (≈ 9.7 degrees) and jet swirl angle, $\omega = 0$ (A), that is, common cone water jet configuration, and $\omega \approx 50$ degrees (B), accordingly.

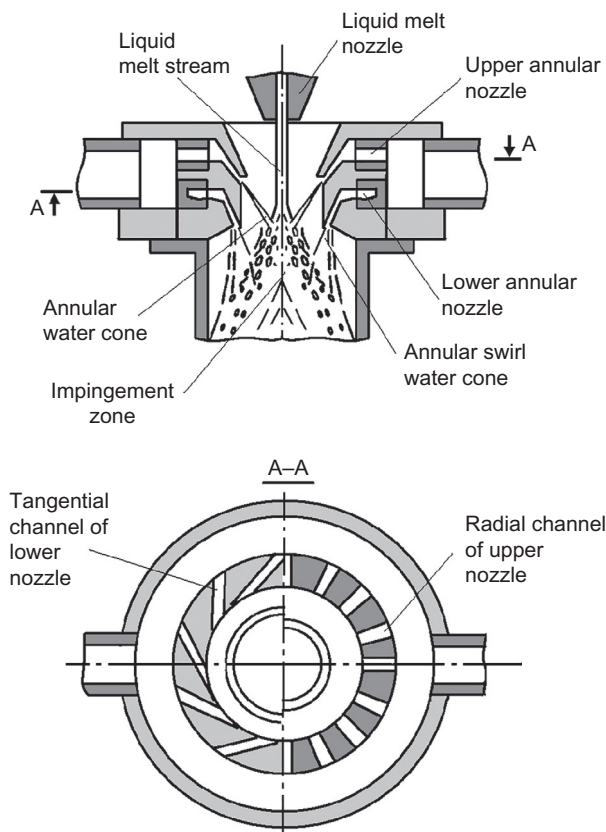


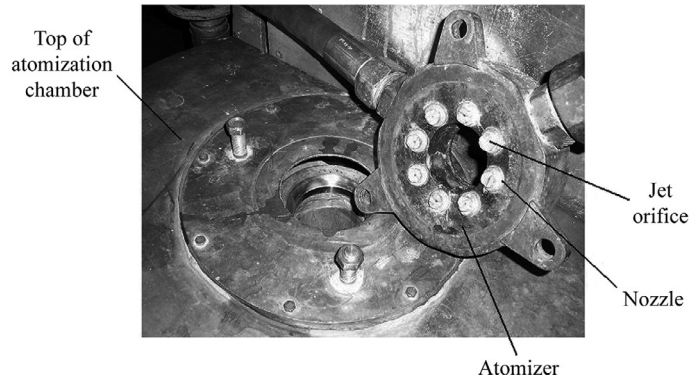
FIG. 4.8 Atomizer with binary water cone configuration.

(≈ 11.5 degrees) and $\omega = 0.0 \text{ rad}$ (0.0 degrees), that is, the usual conical jet configuration. For $\omega = 0.0 \text{ rad}$, δ_{50} of common conical jet configuration atomized powders decreases with decreasing θ down to 0.35 rad , but as θ becomes $< 0.35 \text{ rad}$, δ_{50} increases abruptly with decreasing θ while, by swirl jet configuration for $\omega = 0.2 \text{ rad}$, δ_{50} keeps decreasing with θ decreasing. As can be seen from dependences of δ_{50} on θ in ranges from $\theta = 0.35$ to $\theta = 0.87 \text{ rad}$, δ_{50} for swirl jet configuration is less on one order of magnitude in comparison with the common conical jet configuration. Via the latter, there are many coarse particles with wide size distribution (Fig. 4.7). The particles are spherical or drip-shaped, but with increasing θ up to 0.87 (≈ 50 degrees), the powders become irregular in shape. In the former, there are few irregular aggregates. Almost all particles were spherical and particle sizes decreased with θ decreasing.

Applications for such ultrafine powders include the MIM, sintered filters, conductive pastes, and corrosion-resistant paints.

In atomization installations using an atomizer with a binary water cone configuration (Fig. 4.8) [9], a second convergent water cone performing angular motion relative to the melt stream axis affects the atomized melt droplets. The lower annular

FIG. 4.9 IPMS atomizer equipped with eight discrete nozzles.
Courtesy of IPMS.



nozzle is provided with tangential channels at 27–29 degrees that create a swirl jet configuration. The apex angle of the upper nozzle ranges from 54 to 58 degrees and the lower one ranges from 36 to 40 degrees. The liquid melt outflow orifice is 9 mm.

The IPMS atomizer is equipped with eight discrete nozzles located symmetrically about the axis defined by the metal stream (Fig. 4.9). Four nozzles create a closed V-jet configuration and disintegrate the metal stream upon meeting the atomizing fluid. A second closed V-jet configuration is created by means of four nozzles that impinge on the melt stream at a more acute apex angle than the former. Thus, they meet the melt droplets after the impingement point.

Atomization Mechanism

The water-atomization process is distinguished by a high density of the energy carrier, a high cooling rate, and steam formation in the contact zone between water and melt. High water density $\rho_w \approx 10^3 \rho_{\text{air}}$ leads to an essential increase of impulse linear momentum ($p = mv$) and kinetic energy ($E_k = \frac{mv^2}{2}$) of the energy carrier.

Steam film originating around a drop decreases the heat transfer from drop to surroundings; if the film is disrupted and the contact of melt with water is provided, the cooling rate is appreciably accelerated. The high density of the energy carrier preserves the high velocity of water jets over a long distance that allows a wide range of positional relationships of melt streams and water jets while simplifying the design of hydraulic atomizers.

Liquid metal drops are disintegrated by superheated compressed steam, which is formed on the melt contact surface with water. The breakdown force of the steam film on the melt drop depends on the physical conditions in the contact zone: temperature and density of steam as well as water pressure and volume.

Grandzol and Tallmadge first proposed a mechanism of liquid melt drop formation under impact from the exploding water-steam packet rather than shear for water atomization [10]. This model reflects the dispersed nature of the water and an inverse proportionality between particle size and the normal velocity component of the water, with respect to the metal stream axis. Grandzol and Tallmadge represent the dependence of the mass median particle size (δ_m) on the water drop velocity (v_w) such that:

$$\delta_m = \frac{A}{v_w} = \frac{14,900}{v_w} \left(\frac{1}{n}\right)^{1/3} \quad (4.1)$$

where A is a constant, δ_m is in μm , v_w is in m/s , and n is the number of metal droplets formed from the disintegration of one water droplet. In this equation, water flow rate, water pressure, momentum and energy, jet length, and metal flow are not primary parameters influencing δ_m ; they do, however, affect particle size by influencing water-jet velocities and the number of water droplets. Impingements during atomization can also influence particle size, particle size distribution, and particle shape [11].

From subsequent experimental observations on the influence of the angle between the metal stream axis and the water jet axis on δ_m , it was concluded that the velocity component of the water normal to the liquid metal stream, rather than the velocity component parallel to the liquid metal stream, is the dominant parameter in controlling δ_m [12]. Thus, the refined model [13] gives a relation between δ_m and v_w of:

$$\delta_m = \frac{B}{v_w} \sin \alpha \quad (4.2)$$

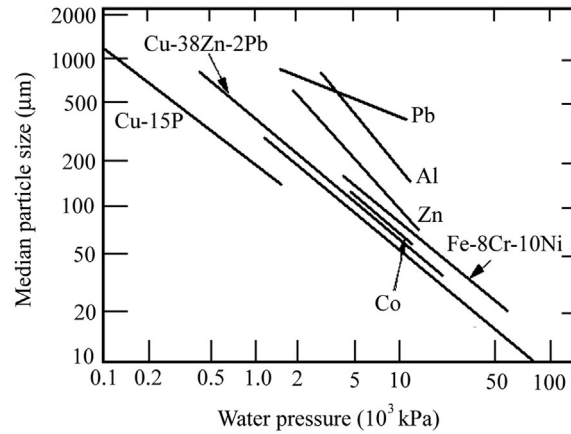


FIG. 4.10 Particle size of water-atomized metals as function of water-atomized pressure.

where δ_m is in μm , v_w is in m/s , α is the angle (in degrees) between the axis of the metal stream and the water jets, and B is a constant. The value of B in conditions of [13] is 2750.

The relation between δ_m and water pressure (p_w) for various metal powders [14] is shown in Fig. 4.10.

Based on the straight log-log plots in Fig. 4.10, the relationship between δ_m and p_w can be expressed as:

$$\delta_m = K p_w^{-m} \quad (4.3)$$

where K and m are constants for the given material and atomization unit. For atomizer modification with two nozzles, when δ_m is in μm , the parameter m is typically in the range 0.6–0.8 for water pressure and from 0.1 to 50 MPa [3].

The values of K are almost one order of magnitude higher for aluminum and zinc than for copper. In practice, this means that for two alloys water atomized under identical operating conditions, δ_m can vary by a factor of about 6. The value K evidently depends strongly on the physical and chemical properties of the molten alloy, in particular viscosity and surface tension. Modification of the surface tension by the atmosphere (steam) to allow the formation of oxides is also expected to be important in terms of disintegration of the molten metal stream.

Increasing the melt superheat reduced δ_m in water atomization, primarily through the effect of temperature on viscosity and surface tension. For example, for zinc, an increase in superheat from 100 to 300 K reduces δ_m from 150 to 100 μm [14]. Similarly, in a cobalt-base alloy, increasing the superheat by about 150 K leads to a decrease in δ_m of about 13.5% [3]. In addition to its effect on particle size, superheat is used as an operating variable to prevent freezing of the alloy in the exit nozzle of the tundish; simultaneously, the superheating leads to an increase of the melt flow rate through the tundish orifice, due to decreasing of melt viscosity.

The apex angle also influences particle size. With the apex angle increasing, the velocity component normal to the metal stream increases. It is shown [13, 15] that δ_m decreases with an increasing angle between the axis of the water jet nozzle and the liquid stream. Grandzol and Tallmadge represent this dependence in the form:

$$\delta_m = \frac{1}{v_w \sin \alpha}$$

However, there is a practical limit to the magnitude of the apex angle. Above about 50 degrees, flow of the molten metal from the orifice of the tundish is impeded by the upward thrust of water, and the incidence of metal freeze-up at higher axis angles, especially at higher pressures (Fig. 4.11). To decrease attenuation in water pressure, a short water-jet length is preferred, but again there are practical limits. It is normally found that using the apex angle to control fineness leads to dangerously unstable conditions. It is better to select a good stable setup with a full shutdown of melt and spray toward the jets and tundish, and then provide the necessary pressure to achieve the desired particle size.

Based on the droplet formation model [16] as the break up of the liquid microjets by instability wavelength and experimental data, Ternovoy [17] derived a semiempirical formula for powder mass median diameter δ_m calculation. The δ_m magnitude is determined subject to all main parameters influencing one, in contrast to Eqs. (4.1)–(4.3) involving the one or two parameters. Ternovoy's formula is represented in the form:

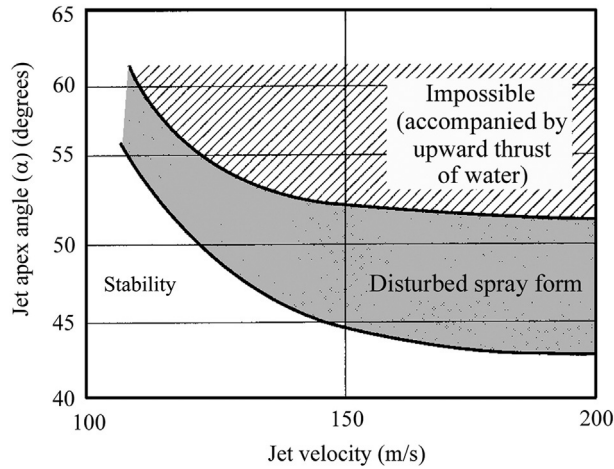


FIG. 4.11 Effect of jet apex angle on stability of water atomization at various water velocities.

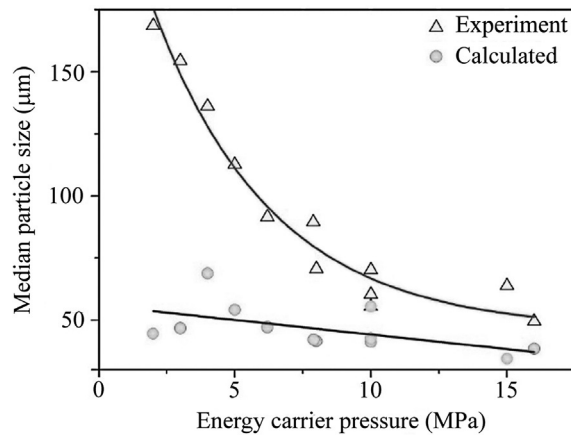


FIG. 4.12 The dependence of powder median diameter on energy carrier pressure by 1273 K temperature.

$$\delta_m = 4.97 \frac{G_{Me}^{1.24} v_w^{0.35}}{G_w^{0.3} \gamma_{Me}^{0.15} D_c^{1.03} \rho_{Me}^{0.56} \rho_w^{0.25} v_w^{0.07} v_w^{0.96} (\sin \alpha)^{0.96}} \quad (4.4)$$

where G_{Me} is the melt mass flow (kg/s), v_w is the water jet velocity (m/s), G_w is the water mass flow (kg/s), v_{Me} is the kinematic viscosity of the liquid metal (m^2/s), ρ_{Me} is the density of the liquid metal (kg/m^3), γ_{Me} is the surface tension of the liquid metal (N/m), D_c is the liquid metal squirt diameter (m), ρ_w is the water density (kg/m^3), v_w is the kinematic viscosity of the water (m^2/s), and α is the jet's apex angle.

The experimental and calculated dependence curves of the powder mass median diameter magnitudes on powder pressure in the 2.0–16.0 MPa range by 1273 K temperature, according to study [4], are shown in Fig. 4.12. The calculations are made with Eq. (4.4). The process parameters and physical quantities by median diameter calculation were in the following range: G_{Me} (0.033–0.1 kg/s), G_w (1.33–3.2 kg/s), v_{Me} (7.52×10^{-7} – $12.3 \times 10^{-7} m^2/s$), v_w (97–137 m/s), ρ_{Me} (2235–2357 kg/m^3), and v_w ($1.4 \times 10^{-6} m^2/s$).

The calculated median diameter volumes are similar to actual sizes by high-pressure volumes (Fig. 4.12). The difference is grown by decreasing the water pressure, and at 2.0 MPa the calculated particle sizes are diminished three times less than in the actual values.

Powder Characteristics

Particles of water-atomized powder generally have an irregular shape with a pronounced uneven surface as compared with gas-atomized powders. For high-yield, low-cost production, and safely engineering, water atomization usually is preferred over gas atomization, providing powder characteristics are compatible with the application.

Particle Size Distribution

Generally, water-atomized powders exhibit lognormal size distribution. Typical data for a range of metals and alloys and for differing operating conditions in water atomization are shown in Fig. 4.13. Deviations from linearity using log normal-probability coordinates usually indicate operational instability, sampling errors, or loss of fines. Minimum values of standard deviations (σ) are normally in the range 1.8–2.3, with some alloys on the low end of this range, for example, Cr-Ni-Mo and Fe-Si. For aluminum alloys (Fig. 4.14) and the alloys that contain aluminum and chromium, which form refractory oxides, the values of σ are typically higher, namely 2.0–3.0. The standard deviation is calculated by:

$$\sigma = \frac{\delta_{84.1}}{\delta_{50}} = \frac{\delta_{50}}{\delta_{15.9}} \quad (4.5)$$

where δ_{50} , $\delta_{84.1}$, and $\delta_{15.9}$ correspond to the particle sizes at the 50%, 84.1%, and 15.9% cumulative weight percent levels, respectively. Thus, the main influence on standard deviation, once a good and stable atomizing jet set-up is ensured, appears to be melt chemistry.

The large effect of the atmosphere is observed in work [18]. In fact, it is confirmed [3] that if copper is atomized with a large dissolved oxygen content, the powder is much finer. Thus, the large difference between nitrogen and air atmosphere may be due to this effect. Similarly, the chemistry may be directly influencing standard deviation. The generally lower values of standard deviation at lower metal flow rates reflect the importance of collisions in broadening the size distributions. Fig. 4.15 illustrates the effect of pouring temperature for water-atomized aluminum and copper powders [4, 6]. The influence of the discharged melt temperature elevation on the atomized powder granulometric composition is characterized by the increase in powder dispersibility. The powder median size decreased from close to 90 μm up to nearly 40 μm by the discharged melt temperature elevation from 963 to 1273 K by the 14 MPa water jet pressure. This is explained by increasing the temperature head and heat flow density and, as result, the heat transfer coefficient expansion, and on the other hand increasing the liquid metal disintegration efficiency due to the surface tension decrease.

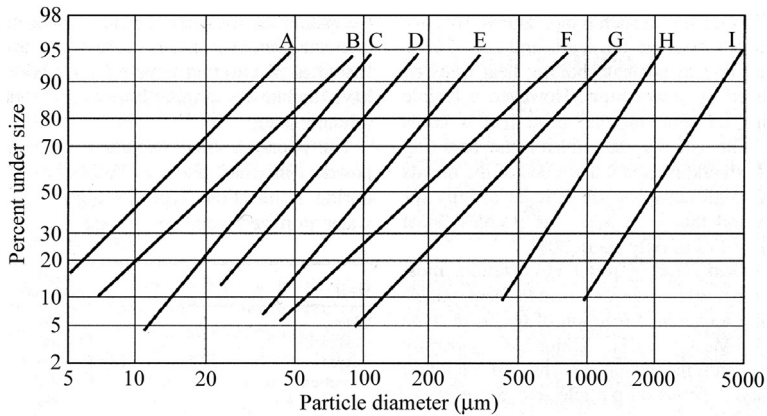


FIG. 4.13 Typical water-atomized particle mass size distribution.

	Alloy and Water Pressure	δ_{50}	σ
A	Copper atomized at 54 MPa	12	2.40
	18Cr-10Ni-2.5Mo stainless steel atomized at 50 MPa	20	2.40
C	Fe-15Si atomized at 20 MPa	40	1.70
D	M2 high-speed steel atomized at 140 MPa	55	2.11
E	Fe-45Si for welding electrodes atomized at 4 MPa	100	1.70
F	Zinc for alkaline manganese batteries atomized at 5.5 MPa	180	2.34
G	Copper shot atomized at 2.0 MPa	400	2.30
H	15% phosphor copper shoot atomized at 0.15	800	1.76
I	15% phosphor copper shoot atomized at 0.05	2000	1.75

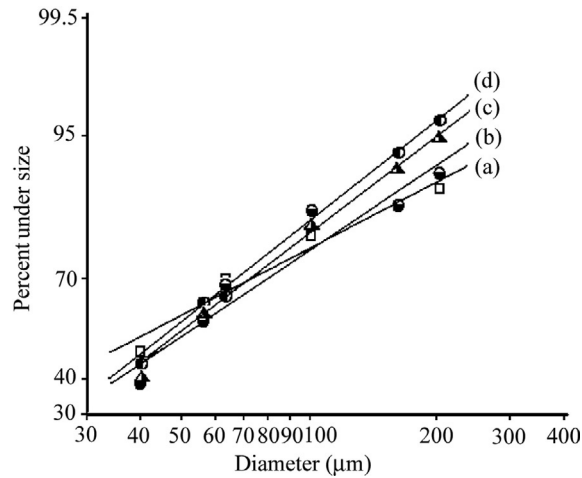


FIG. 4.14 Typical particle mass size distribution of water-atomized aluminum alloys:

	Alloy and Water Pressure	δ_{50}	σ
(a)	Al ₉₄ Fe _{2.0} Cr _{2.0} Ti _{2.0} alloy atomized at 15 MPa	40.5	2.96
(b)	Al ₉₄ Fe _{2.5} Cr _{2.5} Ti _{0.7} Zr _{0.3} alloy atomized at 15 MPa	46	2.83
(c)	Al ₉₄ Fe _{4.1} Cr _{1.3} Zr _{0.6} alloy atomized at 15 MPa	43	2.51
(d)	Al ₉₄ Fe _{4.1} Cr _{1.3} Ti _{0.47} Zr _{0.13} alloy atomized at 15 MPa	42	2.5

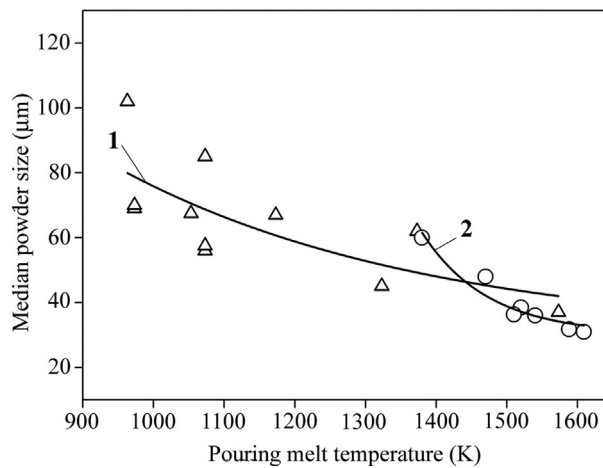


FIG. 4.15 Effect of pouring temperature on distribution of water-atomized aluminum and copper powder. (1) aluminum powder (metal stream diameter 7 mm, water flow 5 kg/s, water pressure 14 MPa), air atmosphere; (2) copper powder (metal stream diameter 4 mm, water flow 5.3 kg/s, water pressure 13.2 MPa, atmosphere nitrogen).

It is appropriate to mention here that each commercial water atomization unit has its own feature operating characteristics. However, well-established proprietary empirical relations give a high degree of predictability in terms of operating conditions and powder properties, in particular, particle size.

Particle Shape

The shape of water-atomized powder particles can vary appreciably. Most water-atomized powders are somewhat irregular in shape. Certain alloys can be produced with a spherical or near-spherical shape, exhibiting apparent densities about 50% of theoretical while others can be sponge-like and extremely irregular in shape, in which case apparent densities are as low as 10%–15% of theoretical.

During melt atomization, the irregular liquid metal drops under action of the surface tension forces tend to a spherical shape, the surface of which is minimal for a certain volume that corresponds to minimum free energy. At that, in prognostication of the particle shape, a determining index is the ratio of spheroidization time τ_{sph} and cooling time τ_{cool} :

$$\varepsilon = \frac{\tau_{\text{sph}}}{\tau_{\text{cool}}} \quad (4.6)$$

The melt drop cooling time τ_{cool} from the discharged melt temperature t_m up to liquidus temperature t_{liq} is expressed [19] by:

$$\tau_{\text{cool}} = d \frac{c_m \rho_m}{6\alpha} \ln \frac{t_m - t_w}{t_{\text{liq}} - t_w} \quad (4.7)$$

where d is the drop diameter (m), c_m is the heat capacity of the liquid metal (J/(kg·K)), ρ_m is the density of the liquid metal (kg/m³), α is the heat transfer coefficient (W/(m²·K)), t_m is the initial temperature of the drop (K), t_{liq} is the liquidus temperature (K), and t_w is the water temperature in the meeting point with the drop (K).

The formula for spheroidization time definition [19] is:

$$\tau_{\text{sph}} = \frac{3\pi^2 \mu}{4V\sigma} (r_{\text{str}}^4 - r_{\text{dr}}^4) \quad (4.8)$$

where μ is the dynamic viscosity of the liquid metal (Pa s), σ is the surface tension of the liquid metal (N/m), V is the drop volume (m³), r_{str} is the strand radius before transformation to drops (m), and r_{dr} is the particle radius after transformation to drop (m).

The melt strand radius formula, which was presented by authors [20] with reference to work [21], is described as:

$$r_{\text{str}} = 0.82d^{1.09} \sigma^{0.09} \nu^{-0.18} \rho_m^{-0.09}$$

where ν is the kinematic viscosity (m²/s) and ρ_m is the density of the liquid metal (kg/m³).

The definition of the heat transfer coefficient is an involved problem in the calculations of the melt drop cooling time. A heat exchange by melt metal drop cooling is the heat transfer process by water boiling. This process is very complicated and possesses a chaotic character even at a constant heat supply in stationary conditions [22]. Analytical process descriptions are presently absent. The experiment and theory of similarity with the dimensional analysis have a decisive role here.

The heat-exchange process of the melt atomization by high-pressure water jets is complicated by the transience of the liquid drop cooling process and the variable heat current. The picture of heat emission in the moment of drop origination and subsequent cooling is possible to see (Fig. 4.16). In the beginning, because of a very high temperature head Δt and heat current q , exceeding the first q_{cr1} and second q_{cr2} critical heat current density, the heat emission occurs in the film boiling conditions. A drop is enveloped by steam film, considerably reducing the intensity of the boiling heat transfer; then, after

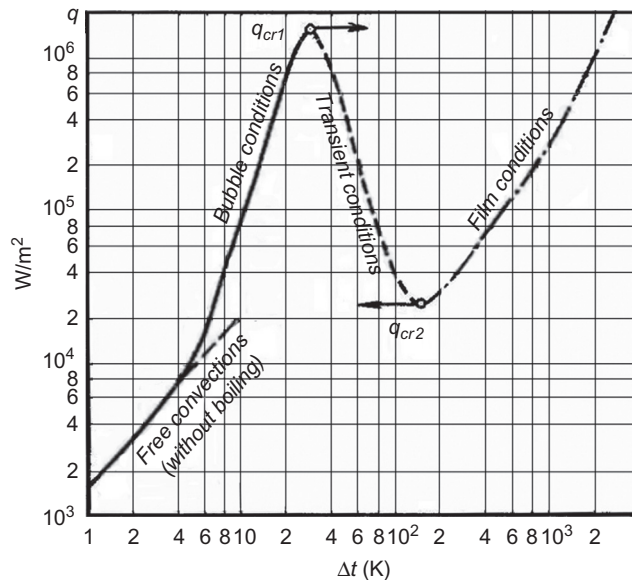


FIG. 4.16 Heat exchange process of the melt atomization by high-pressure water jets.

overcoming q_{cr2} , the cooling rate grows; water begins periodically contacting the drop surface, and the greatest cooling rate is reached in the final cooling stage—bubble boiling conditions, that is, chiefly already after drop consolidation. With such unstable conditions of heat exchange, it is possible to operate only with average heat transfer coefficient values for all cooling drop stages.

The empirical formulas of heat transfer coefficient definition are known for different boiling conditions [22, 23]. However, they are reached by boiling on the body surfaces of cylindrical shapes and plates at atmospheric pressure, that is, for conditions very distant from the heat exchange by high-pressure water atomization of the melt.

The heat transfer coefficient calculated values for well-developed bubble boiling conditions by empirical formulas [23] exceed by 2–3 orders of magnitude the current actual values and the calculated values for film boiling conditions by empirical formulas [22, 23], and exceed by 1.5–2 orders of magnitudes the current actual values. For example, the calculation by Bramley's [23] advanced formula (Eq. 4.9) for the case of an 11.4 μm aluminum melt drop cooling by 963 K pouring melt temperature and 10 MPa water pressure gave a result of $\alpha = 10^6 \text{ W}/(\text{m}^2 \text{ K})$. The above-mentioned formula is expressed as:

$$\alpha = 2.7 \sqrt{\lambda_2 \varphi r \rho_2 w / \Delta t d} \quad (4.9)$$

where λ_2 is the heat conductivity of the steam ($\text{W}/(\text{m K})$); r is the heat of vaporization (J/kg); ρ_2 is the steam density (kg/m^3); w is the velocity of the water jet in the meeting moment with the melt stream (m/s); Δt is the temperature head, assignable as the temperature differential of the melt drop (t_s) and water (t_w) in the meeting point with the drop disconnected by the steam film (K); c_2 is the heat capacity of the steam by the saturation line temperature, $\text{J}/(\text{kg K})$; d is the drop size (m); and $\varphi = 1 + c_2 \Delta t / 2r$. The parameter magnitudes by the calculation are the following: $\lambda_2 = 5.55 \times 10^{-2} \text{ W}/(\text{m K})$; $r = 1.5 \times 10^6 \text{ J}/\text{kg}$; $\varphi = 1.736$; $\rho_2 = 36 \text{ kg}/\text{m}^3$; $w = 119 \text{ m}/\text{s}$; $c_2 = 5.45 \times 10^3 \text{ J}/(\text{kg K})$; and $\Delta t = 405 \text{ K}$.

Thus, the prerequisites [19, 24] about the possibility that the film-bubble heat emission conditions occur in the 923–973 K temperature range and in connection with this, the increasing of heat emission had not been confirmed by study in work [4].

More reliable cooling time data can be gathered using a method for cooling rate definition based on the particle structure [4]. Thus, the cooling rate of melts is estimated with the use of the dendrite parameter, which is equal to the average size of the nondendrite grain [25]. The analysis of the dendrite structure allows one to estimate the cooling rate by the equation:

$$v = (\alpha / \delta)^{1/n}, \quad (4.10)$$

where δ is the measured nondendrite grain in μm ; v is the cooling rate in K/s ; and a and n are constants for aluminum alloys $a = 100$. A value of n is taken in the interval 0.25–0.5 depending on the grain shape, $n = 1/3$ for equiaxed grains (chapter 16 contains details of the analysis of the droplet cooling rate).

Then the average size of the heat transfer coefficient is defined according to the formula (Eq. 4.7). It is used for definition of the heat transfer coefficient values by the various drop sizes at various discharged melt temperatures and water pressures:

$$\alpha = d \frac{c_m \rho_m}{6 \tau_{\text{cool}}} \ln \frac{t_m - t_w}{t_{\text{liq}} - t_w}$$

The dependence of the heat transfer coefficient on the heat flow density in the 953–1273 K temperature range by aluminum water atomization is shown in Fig. 4.17 [4]. The heat transfer coefficient varies from the 10^4 to $5.2 \times 10^4 \text{ W}/(\text{m}^2 \cdot \text{K})$ range, when the heat flow density is increased from 10^7 to $4 \times 10^7 \text{ W}/\text{m}^2$ by 10–14 MPa energy carrier pressure. Such heat transfer coefficient values range with $\pm 5.5\%$ abmodality, can be considered, is not great, whereas the transience of liquid drop cooling process and variable heat current and as well that the cooled particles had various sizes, shape and morphology.

It is significant that the lowest heat transfer coefficient values were reached for large-dimension particles. It can be explained by the more irregular shape and uneven surface of coarse particles, contributing to the steam film rupture and abruption from its particle surface, which results in the abrupt heat dissipation decreasing.

The spheroidization time (τ_{sph}) was calculated via a formula (Eq. 4.8) added by the correction, taking into account the energy carrier density (ρ_w) in the ratio form of the energy carrier density to steam density (ρ_{stm}). That is more reasonable in film boiling conditions than how air density was accepted before. The formula (4.4) with the correction coefficient is written as:

$$\tau_{\text{sph}} = \frac{3\pi^2 \mu \rho_w}{4V \sigma \rho_{\text{stm}}} (r_{\text{str}}^4 - r_{\text{dr}}^4)$$

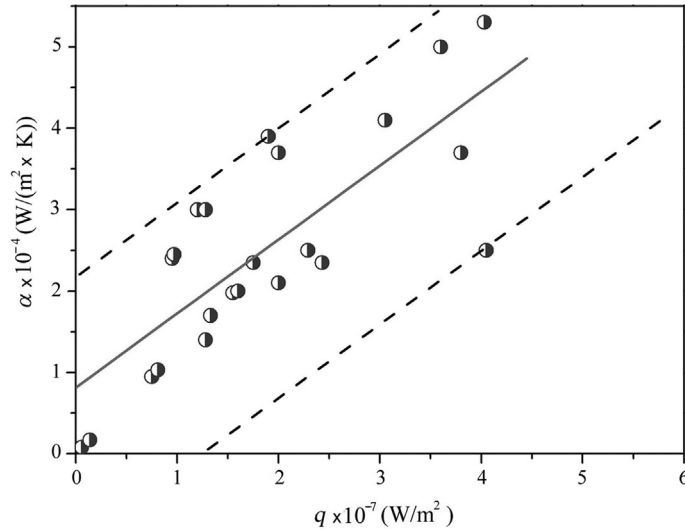


FIG. 4.17 The dependence of the heat transfer coefficient on the heat flow density by the 10–14 MPa energy carrier pressure range.

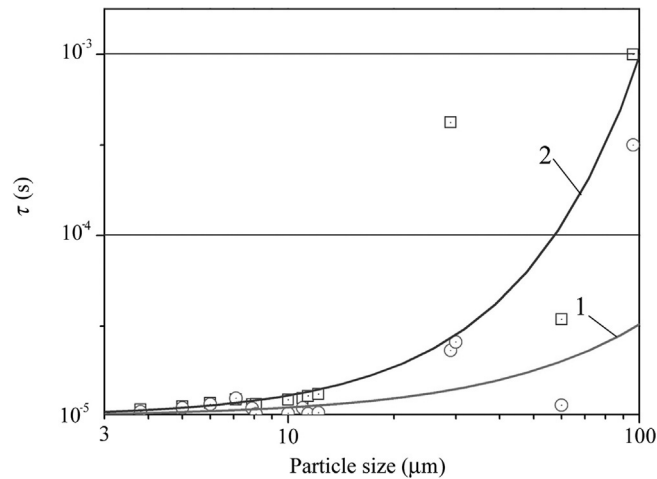


FIG. 4.18 Comparison of (1) $\tau_{\text{cool}}=f_1(d)$ and (2) $\tau_{\text{sph}}=f_2(d)$ dependences for powders made by water pressure in 3–15 MPa range and melt pouring temperature in 960–1620 K range.

The cooling time (τ_{cool}) of the drops up to liquidus temperature is calculated by their cooling rates defined by the experimental dendrite parameter values, according to the above-mentioned method [24] by Eq. (4.10).

The dependence of cooling time on particle size ($\tau_{\text{cool}}=f_1(d)$) and the dependence of spheroidization time on the particle size ($\tau_{\text{sph}}=f_2(d)$) are presented in Fig. 4.18. The approximation curves of these dependences are approached with each other in the course of particle size decreasing and flow together when τ_{sph} is being diminished up to τ_{cool} of the particle's results in particle spheroidization. It occurs with the 5–7 μm drops and smaller dimensions.

Micrographs of the water-atomized aluminum powders, made by melt atomization at 1273 K and pouring temperature in the pressure range from 2.0 to 16 MPa, are shown in Fig. 4.19. Characteristically, the influence of energy carrier pressure magnitude over the particle shape and morphology is not affected notably as both for particles larger 50 μm (Fig. 4.17A and B), when $\tau_{\text{sph}} > \tau_{\text{liq}}$, and lesser sizes particles (Fig. 4.19C and D), when spheroidization time is less, than their cooling time.

The influence of the pouring melt temperature in the 963–1273 K range by 10–14 MPa energy carrier pressure is not observed on the surface relief and shape of the particles, similar to sizes as large as 50 μm (Fig. 4.20A and B) and as small as 20 μm (Fig. 4.20C and D).

Therefore, particles larger than 50 μm have an irregular shape and uneven surface that increases with the particle size growth. In particles <30 –20 μm and with further diminishing of the sizes, the surface irregularities are smoothed and complete spheroidization of the 7–5 μm particles occurs. Thus, the melt drop size is a determinative parameter in the

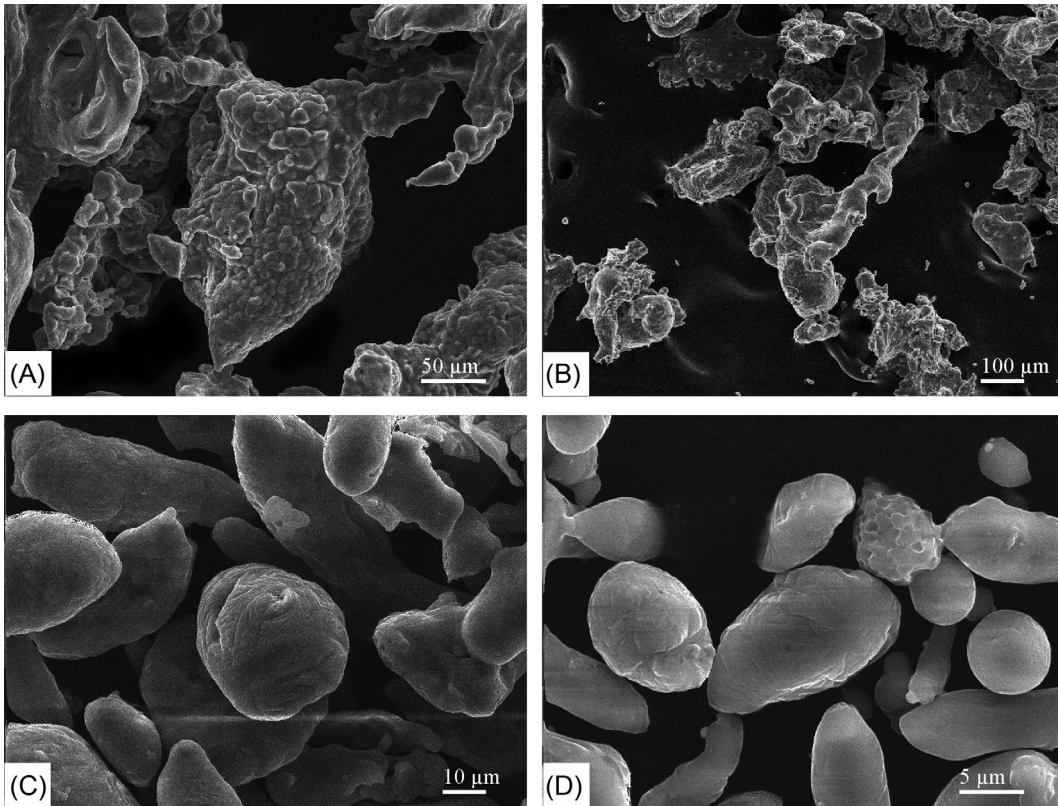


FIG. 4.19 Characteristic shape and morphology of the particles similar in sizes: (A, B) larger 50 μm, (C, D) less 20 μm, made at 1273 K pouring melt temperature and various energy carrier pressure: (A) 3 MPa, (B) 16 MPa, (C) 2 MPa, (D) 6.2 MPa.

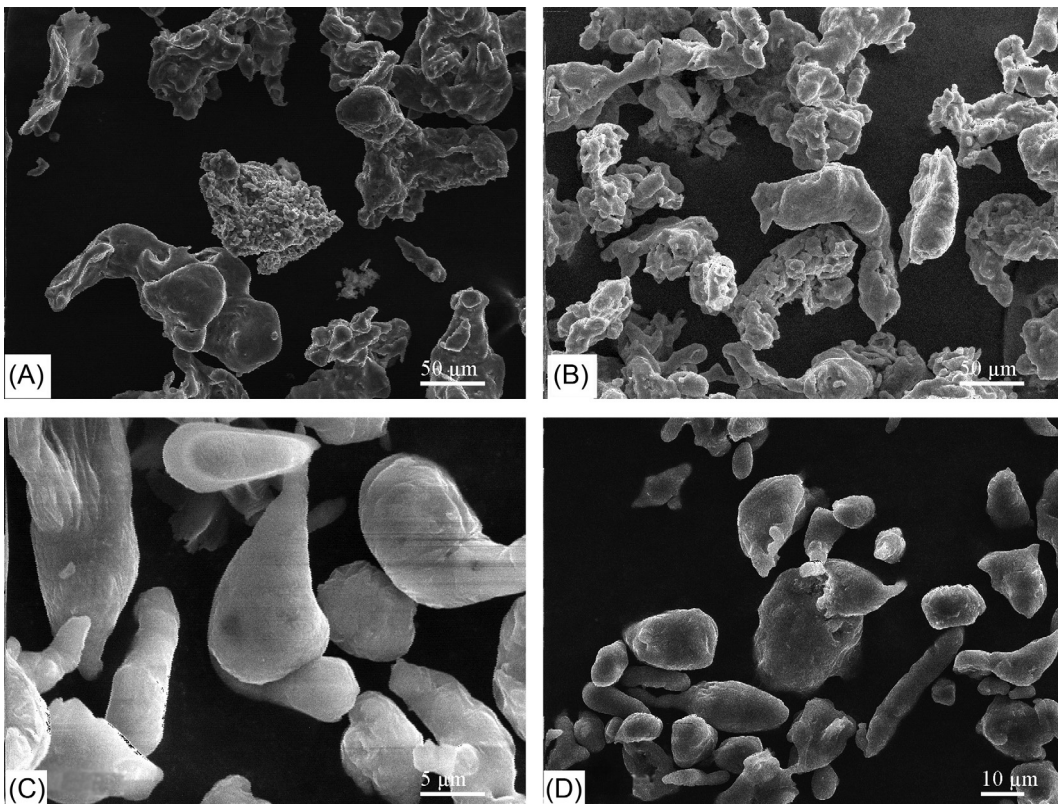


FIG. 4.20 Characteristic shape and morphology of the particles similar in sizes: (A, B) larger 50 μm, (C, D) less 20 μm, made by 10–14 MPa energy carrier pressure and at various pouring melt temperature: (A) 963 K, (B, C) 1273 K, (D) 1273 K.

independent shaping of the current energy pressure range and the pouring melt temperature range while the granulometric composition greatly depends on the energy current pressure and discharged melt temperature.

Lawley [13] summarized that the estimated spheroidization time for a 100 μm diameter droplet to be in the range from 0.1 to 10 μs , depending on the magnitude of surface tension forces. Freezing (solidification) times are of the order of 50–750 μs for elevated temperature aluminum alloys by a pouring melt temperature 1520–1573 K. Thus, solidification times are near to or less than the spheroidization times and water-atomized particles are therefore predicted to be predominantly irregular in shape.

The formation of an oxide film on the surface of the droplet before it is in free fall and able to spheroidize can drastically affect particle shape. Elements that form refractory oxides prevent spheroidization by producing an oxide film with sufficient strength to oppose the forces of surface tension.

Thus, in terms of particle shape, droplets with very short freezing times tend to be more irregular and in turn are associated with low apparent densities. Accordingly, the longer freezing times characteristic of high melting point elements or alloys result in a more spherical particle shape.

Surface Morphology and Internal Structure

Water-atomized powders, along with their irregular shape, typically show a rough surface morphology and are honey-combed. This characteristic is illustrated in water-atomized Al-6.0Zn-0.3Mg-0.3Zr-0.5Mn high strength alloy (Fig. 4.21) and Al-5.0Fe-5.0Cr-2.0Ti-1.0Zr elevated temperature alloy (Fig. 4.22). Their morphology is similar to one of aluminum powders similar in size (Figs. 4.19A and 4.20A). The combination of irregular shape, surface roughness, and porosity is an important feature of water-atomized powders because green strength is enhanced by the mechanical interpenetration of irregular powders during die pressing.

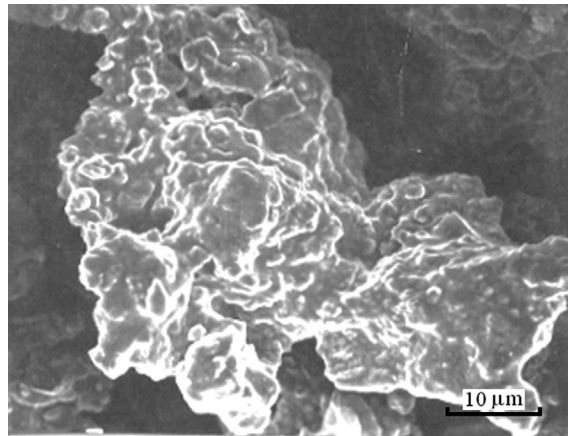


FIG. 4.21 SEM micrograph of water-atomized powder of Al-6.0Zn-0.3Mg-0.3Zr-0.5Mn high-strength alloy.

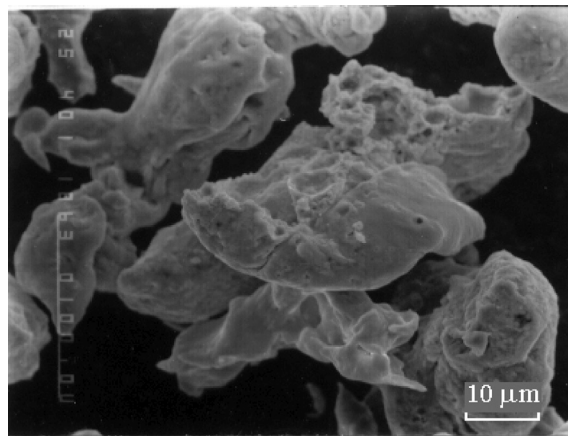


FIG. 4.22 SEM micrograph of water-atomized powder of Al-5.0Fe-5.0Cr-2.0Ti-1.0Zr elevated temperature alloy. Superheat 200 K; diameter of gravity melt stream 7.0 mm.

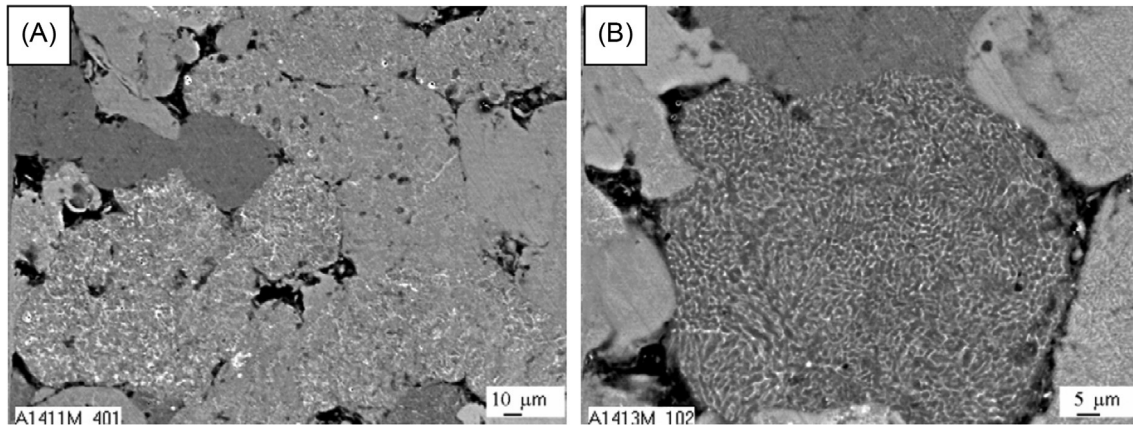


FIG. 4.23 Microstructures of two typical metallographic sections of water-atomized powder particles of Al-Fe-Ce alloy in backscattering electrons with lower (A) and higher (B) magnifications.

Individual particles or even different grains within a powder particle differ in microstructure (Fig. 4.23A). This is caused by differences in solidification behaviors of the solidifying fronts growing into the melt and of primary intermetallic phases distributed in the melt. Most particles exhibit a cellular or nondendritic-like structure with an arm spacing of a few hundred nanometers in colonies a few microns in diameter (Fig. 4.23B). Some other grains show a coarser background network structure where coarse primary intermetallics act as separate growth centers.

In addition to a nondendritic structure, some other areas of individual particles show subdendritic and cellular structures. Such observations can be explained by a significant intensification of the nucleation during crystallization by a deep supercooling of the melt. The nondendritic and subdendritic cell sizes are different for different particles. For example, the calculated cell size values shown in Fig. 4.23B range from 1.2 to 0.94 μm that, in accordance with Eq. (4.10) corresponds to cooling rates from 0.83 to 1.7 $\text{K}/\mu\text{s}$.

Powder Purity

Deoxidation of the melt plays an important role in the atomization process. The oxygen content of water-atomized powder is a function of the free energy of the reaction of the metal with water vapor and also of the reaction kinetics. For many water-atomized powders, oxygen levels are in the range 1000–4000 ppm by weight. The importance of the kinetic effect is exemplified by the appropriate oxygen levels in aluminum or high silicon alloys. In these alloys, a protective oxide film arises on the particle surface, which prevents or retards further oxidation. The surface oxide of water-atomized powders is nonuniform in thickness. Therefore, with water-atomized powders, three-dimensional film islets with a typical thickness of 30–40 monolayers usually cover 30%–70% of the particle surface. The rest is covered by a thin oxide film of three to eight monolayers [26]. Table 4.2 gives the characteristic properties of water-atomized powders, including oxygen content.

The increase of oxygen content can be accommodated by modifying the atomization conditions. For example, the use of inhibitors in combination with the control of the hydrogen ion level and suspension temperature during the atomization process can lead to a decrease in the oxygen content to the level of gas-atomized powders [27]. The Au-Ni brazing alloys normally have oxygen content about 200 ppm. By using inert purging gases in the melting process, the oxygen level is reduced to 150 ppm. Further reductions in the oxygen level to 100 and 40–50 ppm can be achieved by deionized water or by the addition of alcohol to the water. The use of antifoaming agents in the atomizing water can further reduce oxidation and increase the cooling rate [15].

OIL ATOMIZATION

The oil-atomization process should avoid the problem of powder oxidation. In the early 1980s, Sumitomo Metals developed the oil-atomization process for the commercial production of relatively high carbon (0.4 wt%) steel [15]. Oil-atomized powders resembled water-atomized powder in particle size. Their densities are intermediate between water- and gas-atomized powders as the cooling rate is slower and the oxidation much less. However, carbon pickup occurs to an extent depending on metal temperature and the carbide-forming tendency of the melt [28].

TABLE 4.2 Characteristic Properties of Water-atomized Powders

Metal Alloys	Mass Median Particle Size (δ_m) (μm)	Standard Deviation σ_g	Apparent Density (g/mL)	Oxygen Content (ppm)
Ag	37	2.16	3.76	—
Ag-28Cu	32	2.3	3.37	285
Ag-25Sn-5Cu-1Zn	35	2.40	5.11	260
Al-3.92Fe-3.65Cr-3.3Ti ^a	40.5	2.96	1.07	—
Au	130	2.69	7.82	—
Au-20Ni	62	2.9	—	57
Bi	79	3.33	3.58	—
Cd	185	2.00	1.29	—
Cu	46	2.30	3.48	350
Cu	90	2.40	5.07	397
Cu-0.3Mg	31	2.51	2.01	1105
Ni	100	2.10	4.50	645
Ni-5Al	34	2.29	2.85	710
Ni-Cr-B-Si	51	1.69	4.26	—
Pt-10Rb	250	2.80	12.3	—
Sn	160	2.19	1.48	314
Sn	90	2.19	1.23	620
Zn	58	2.05	1.82	—

^aIPMS data.

Lawley A. Atomization. Princeton: Metal Powder Industries Federation Publishers; 2003.

GAS ATOMIZATION

Gas atomization (GA) is the process in which the liquid metal is dispersed by a high-velocity jet of air, nitrogen, argon, or helium. Gas atomization is used for the commercial production of powders of copper, copper alloys, aluminum and its alloys, magnesium, zinc, titanium, titanium alloys, nickel-base alloys, cobalt-base alloys, lead, tin, solder, precious metals, refractory metals, beryllium, etc.

Gas atomization differs substantially from water atomization. The gas-to-metal ratio is the dominant factor in controlling particle size while the pressure of the medium is dominated by water atomization. This fundamental difference is easily explained. In the case of gases, increases in pressure above 0.1 MPa, at which sonic velocity is reached, give very small increments in gas velocity. In contrast, to reach sonic velocity with a water jet, a pressure of nearly 40 MPa is needed and the velocity increases uniformly as the square root of the pressure. Moreover, gas atomization takes place by the action of a continuum on another while in water atomization, a stream of droplets in an entrained gas flow acts on a continuum. Therefore, the density of the water medium is about a thousand times higher than typical gases, giving much greater impact.

Air atomization is used for aluminum, copper, brass, and zinc powder production. Inert gases are used when the oxygen content must be kept low or when atomizing reactive metals such as superalloys and titanium. The worldwide annual tonnage of inert gas-atomized metal powders is much less than for water-atomized powders. The relationship between the shipments of ferrous and nonferrous powders is about 4 to 1. However, in market value terms, aluminum, silver, and zinc are all close to the value of iron powders [1, 29].

Gas-Atomizing Units

Gas-atomizing units exist in a much wider range of designs than water atomizers. The earliest gas atomization was with steam, patented in 1872 by Marriott of Huddersfield. The very simplest design of the atomizer is to let a metal stream fall onto a horizontal gas jet, and this has been used for zinc powder production. The earliest scientific worker in this field seems to have been Professor Hall, founder of the Metals Disintegrating Co. His patent in the late 1920s [30] represents a kind of close-coupled atomizer for aluminum atomization. The basic design shown in this patent is still in use and has yet to be improved in any radical manner. A similar unit developed by VAMI is shown in Fig. 4.24. The atomizing gas is delivered through an annular orifice around the nozzle at the converging angle. The gas flow creates the suction (ejection) effect at the tip of the nozzle that draws the molten metal into the nozzle. The amount of gas delivered by the nozzle is controlled by the size of the air gap and the pressure and temperature of the gas. The rate of metal flow and resultant powder particle size are influenced by the aspirating force, the nozzle metal orifice diameter, and the vertical distance between the nozzle and the molten metal level.

This atomizer design aims to contact the liquid metal stream with the gas is at or close to the gas jet exit plane where the highest jet velocities exist. It leads to an efficient break-up of the liquid, resulting in finer powders, and is the preferred method for aluminum and other low melting point metals. It can be operated vertically upward or downward or in the horizontal position. Careful design of the atomizer is required, however, to avoid the freezing of the metal by the gas jet, which can lead to solidification at the nozzle tip.

Many gas atomizer designs are known. They are classified as free fall, confined or closed nozzles (Fig. 4.25), and internal mixing. The closed nozzle designs are also called close-coupled nozzle designs. For free gas atomization (Fig. 4.25A), the key process variables are similar to those of water atomization (Fig. 4.3). In this atomizer, the liquid metal issues in the form of a stream from a tundish and falls 100–200 mm by gravity. Then it is atomized either by means of a discrete or an annular directed at the point of meeting with the metal stream. This method is easy to operate but is not suitable for making fine powders. In the “internal mixing prefilming” atomizer type, the gas and liquid metal are mixed together before expanding into the atomizing chamber [31].

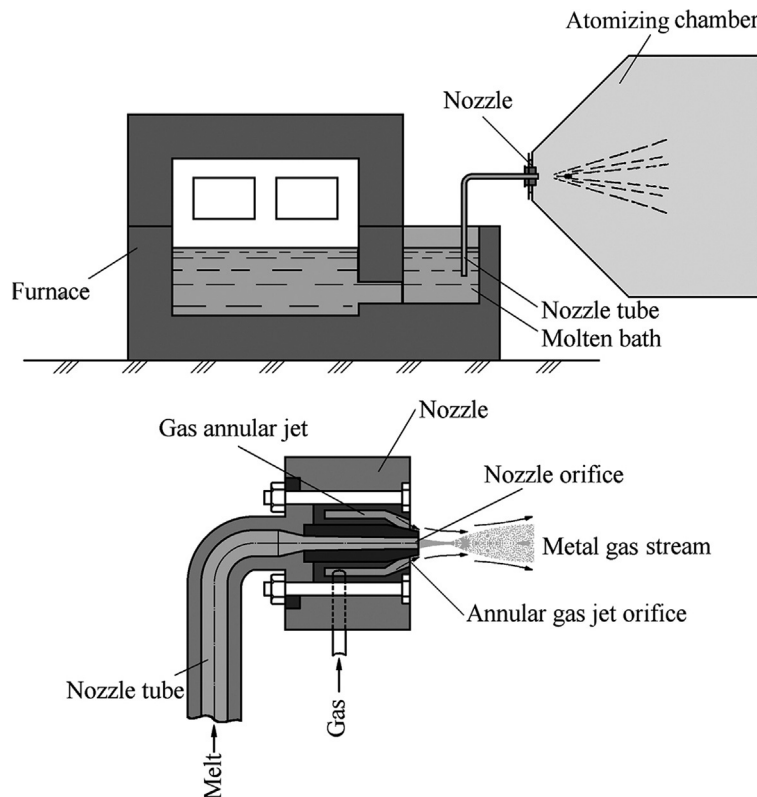


FIG. 4.24 VAMI ejection nozzle design with horizontally molten metal stream.

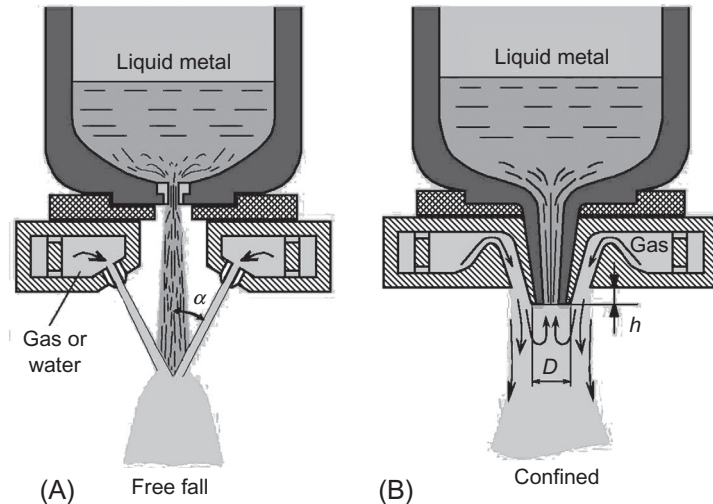


FIG. 4.25 Atomizer designs of two types: (A) free-fall design (gas or water) and (B) confined-nozzle design (only gas). Design characteristics: α , angle formed by free-falling molten metal and atomizing medium jet; D , diameter of confined molten metal nozzle end; h , protrusion length of metal nozzle.

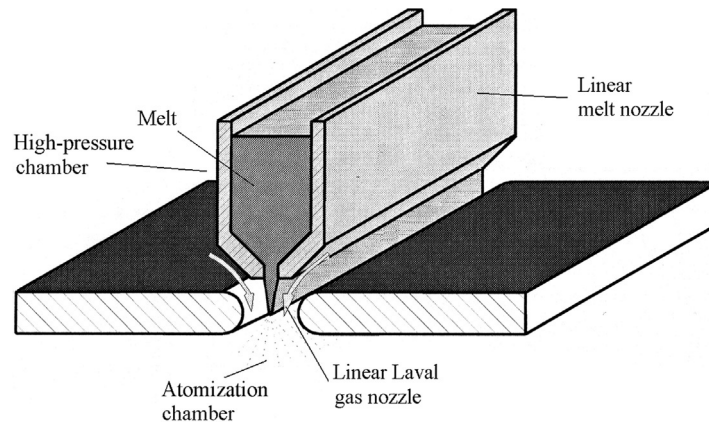


FIG. 4.26 Simplified drawing of the WIDEFLOW confined linear nozzle design.

Confined Nozzle Designs

This nozzle design (Fig. 4.25B) makes it possible to increase the yield of median particle size powder (40–60 μm) by maximizing the gas velocity and density at the meeting with the metal stream [32]. However, the use of these units can cause the freezing of the molten metal at the end of the tundish nozzle, which immediately stops the atomizing. Along with this, the interaction of the gas stream with the nozzle tip can form either underpressure or positive pressure, varying from an underpressure that can significantly increase melt flow rate to an inverse pressure sufficient to stop it and blow gas into the tundish. Thus, great care is needed in setting up closed nozzles and control during atomization.

The WIDEFLOW gas atomizer based on the confined nozzle principle is illustrated in linear modification (Fig. 4.26) [33]. This atomizer involves two chambers, a high-pressure chamber (autoclave) containing melting and pouring units, and a low-pressure atomization chamber divided by a linear Laval gas nozzle. The pressure difference between the two chambers forces the gas-accelerated flow through the converging linear Laval nozzle to sonic velocity, when the pressure ratio exceeds the critical value. The kinetic energy of ultrahigh velocity gas flow is transferred efficiently to the atomization of the thin melt film. Schulz reported that by using nitrogen or argon, the mean particle diameters of about 10 μm can be achieved with pressures of 2.0–2.5 MPa [34].

Prefilming Nozzle Design

In several confined designs, the circulation created by the gas flowing up the side of the tundish nozzle caused due to suction force action, the molten metal to spread across the face of the ceramic nozzle to its edge, where it is sheared by the flowing gas [35]. These nozzle designs are referred to as “prefilming” (Fig. 4.27A) and are quite widely used.

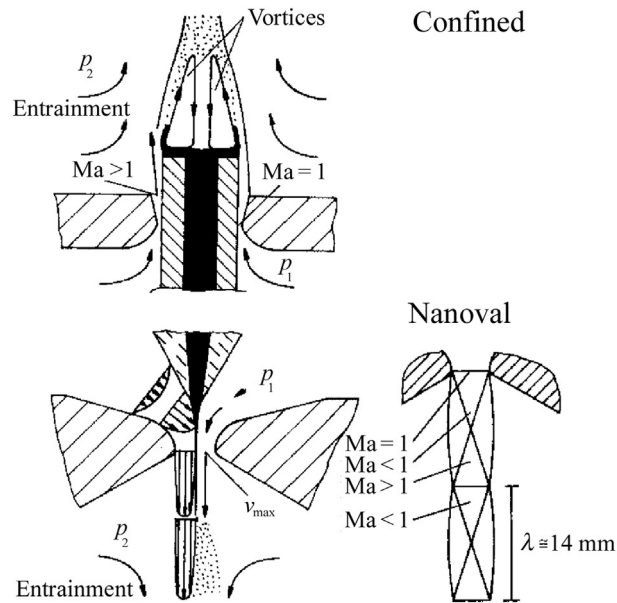


FIG. 4.27 Schematic of prefilming nozzle design (A) and Nanoval design (B). Ma is the Mach number.

The regime when a thin film is formed on the melt nozzle top is the preferred operating regime for producing fine powders. When the metal flow rate is too high, the filming effect is partially lost, and some of the metal is entrained into the low-velocity wake [36]. Such a regime leads to coarser powders and to the formation of undesirable flakes in the powder. The low pressure (suction, aspiration) created at the nozzle tip is a useful feature of the prefilming nozzle design. It is employed to draw the liquid metal into the melt nozzle from the crucible in up-draught operation, as mentioned above. Additionally, the presence of suction at a point of contact between the gas and liquid avoids the potentially hazardous blowback effects observed in free fall nozzle designs for certain jet geometries.

At the same time, by air atomization a sudden stoppage or decrease of flow rate can lead to ignition or explosion of the suspended solid powder in the case of active metals or alloys. The level of suction created by a nozzle is found to be extremely sensitive to nozzle geometry, atomizing gas nature, and operating gas pressure.

Nanoval Nozzle Design

In the Nanoval nozzle design [37], a metal melt stream is broken up by the action of friction forces between the atomization gas and the liquid (Fig. 4.27B). Because the metal stream is always kept very thin and is delivered directly to the throat of the nozzle, this design is capable of producing very fine powders. The comparison of mean particle sizes by Nanoval and the conventional confined nozzle design represented in the form of mass median diameter dependence on specific gas momentum is shown in Fig. 4.28.

Pressure-Swirl Hybrid Prefilming Atomizer

This atomizer combines pressure-swirl atomization and ring-gas atomization. In the first stage, a film is generated followed by gas jet atomization in the second step [38]. The pressure-swirl-metal chamber, atomization chamber, and gas-recirculation system are the main components of the powder atomization unit. Fig. 4.29 [39] schematically shows a pressure-swirl-atomizer. Due to overpressure, the molten metal flows tangentially into the swirl chamber, leaves it through a small cylindrical hole (D_L), and forms a swivelling hollow cone film of molten metal. The film is subsequently atomized by the gas jets through the orifices (D_G).

Spherical tin powders with median diameter 10–20 μm and standard deviation below 2 were obtained by superheating to 373 K, gas (nitrogen) pressure 1.0 MPa, gas-to-metal ratio of 1.3, and with a melt flow rate between 160 and 190 kg/h.

Prefilming Hybrid Atomizer

This atomizer has been developed for viscous melt atomization [40]. Viscous melts, such as oxidized metals or slags, have a comparably high viscosity. The prefilming hybrid atomizer is shown in Fig. 4.30. Their local flow regimes are to be

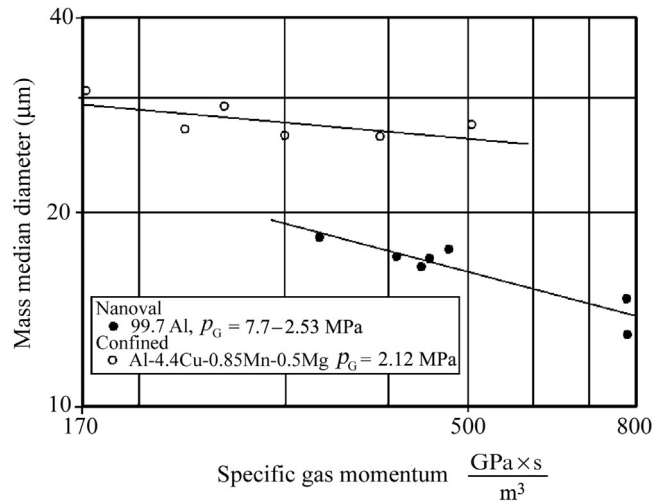


FIG. 4.28 Comparison of mean particle sizes by Nanoval and conventional confined atomizing nozzle designs.

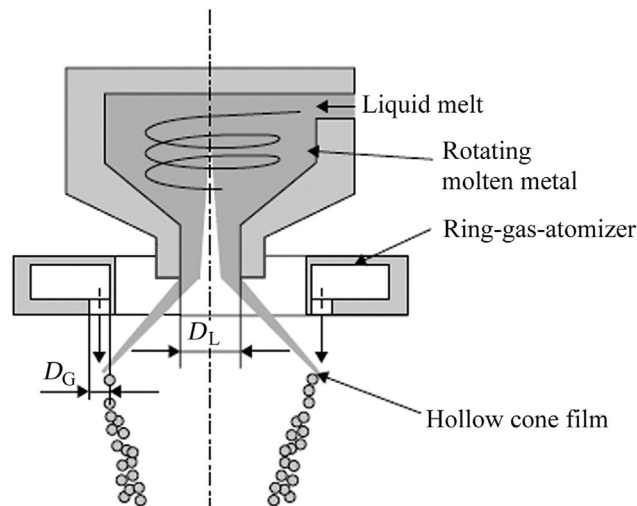


FIG. 4.29 Pressure-swirl hybrid prefilming atomizer.

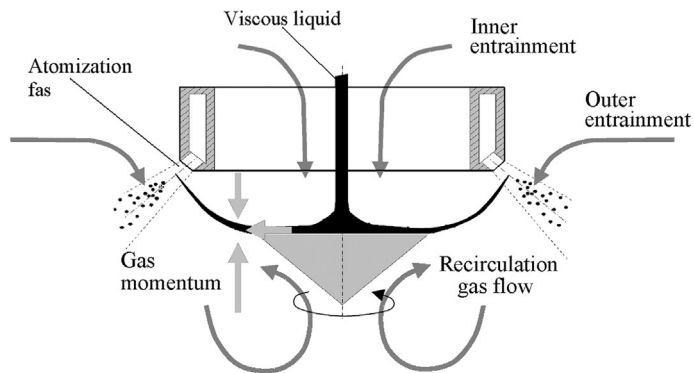


FIG. 4.30 Prefilming hybrid atomizer for viscous melt atomization. Czisch C, Fritsching U. Atomizer design for viscous-melt atomization. *Mater Sci Eng A* 2008;477(1-2): 21-5.

distinguished by the difference from where the ambient gas interacts with the atomization gas. The inner entrainment reaches the atomization area through the atomizer's liquid stream passage. The outer entrainment reaches the atomization area directly and the recirculation gas flow reaches the atomization area from below the rotary disc. The aim of the prefilming hybrid design is to generate a maximum recirculation momentum so that the film is transported closer to the external mixing atomizer gas outlet.

Process Parameters

In conventional gas atomization processes, the atomization pressures are typically in the range 0.5–4 MPa, and gas velocities in the nozzles range from Mach 1 to 3. However, in free-fall atomizers, gas velocities in the impingement zone usually have fallen to 50–150 m/s (for air or nitrogen). Typically, gas-atomized powders are usually spherical with a lognormal size distribution. Average particle sizes are usually in the range 10–300 μm with a standard deviation of about 2; oxygen content is about 100 ppm. Prealloyed alloys are commonly made by inert gas atomization. The worldwide annual tonnage of inert gas-atomized powder is much less than that of water-atomized powders, probably amounting to >50,000 tons per year. Metal feed rates are lower than in water atomization, and the melt batch is smaller. However, the tonnage of air-atomized powders, especially zinc and aluminum as well as copper, tin, lead, and copper alloys, probably exceeds 400,000 tons per year [29]. Air atomizers operate continuously for many hours or around the clock. Multinozzle units are often used to boost the yield on aluminum and zinc.

In conventional inert gas or air atomization, typical metal flow rates through single orifice nozzles range from about 1 to 90 kg/min. The capability of plants varies from very little laboratory units to immense plant such as the ANVAL Atomizer 1 (Fig. 4.31), which is the biggest inert gas atomizer and was designed for producing large tonnages of superalloys and other alloy powders. Melting takes place in two 5.5-ton induction furnaces. Plasma-heated tundish is used. Due to the height of the tower, powder with up to a 1 mm particle size can be produced. Very fine powder can also be produced for applications such as MIM.

In conventional atomizers, the typical gas flow rate ranges from 1 to 50 m^3/min at pressure ranges of 350 kPa to 4 MPa. The superheating of molten metal (the temperature differential between the melting point and the temperature at which the molten metal is atomized) is generally about 75–150 K. In gas atomization with inert gas, the cost of gas consumption is significant, and a means of circulation to promote gas reuse is desirable, especially in large-scale facilities.

In practice, for a given gas nozzle design and size, the mean particle size is controlled by the pressure of the atomizing medium and the melt flow rate. For all nozzles, the velocity of the gas usually “chokes” at sonic velocity (about 300 m/s for nitrogen and argon) in the narrowest region of the nozzle if the upstream gas pressure is at least 1.9 times the external pressure [3].

Therefore, the amount of gas flow (Q) depends on gas pressure, temperature, and nozzle area. For ideal conditions and zero velocity on the entrance side of the nozzle, gas flow can be expressed as:

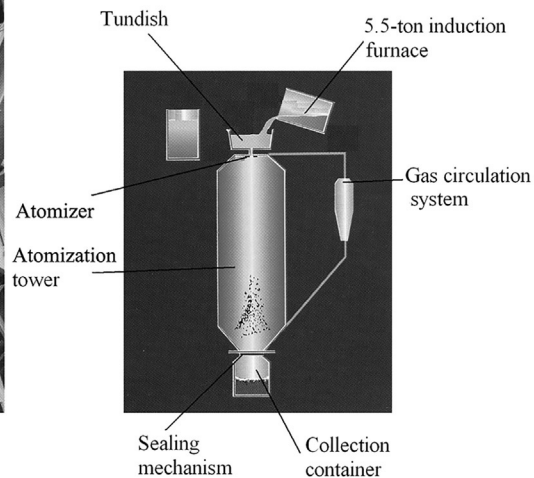
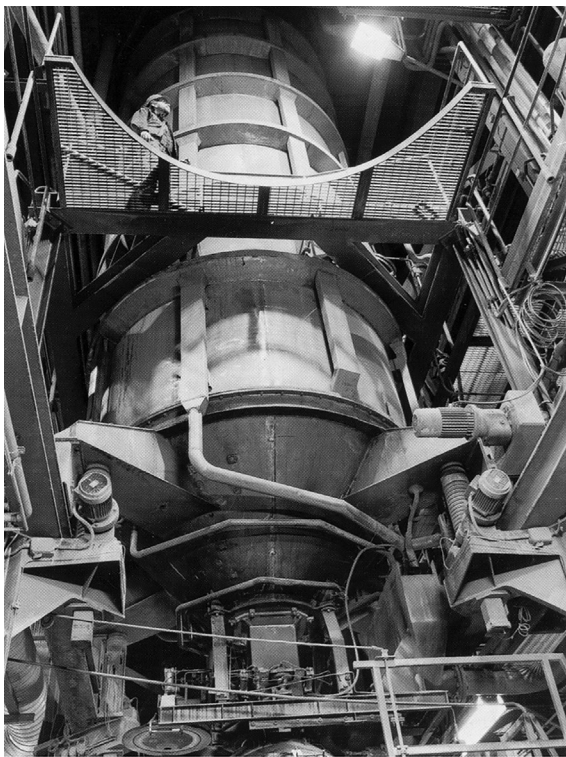


FIG. 4.31 ANVAL atomizer 1. Courtesy of ANVAL.

$$Q = \omega \left(\frac{2}{k+1} \right)^{\frac{k+1}{2(k-1)}} \frac{p\sqrt{2g}}{\sqrt{RT}} \quad (4.11)$$

where ω is the cross section of gas nozzle at exit; k equals C_p/C_v , is the ratio of specific heat at constant pressure and volume, correspondingly; p is the gas pressure in the reservoir; T is the temperature in the gas reservoir; R is the gas constant; and g is the acceleration due to gravity. For nitrogen $k = 1.4$, Eq. (4.11) takes on the form with the dimension of quantity (g/s):

$$Q = 4 \times 10^6 \frac{ap}{\sqrt{T}}$$

Comparisons based on how much powder surface is generated per unit volume of gas spent can be used for evaluation of the gas efficiency. This criterion accounts for higher gas consumption requirements when higher gas pressures are applied in producing finer powders. Confined nozzle designs in comparison with consumption ones give higher efficiencies at a comparable gas-to-metal ratio [41]. A simple equation of median particle size dependence on gas/metal ratios can be used:

$$\delta_m = \frac{k}{\sqrt{G/M}}$$

where k is a constant for the process and G/M is the gas/metal ratio, which is variously measured in kg/kg or cubic meters of gas per metal mass (m^3/kg). The source [32] involves typical values of k for confined nozzle designs.

Models of Gas Atomization

Superheated metal melts may be considered as Newtonian fluids; in this connection, their interaction with a gas jet is expressed by criterial dependences. The most empirical formulations for definition of an average particle size in real atomization systems use the aerodynamic Weber number:

$$We = \frac{\rho_g v_g^2 d_0}{\sigma_m}$$

This criterion represents the balance of the break-up force, related to gas kinetic energy through the gas density, ρ_g , and v_g^2 , that is resisted by melt surface tension, σ_m , acting over a specific melt stream diameter, d_0 .

Generally in each model of droplet formation, a stability criterion involves the Weber number of the liquid metal. The first attempt to develop a model of a three-step droplet formation process seems to have been made by Dombrowski and Johns [42]. Proposed mechanisms of droplet formation involve:

- The initiation of a sinuous wave that rapidly increases in amplitude.
- Detachment of the wave from the layer of the liquid to become a ligament whose dimensions depend on the wave length λ at disintegration on wave number k_w (i.e., $2\pi/k_w$).
- Breakdown of ligaments into droplets (Fig. 4.32).

In Bradley's mathematical model, known as the capillary wave model [43, 44], the liquid is considered to be a horizontal infinitely deep phase, initially unmoving and being swept by a compressible gas phase with a uniform velocity parallel to the liquid surface. The Rayleigh instability was invoked for the break up of the ligament into spherical drops. In the first stage of the atomization process, the critical wave number k_{\max} with the fastest-growing amplitude is determined from the quadratic equation in k and includes a dependence on the kinematic viscosity of the liquid, the densities of the gas and liquid phases, the liquid/gas interfacial energy that opposes the growth of the wave, and the Mach number M of the atomizing gas.

In the second stage of atomization, Bradley suggested that the ligament diameter D is related to the wavelength λ_{\max} , that is, $2\pi/k_{\max}$ by linear dependence:

$$D = \varepsilon \lambda_{\max} = \frac{2\pi\varepsilon}{k_{\max}}$$

where the parameter ε (of the order of 0.25) was defined in earlier studies on the air atomization of water.

The resultant droplet diameter δ is expressed as:

$$\delta = \frac{2.95\sigma_m}{L\rho_g v_g^2}$$

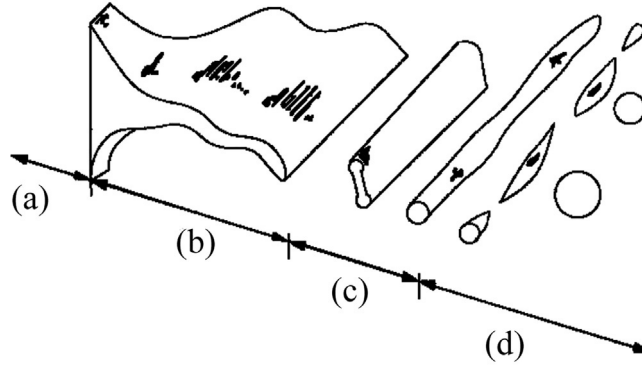


FIG. 4.32 Model for the disintegration of a liquid sheet by a high velocity jet of gas: (a) stable sheet; (b) growth of waves in sheet; (c) ligament formation; (d) ligament breakdown.

where σ_m is the liquid surface tension (N/m), ρ_g is the density of the gas (kg/m^3), v_g is the sonic gas velocity (m/s), L is a dimensionless parameter, the function of the Mach number M and knowing the value of M during gas atomization; and L can be defined by [45].

A comparison of the experimental data of See and Johnston to Bradley's predictions for the nitrogen atomization of lead sees that the model gives agreement approximately within a factor of 2 [46]. As at present design, Bradley's model does not give any indication of the origin of the spread in powder production by gas atomization.

The other often-cited models are the capillary and acceleration wave models of Ingebo [47]. Here, the Reynolds number is an important part of the Ingebo expressions for both capillary and acceleration wave break up. The Reynolds number

$$Re_L = \frac{\rho_L (v_g - v_L)^2 d_0}{\mu_L}$$

contains the dimensionless balance of gas kinetic energy through $(v_g - v_L)^2$, as related to the dynamic viscosity, μ_L , in the melt with a density, ρ_L , in the melt stream diameter, d_0 .

The resulting Ingebo equation is:

$$\frac{d_0}{\delta_m} = c_0 (We Re_L)^m$$

where c_0 and m are adjustable constants; for area $We Re_L > 10^6$ $c_0 = 0.027$ and $m = 0.4$, then

$$\delta_m = 37 d_0 [We Re_L]^{-0.4}$$

A modified capillary wave model in melt atomization was applied in several works [48, 49]. Ternovoy with colleagues [48] considered the atomization of a free melt stream by an annular gas jet with a hollow cone of metal formation. The instability wavelength λ_f with the fastest growing amplitude in the metal film was defined in accordance with [16]

$$\lambda_f = \frac{1.5\gamma}{\rho_g v_g^2}$$

where γ is the specific surface energy of a melt, ρ_g is the gas density, and v_g is the gas velocity at the exit of the melt nozzle.

The droplet formation is considered as a break up of the melt microjets by instability wavelength $\lambda_{\mu j}$ with the fastest-growing amplitude in metal microjets and is described in accordance with [16] by the expression:

$$\lambda_{\mu j} \approx 4\pi \left(\frac{v_m^2 \rho_m \delta_{\mu j}^3}{8\gamma} \right)^{1/4}$$

where v_m is the kinematic viscosity of a melt, ρ_m is the melt density, and $\delta_{\mu j}$ is the diameter of the microjet.

The resulting semiempirical formula for the droplet diameter definition is:

$$\delta_m = \frac{1.88 v_m^{0.4} \rho_m^{0.2} d_m^{1.26}}{\gamma^{0.026} \rho_g^{0.17} R_{tr}^{0.63} v_g^{0.34}} \left(\frac{gh\rho_m + \Delta p}{gh\rho_m - 2\Delta p} \right) \left(\frac{G_m}{G_g} \right)^{0.3}$$

where d_m is the melt jet diameter at the exit of the melt nozzle, R_{tr} is the film opening radius in the position of toroidal thickening on its periphery, g is the acceleration of gravity, h is the melt height in the tundish, Δp is the pressure differential between the furnace chamber and the exit of the melt nozzle, G_m is the melt mass flow, and G_g is the gas mass flow.

More recently, improved flow visualization techniques used to study melt atomization dynamics do not confirm the formation of a film hollow cone in the conditions of atomization of a free melt stream by an annular gas jet [50]. Through that, the authors [49] obtained the tolerable convergence of median particle size values calculated on the suggested formula with measures for argon or argon/helium mixture atomization by a confined jet.

The pressure-swirl atomization principle allows forming the film metal hollow cone, as shown in Fig. 4.29. Here, a conical film of melt created by the pressure swirl nozzle and shaped by centrifugal forces is atomized by high-velocity gas jets. The physical model of such a combined atomization process was represented in the work [51]. These are considered the stages of the atomization process (Fig. 4.33):

1. Transmission of an instability wave in a film across and along the velocity vector owing to oscillation processes caused by external and internal factors. The instability wavelength λ_f with the fastest growing amplitude in a metal film was introduced in accordance with Ref. [16]. Depending on the physical properties of the liquid and gas, two schemes are suggested: a thickening of a film in toroidal form in accordance with the wavelength (Fig. 4.33a) and when a film is just bending (Fig. 4.33b).
2. Formation of a liquid torus on the peripherals of a film as a result of transmission of a longitudinal wave with the fastest growing amplitude.
3. Transmission of the instability of the toroidal peripheral area.
4. All previous stages coincide with the above-described model [49] while the final stage differs because it consists of secondary atomization of previously broken-up film ligaments (torus or drops in dependence on atomization conditions) under the action of a high gas pressure jet.

The thin film represents a surface for efficient disintegration in order to achieve fine particle sizes and narrow size distribution using low specific gas consumption.

On the basis of this model, a formula for the definition of particle diameter was suggested:

$$\delta = k\varphi^{0.46} \frac{v_m^{0.17} \rho_m^{0.08} \sigma^{0.38} d^{0.92}}{R_f^{0.46} \rho_g^{0.46} v_g^{0.92}} \quad (4.12)$$

where k is the coefficient of the nozzle geometry; φ is the unfilled coefficient for the melt nozzle orifice of d diameter; v_m is the kinematic viscosity of a melt; ρ_m is the density of a melt; σ is the surface tension of the melt; R_f is the radius of the film at the point of break up; and ρ_g and v_g are the density and velocity of a gas stimulating the film atomization.

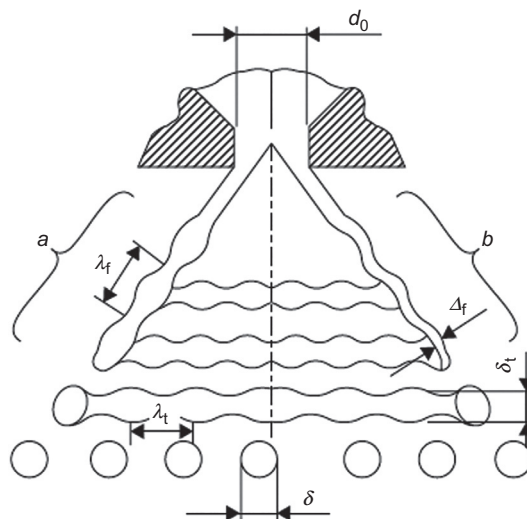


FIG. 4.33 Model of the pressure-swirl atomization process: d_0 is the melt metal nozzle orifice diameter, Δ_f is the film thickness in zone of impingement with secondary atomization gas jet, δ_t is the diameter of max torus cross section in zone of impingement with secondary atomization gas jet, λ_f is the wavelength of film instability, λ_t is the wavelength of in liquid torus, and δ is the atomized particle diameter. *Lagutkin S, Uhlenwinkel V, Achelis L, Pulbere S, Sheikhaliev S. Centrifugal—gas atomization: preliminary investigation of the method. In: Proceedings PM 2004 World Congress. Wien, Austria: EPMA; 2004. p. 71–6.*

TABLE 4.3 Tin Powder Properties Produced by Means of the Pressure-Swirl Atomization Process.

Oxygen Content in the Atomization Chamber (ppm)	Melt Temperature (K)	Melt Pressure (MPa)	Melt Flow Rate (kg/h)	Gas Pressure (MPa)	Gas Flow Rate (m ³ /kg)	Mass Median Diameter (μm)	Standard Deviation (δ_{84}/δ_{50})
<100	563	0.7	180	0.7	109	33.5	1.85
100	563	0.7	180	0.7	109	22.8	1.6
300	563	0.7	180	0.7	109	22.1	1.6
500	563	0.7	180	0.7	109	24.6	1.6

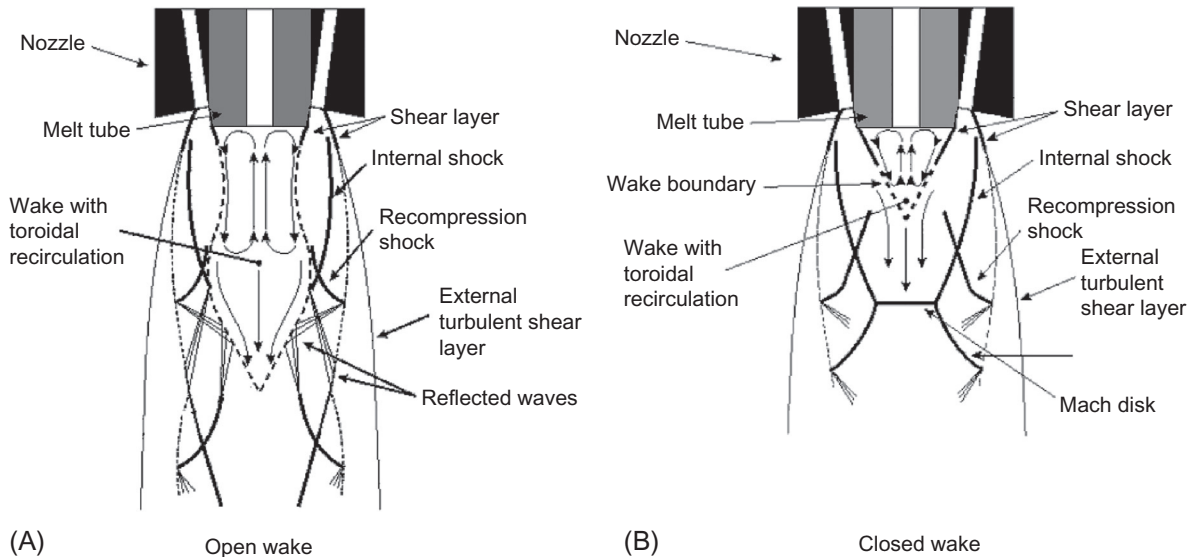


FIG. 4.34 Schematic of (A), open-wake and, (B) closed-wake gas flow patterns in close-coupled gas atomization. Anderson IE, Terpsta RI, Figliola R. Gas recirculation flow in the melt feeding zone of a close-coupled gas atomization nozzle: modelling and measurement. In: Proceedings of 2nd international conference on spray deposition and melt atomization, vol. 2. Bremen: Bremen Universität; 2003. p. 19–30.

The estimation of the mass median diameter, offered by Eq. (4.12), shows sufficient comparability between the calculated and experimental values for tin, tin-lead solder (61Sn-39Pb), and copper alloy (Cu-15Sn-5Pb-4Ni) in experiments by gas/metal ratio values in the range from 0.15 to 0.35 m³/kg [51]. An effect of oxygen content on powder properties was revealed (Table 4.3).

Traditionally, gas atomization by means of close-coupled nozzles is believed to involve the formation of a melt film at the nozzle edge [35], as shown in Fig. 4.27A. Fine particles are thought to form as a result of the primary breakup of the melt film upon its interaction with the supersonic gas flow at the nozzle edge. Further, even if low melt flow conditions that favor filming are used, it has been suggested that secondary breakup still plays an important role in determining particle size.

More recently, a microsecond-exposure spark schlieren technique allow us to visualize the melt atomization process along with the atomizing gas flow features, providing a look at the fluid dynamic interactions during atomization [50]. These experiments indicated more complex atomization behavior, including a primary breakup stage close to the nozzle tip followed by a finer secondary breakup stage where the coarse droplets are disintegrated under high shear into fine powder. Therefore, several authors [52, 53] have discussed the apparent dominance of secondary atomization and break-up mechanisms in most studies of close-coupled gas atomization.

The increased understanding of the atomization process shows new ways to approach the problem of particle size control and atomization efficiency. In this connection, in close-coupled gas atomization there is considered a description of the two gas flow situations that are termed the open wake condition [53, 54], as shown in Fig. 4.34A, and the closed wake

condition in Fig. 4.34B. Where the sketches are of a central cross-section and may apply to either a discrete jet nozzle ensemble or an annular slit nozzle with the same melt tube arrangement.

A more complicated gas flow situation has often been developed purposefully for the production of high yields of fine droplets where the shear wall gas flow is interrupted by a Mach shock disc. The Mach shock disc can appear during high-pressure operation of either an annular slit [54] or a discrete jet [55]. The wake closure effect and its associated Mach shock can present an additional kind of atomization energy coupling.

The pressure value on the liquid metal nozzle tip is an important parameter in close-coupled gas atomization. The pressure formation on the melt nozzle tip in dependence on gas pressure is shown in Fig. 4.35.

A pulsatile gas-atomization model based on the close-coupled atomization kinetics advances the understanding of the atomization process fundamentals [56–59]. The model reveals that melt flow rate is determined by the time-averaged stagnation pressure formed in front of the melt orifice. This stagnation front dictates the behavior of the melt exiting the melt orifice and how it interacts with the atomizing gas.

As illustrated in Figs. 4.34 and 4.35, the rapidly flowing gas passing around the melt tip can produce an overambient or subambient pressure region in front of the delivery tube orifice that is often known as the aspiration base pressure. Ting [59] reported that seven 22.7 kg batches of an Ni-based alloy were atomized. Prior to atomizing each batch, the gas-only aspiration profile of the atomizer nozzle was measured with a digital pressure transducer to determine the manifold pressure at which wake closure occurred. The aspiration measurements discovered the existence of an abrupt transition zone between open-wake and wake-closure conditions (Fig. 4.36). The tests indicated that this transition pressure, named the wake-closure pressure (hereafter known as WCP), developed around 4.93–4.95 MPa (715–718 psi).

For each atomization batch of the Ni-based alloys, the atomization gas pressure in the nozzle manifold was selectively tuned to atomize at pressures either above or below the WCP. Batches that were atomized below WCP had shallow gas-only aspiration of 0.25 atm. (3.7 psi) below atmosphere pressure while batches atomized above WCP had deep gas-only aspiration of 0.58 atm. (8.5 psi) below atmosphere. The atomization pressure was monitored, and the particle size distribution was vibratory screened and sonically sieved to obtain the particle size distribution above and below 45 μm , respectively.

The gas-to-melt ratio, atomizing pressure, median diameter δ_{50} , and standard deviations (δ_{84}/δ_{50}) are presented in Table 4.4. Produced powders in a close-wake regime showed considerably finer median δ_{50} particle size than those atomized at pressures below WCP (in open-wake condition). The median particle size from L1271 atomized at 0.017 MPa (3 psi) above WCP was 42% (or 26.5 μm) smaller than that of L1270 atomized at 0.034 MPa (5 psi) below WCP. The 60% longer gas atomization run time, associated with a slower average melt flow rate, resulted in the particle refinement in L1270. This atomization run had a 64% greater gas-to-metal ratio (GMR) than L1271 (Table 4.4). It was also interesting to note that atomizing at pressures above WCP showed a resulting mean average 23% improvement in particle size standard deviation (δ_{84}/δ_{50}) when compared to atomization below WCP, giving rise to a narrower particle size distribution. The observed particle yields above and below WCP in melt atomization are due to changes in the atomization gas dynamics when the melt is introduced.

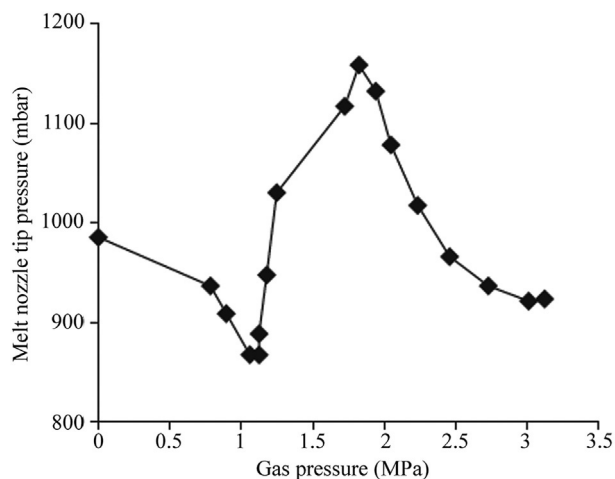


FIG. 4.35 The pressure formation on the melt nozzle tip in dependence on gas pressure in close-coupled slotted nozzle design (by the constant protrusion length 10 mm).

FIG. 4.36 Gas-only aspiration pressure measurements at the melt orifice. Shaded area shows the WCP location. *Reproduced with modification from Ting J. The close-coupled gas atomization: a quantitative analysis of the dynamic pressures of the pulsative atomization process. In: Compiled by Russell A, Chernenkoff W, Brian J. Proceedings of 2014 powder metallurgy world congress. Orlando, FL: Metal Powder Industries Federation; 2014: p. 02-76–84.*

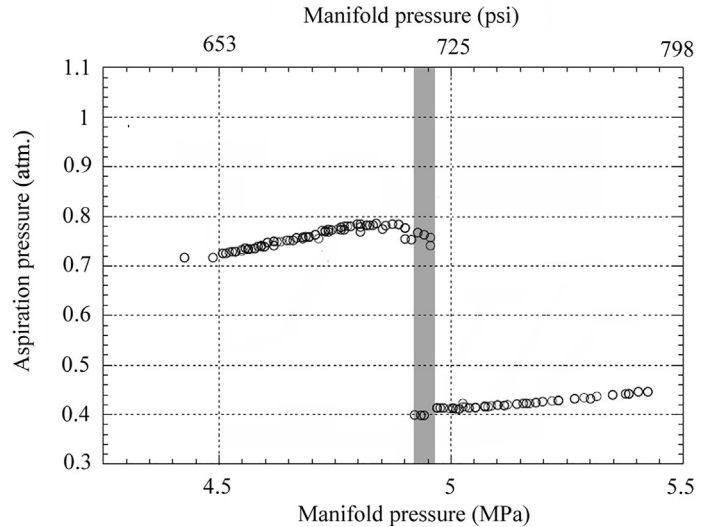


TABLE 4.4 Atomization Parameters and Results for a Nickel-Based Alloy Produced Near the WCP

Batch Number	GMR	Atomizing Pressure (MPa)	δ_{50} (μm)	δ_{84}/δ_{50}
L 1267	1.77	4.48	68	3.16
L 1271	2.48	4.89	63.5	3.38
L 1270	4.06	4.96	37	2.61

The aspiration pressure being the force of the total recirculating gas flow on the melt discharge orifice area, the proposed model [57, 60] suggests that it is possible to determine a stagnation pressure in the wake front of the atomizer nozzle, hence providing a way to regulate the atomization process. According to this model, the majority of the gas masses enter the wake through the stagnation front and exit along the circumferential edge of the melt tip base. In Fig. 4.37A below WCP (in open-wake condition), the recirculating gas enters the wake via Point 1 (stagnation front) and exits the edge of the melt tip, as depicted. The turbulent boundary that separates the recirculation zone (inside) from the atomization gas stream (outside) has been identified as the “sonic line” [57]. In the two-phase flow interaction between the melt and the gas, the gas-only feature at below WCP creates the aspiration pressure that draws the melt into the wake, causing it to enlarge and allowing the stagnation pressure at Point 1 to quickly and easily be drawn to the melt orifice. The reverse gas flow against the melt orifice then temporarily arrests the melt flow (Fig. 4.37B). As the recirculation is devoid of melt, the aspiration pressure is formed once again to draw the melt down the tundish nozzle.

In the computational fluid dynamic study by Ting and Anderson [58], using the modeling, they showed that the stagnation pressure (Point 1) at the primary wake front was twice its magnitude before WCP (Fig. 4.37A) when compared to after WCP (Point 2) (Fig. 4.37C). Subsequently, the smaller new primary recirculation zone (above WCP) with the smaller stagnation pressure Point 2 generates a lower orifice pressure than that at Point 1 (below WCP). From the modeling [57, 59], two stagnation pressure points are formed downstream of the Mach disc (depicted as Points 3 and 4 in Fig. 4.37C). Above WCP, the magnitude of the stagnation pressure at Point 4 is 1.28 times greater than that at Point 1 below WCP. This is important because it is this stagnation pressure Point 4 that is the primary pressure that causes the melt to slow in above-WCP atomization, and making melt flow slower than in open-wake atomization.

In the two-fluid flow closed-wake condition, the melt flowing from the delivery tube orifice acts as a moving boundary that can disrupt the stability of the closed-wake structure by displacing the internal shock (Fig. 4.37C). In this state, the Mach disc vanishes (Fig. 4.37C) and the stagnation pressure from the secondary recirculation zone rushes into the “opened” primary recirculation zone, pushing upward against the melt orifice and temporarily arresting the melt flow. As the melt flow is indented in the pour tube and short halted by the strong upstream gas flow from stagnation Point 4 (Fig. 4.37E), the gas dynamic is the reestablishment of the Mach shock structures as the recirculation is devoid of melt. The deep aspiration

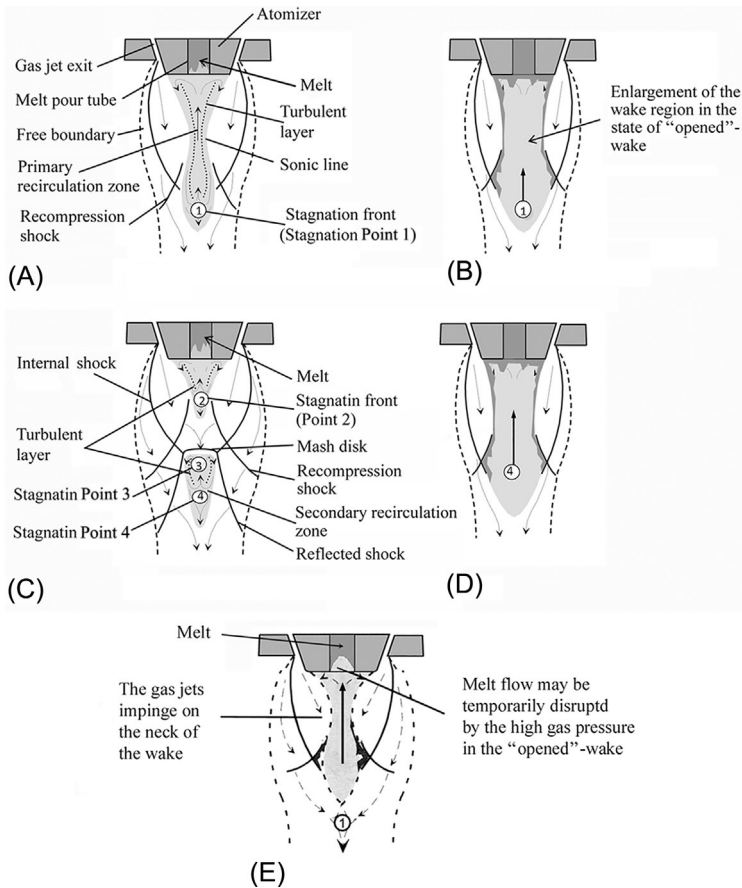


FIG. 4.37 The phase flow interaction by the pulsatile atomization model below (A, B) and above (C, D, E) WCP. Reproduced with modification from Ting J, Peretti MW, Eisen WB. *The effect of wake-closure phenomenon on gas atomization performance.* *Mat Sci Eng* 2002;A326:110–21; Ting J. *The close-coupled gas atomization: a quantitative analysis of the dynamic pressures of the pulsative atomization process.* In: Compiled by Russell A, Chernenkoff W, Brian J. *Proceedings of 2014 powder metallurgy world congress.* Orlando, FL: Metal Powder Industries Federation; 2014: p. 02-76–84.

pressure of the reestablished closed-wake condition strongly draws the melt down the ceramic pour tube to once again resume the melt flow (Fig. 4.37D). When operating at above WCP, this whole intermittent melt atomization process would repeat itself, pulsating between Fig. 4.37C and Fig. 4.37E. Thus, own domination the pulsatile atomization model had derived thanks to such atomization cyclicality.

It is necessary to note that the wake-closure phenomenon is highly sensitive to atomizer and melt pour tube geometry. It possesses a hysteresis-type aspiration behavior that suggests that there is an energy of formation associated with the wake-closure structure.

Rieken et al. [61] developed the enhanced closed-wake nozzle (named ECW) containing an interior ring of 30 jets with 0.74 mm diameter and a gas flow apex angle of 45 degrees equally spaced around 11.15 mm annulus, similar to the DJ-HPGA nozzle type [62]. It also contains an additional second concentric ring of 60 jets with 0.74 mm diameter and gas flow apex angle of 90 degrees equally spaced around a 21.92 mm annulus (Fig. 4.38). The ECW geometry was selected to create an identical gas flow focal point between the two rings of jets while the exterior ring of jets contains twice the cross-sectional area compared to the interior jets. The two rings of jets in the ECW nozzle are hermetically isolated (during operation) and supplied from independent gas manifolds, allowing significant experimental design flexibility (e.g., independent manifold pressures and/or differing atomization gas types).

According to the work [61], three gas nozzle configurations were engineered and tested using a high temperature alloy to develop atomizer parameters to maximize powder yield in the 20–75 μm range. The comparison between close-coupled atomizers with close-wake and enhanced closed-wake nozzles showed the 20–70 μm fraction yield up to 68% and 74%, respectively.

Lampa and Fritsching [63] discussed the effect of spray parameters on the large-scale fluctuations of gas and droplets in confined sprays investigated experimentally and numerically. In numerical simulations, the relevant fluctuating scales have been resolved with large-eddy-simulation (LES) [64]. In the experimental part adopted from the work [65], twin-fluid nozzles in a confined environment have been analyzed with planar Particle-Image-Velocimetry (PIV) to yield the velocity of the gas and the discrete phase. The transient behavior of the spray process including the spray flow structures in

FIG. 4.38 Schematic representation of the two close-coupled atomizer gas nozzles: (A) closed-wake and (B) enhanced closed-wake (ECW).

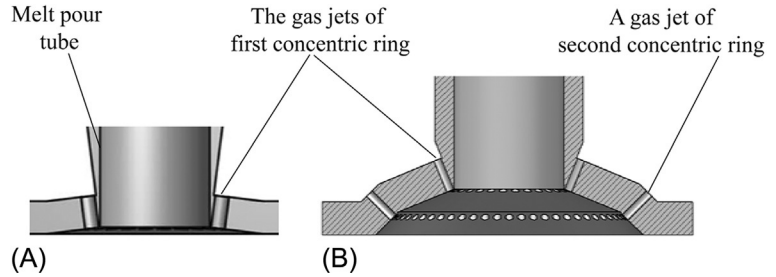
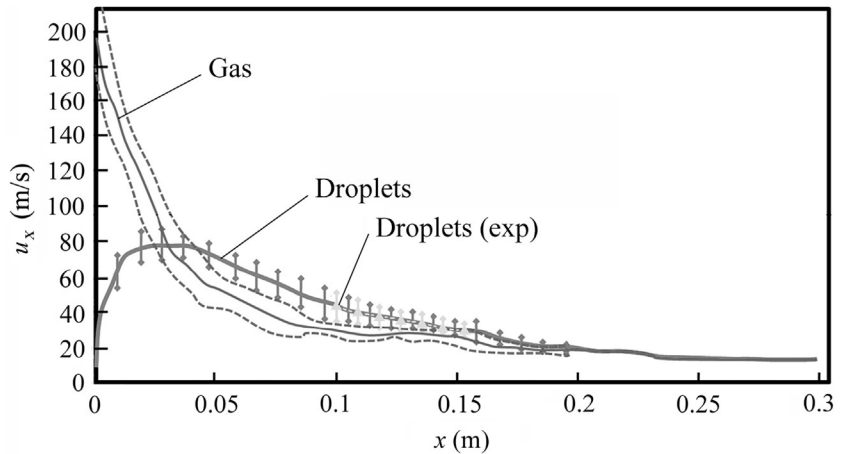


FIG. 4.39 Axial gas and droplet velocity on spray axis (LES) and validation with experimental droplet velocity (PIV, $p=0.5$ MPa). The error bars and dashed lines indicate the upper and lower RMS values of the velocity component. Reproduced with modification from Lampa A, Fritsching U. Spray structure and propagation in confined atomization processes. In: Uhlenwinkel V, Fritsching U, Ellendt, Mädler, editors. Proceedings of 5th international conference on spray of spray deposition and melt atomization. Bremen, Germany: Universität Bremen; 2013. p. 1–14.



dependency from the spray chamber design was discovered by LESs. For the validation of the LES spray simulation, the numerical results have been compared with PIV measurements in the distance range 100–157 mm in the stream-wise direction. The distribution of axial gas and droplet velocity on the spray axis (LES) and experimental droplet velocity (PIV) presented in Fig. 4.39 shows in principle good agreement with the measured data, through the authors reported [63] that generally the mean absolute droplet velocity is higher than the mean absolute gas velocity in this region of the spray.

Studies based on water-spray modeling of the close-coupled atomization [66] showed that a combination of gas pressure, nozzle insert angles, and extension can lead to melt film back flow, a so called “lick back.” Fig. 4.40 is a schematic of the cross-section of an annulus-type nozzle showing the normal path for the melt and the melt path taken that defines full lick back situations. As mentioned above, lick back can appear as a result of atomizer design features. Other factors may also lead to lick back, such as gas pressure regime, surface tension of the melt, and the melt reaction with the insert’s surface. If the melt makes contact with the inner annulus, the nozzle will be destroyed.

Strauss [66] reported the study of nozzles with a three-nozzle tip angle (Fig. 4.41) and at two atomization pressure levels (arbitrarily low and high). Additional tests were performed with the insert recessed and protruding from its normal placement in the atomization nozzle.

Fig. 4.42 shows three typical atomization conditions: (a) partial, (b) total, and (c) and without lick back. In the case of the matched angle configuration, the low-pressure level shows total lick back. The high-pressure level shows partial lick back. In this case, increasing the pressure decreases the extent of lick back. When the nozzle jet angle is less than the nozzle insert angle, total lick back is at both pressure levels. In the case where the nozzle jet angle is greater than that of the insert, lick back does not occur at the low-pressure level and only partial lick back occurs at the high-pressure level. Among the compared nozzle insert placements, the atomization nozzle with a greater angle in a protruding placement appeared more preferable.

Outside the design of the attributes of the atomization nozzle and nozzle insert, there are other factors that may lead to or cause lick back. Along with the gas pressure, the surface tension effect may be related to another extrinsic factor connected to the lick back occurrence. Strauss also reported [66] the tests using water, acetone, and isopropyl alcohol as the atomized fluid by pressure ramped slowly to determine the onset pressure of lick back. These tests showed that the onset of lick back occurred 0.1 MPa (~ 15 psi) lower in pressure for acetone and isopropyl alcohol than for water. The surface tensions of these fluids are 5–20 times lower than those of molten metals. On the basis of surface tension dependence data from varied

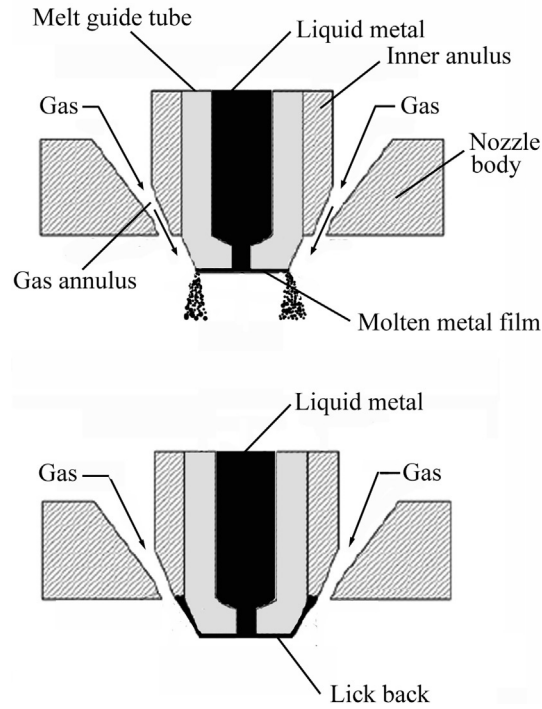


FIG. 4.40 Molten metal film formation for normal and lick back modes.

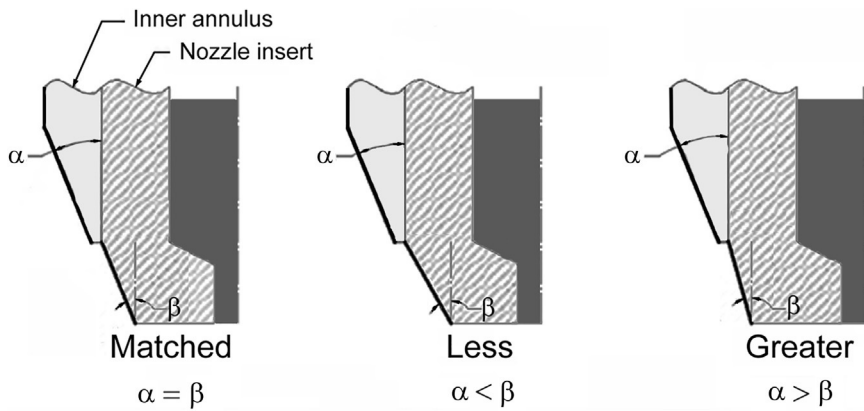


FIG. 4.41 Schematic of the angle matching between the nozzle jet and nozzle insert.

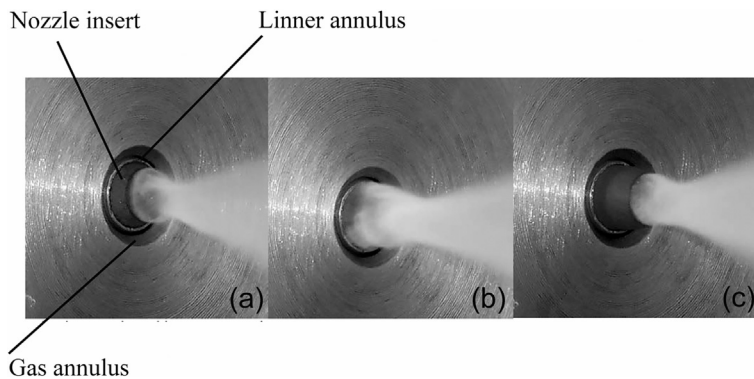


FIG. 4.42 Configuration of atomization plume: (A) the angles of the nozzle jet and nozzle insert are matched, at high pressure; (B) the angle of the nozzle jet is less than the insert angle, at high gas pressure; (C) the angle of the nozzle jet is greater than the insert angle, the nozzle is in a protruding placement, at low gas pressure. *Reproduced with modification from Strauss JT. Lick back in close-coupled atomization: a phenomenological study. In: Compiled by Russell A. Chernenkoff W, Brian J. Proceedings of 2014 Powder Metallurgy World Congress, Orlando, FL: Metal Powder Industries Federation; 2014: p. 02-38-45.*

factors, the author concluded that, while surface tension may not be the primary driving force for lick back, it is certainly plausible that it can affect the occurrence of lick back. Slight changes in alloys, insert materials, impurities, and oxygen content may possibly be enough to cause lick back that is otherwise simply explained by random occurrences.

In the paper [67], Mullis and Dunkley discussed using acoustic techniques [68, 69] for study of the pulsation phenomena during close-coupled gas atomization of a metal melt. The gas atomizer studied uses a gas delivery nozzle of the annular slit type with the melt delivery nozzle having an included apex angle of 30 degrees, a tip diameter of 9 mm, and a central bore for the melt feed of 5 mm. The atomizer was operating with nitrogen gas at a gas inlet pressure of 2.4 MPa. The melt and gas flow rates were 0.25 and 0.35 kg/s, respectively, and a typical batch atomization takes about 15 min, wherein some 200 kg of metal was atomized. During the run recorded, the gas was preheated to an inlet temperature of 673 K, wherein the jet exit temperature upon ideal expansion will be 190 K. made an audio recording during gas atomization.

The authors found that there is strong absorption of frequencies in the 1–8 kHz range. These frequencies are characteristic of the resonance of droplets with 150–600 μm diameters and may be indicative of the dynamics of the initial breakup of melt ligaments. During atomization, it was found that there are considerable low frequency (<30 Hz) fluctuations in the intensity of the acoustic emissions. In the judgment of the authors, this may be related to atomizer pulsation and the quasi-periodic low-frequency variation in the melt volume instantaneously at the atomizer tip (see Fig. 4.37).

According to Ref. [67], in contrast with high speed imaging, acoustic recording is inexpensive and can be set up at a distance of about 1 m from the atomizer without the need for direct line-of-sight of the melt plume. Moreover, the equipment is much more robust than precision optics, needs no careful alignment, and produces a data stream of a size that would make real-time processing feasible.

Gas-Atomized Powders

Particle Size, Size Distribution, Shape, and Surface Morphology

There is a comprehensive literature base on gas atomization in terms of the effect of operating conditions on powder properties [6, 15, 70, 71].

One of the most important single parameters controlling particle size in gas atomization is specific gas consumption. It can be expressed as a mass ratio of gas-to-metal flow or as the ratio of gas volume to metal mass. Data for several metals and alloys conform to an equation of the form:

$$\delta_m = KF^{-1/2}$$

where K is a constant and F is the specific gas consumption in m^3/kg . The value of K is a function of nozzle design and alloy properties [15].

Specific gas consumption is also an important process parameter in controlling δ_m in ultrasonic gas atomization [46, 72]. For an aluminum alloy at a fixed atomizing gas pressure, median diameter value can be varied from ~ 250 to below $50 \mu\text{m}$ when the mass flow ratio of gas to metal increases from 0.3 to 2.0. A decrease in δ_m is also predicted with increasing gas pressure.

Gas-atomized powders generally have a lognormal size distribution with standard deviation normally around $\sigma = 2.0 \pm 0.3$. The values of σ generally decrease as δ_m decreases and most data show an empirical relation of the form [70, 73]:

$$\sigma = a\delta_m^b$$

where a and b are constants.

Lubanska [73], by comparing the literature on gas-atomized metal powders and by using a relationship developed by Wigg [74], derived an empirical equation for the average particle size (δ_m). In dimensionless form, Lubanska's formula is:

$$\frac{\delta_m}{d_0} = K \left[\frac{v_m}{v_g} \frac{1}{We} \left(1 + \frac{M}{A} \right) \right]^{1/2} \quad (4.13)$$

where We is the Weber number; δ_m is the mass median particle diameter; d_0 is the diameter of the metal stream; v_m is the kinematic viscosity of liquid metal; v_g is the kinematic viscosity of the atomizing medium; M/A is the ratio of gas-to-metal mass flow rates; and K is a constant.

Data from the source [73] for various metals are depicted graphically on a log/log scale in Fig. 4.43 and show consistent agreement with experimental data.

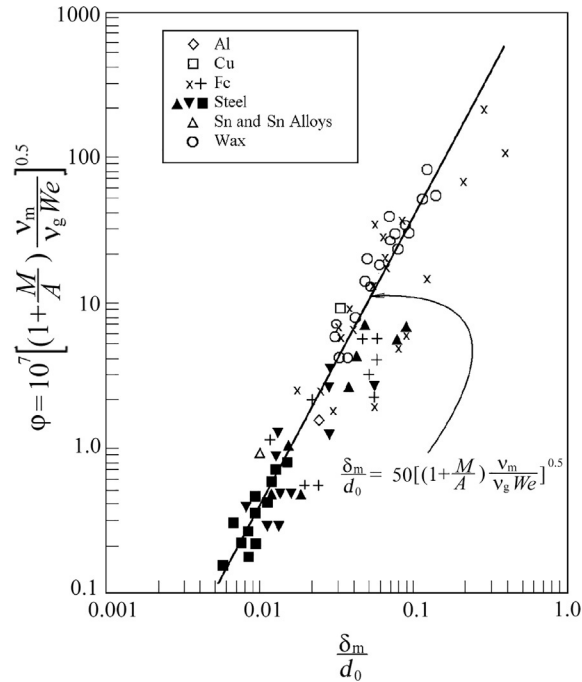


FIG. 4.43 Lubanska correlation (Eq. 4.13) for air atomization.

Various other empirical equations have been published. Miller and Giles [13] have analyzed the atomization of a variety of metals and concluded that acceleration wave break up predominates at a high gas velocity. They define a modified Weber number and correlate it to material properties and the ratio of gas-to-metal mass flow rates. The functional (dimensionless) form of relation was obtained from experiments.

Some empirical relationships can be transformed in terms of physical models for droplet formation. That referred to as maximum stability criterion, for instance, gives maximum drop size as a function of surface tension of the liquid metal (σ), gas density (ρ_g), and velocity (v) of the atomizing medium as:

$$\delta_{\text{crit}} = \frac{\sigma}{\rho_g v^2}$$

This equation applies to the breakup of ligaments [46]. Secondary disintegration into particles smaller than δ_{crit} occurs only if the dynamic pressure due to the gas stream velocity exceeds the restarting force of surface tension. Owing primarily to the higher surface tension of liquid metals, energy requirements and, therefore, gas pressures used for atomizing metals is typically between 0.35 and 2.75 MPa.

Similar to water atomization, commercial gas-atomization units exhibit nonuniform operating characteristics. Proprietary empirical relations have been established between operating conditions, material properties, and powder characteristics, in particular median particle size and standard deviation. Beddov [75] has annotated several of these empirical relations for gas atomization.

The majority of inert gas-atomized powders are spherical or nearly spherical in shape. However, in reality, “satelliting” may be formed when small particles are attached to larger particles (Fig. 4.44). Their collision probability is increased with small particle yield growth and/or by the circulation of gas within the atomizing chamber that lifts finer particles back into the spray plume, where they collide with larger, still partly molten particles [76].

In the absence of impurity effects and surface oxide films, particle shape is controlled by the relative magnitudes of the times for solidification and spheroidization, provided the residence time of the particle in the suspended solid state in the gas is greater than either of these times. Models of both phenomena are given in Ref. [77].

In the model for solidification time in gas atomization, it was assumed that the molten droplets did not undercool, that the relative velocity between the gas phase and the particle is constant, and that convective heat transfer is dominant. Then, the total solidification time τ_{sol} (in seconds) [46, 77] is expressed by:

$$\tau_{\text{sol}} = \frac{\delta_m \rho_m}{6h_g} \left[(c_p)_m \ln \left(\frac{t_{\text{in}} - t_g}{t_m - t_g} \right) + \left(\frac{\Delta H_m}{t_m - t_g} \right) \right]$$

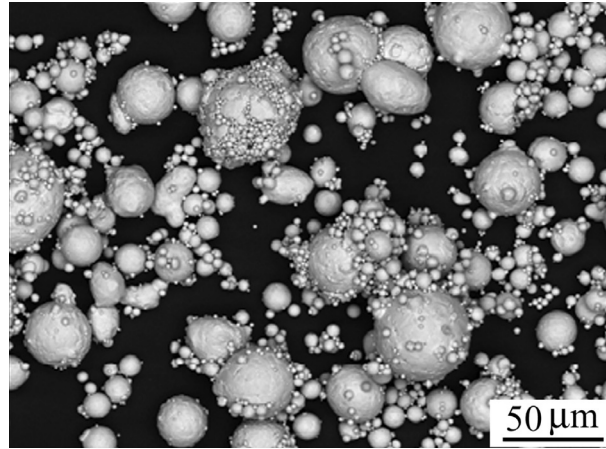


FIG. 4.44 Argon gas atomized Cu-10Sn alloy.

where δ_m is the mass median particle diameter (m); h_g is the convective heat transfer coefficient of the gas ($W/(m^2 \cdot K)$); ρ_m is the density of the liquid metal (kg/m^3); $(c_p)_m$ is the heat capacity of the liquid metal ($J/(kg \cdot K)$); t_{in} is the initial temperature of the particle (K); t_g is the gas temperature (K); t_m is the melting point of the metal/liquidus temperature for alloys (K); and ΔH_m is the latent heat of fusion of the metal (J/kg).

The value of h_g is given by:

$$h_g = \frac{k_g}{\delta_m} (2.0 + 0.6Re^{0.5}Pr^{0.33})$$

where k_g is the thermal conductivity of the gas ($W/(m \cdot K)$); Re is the Reynolds number relative to the particle; and Pr is the Prandtl number for the gas.

Under the influence of surface tension forces alone, the time for spheroidization τ_{sph} is expressed by:

$$\tau_{sph} = \frac{3\pi^2\mu_m}{4V\sigma_m} (r^4 - r_{tr}^4) \quad (4.14)$$

where μ_m is the dynamic viscosity of the liquid metal ($Pa \cdot s$); V is the particle volume (m^3); σ_m is the surface tension of the liquid metal (N/m); r is the radius of the spheroidized droplet (m); and r_{tr} is the metal liquid trickle radius before transformation to spherical droplets (m).

A more detailed and general model to estimate the time for spheroidization of a droplet has been given by Rao and Tallmadge [78]. Lawley [13] notes that their predicted spheroidization times are not significantly different from those given by Eq. (4.14).

Based on these models, See and Johnston [46] have calculated the times for spheroidization and solidification of a range of droplet sizes (149–420 μm) for tin. Spheroidization times ($< 2 \times 10^{-5}$ s) are several orders of magnitude lower than the times required for solidification so that only spherical particles should be produced in gas atomization, if there are no factors that hinder this transformation. The presence of ligament-shaped particles of Sn, particularly at small particle size fractions, is attributed to the presence of an oxide layer (SnO_2) that opposes the action of the surface tension.

The surface of gas-atomized powders is generally smooth. The particle surfaces frequently exhibit a cellular or dendritic morphology, subject to cooling rate during solidification of the droplets. When reactive elements are prealloyed with the base elements, some surface oxidation can occur during gas atomization.

The spherical shape and smooth surface inhibit the development of green strength in cold compaction. In addition, prealloying before atomization increases particle hardness and strength, which reduces compressibility. These inherent limitations of gas-atomized powders have stimulated development of elevated temperature consolidation processes to achieve high density; examples include hot extrusion and hot pressing. A change in particle shape toward nonsphericity is possible by means of an increase of cooling rate via decreased particle size. There is also the possibility of adding elements that alter the surface tension values (Li, Mg, Si, Ca, Mn, etc.).

The relatively high cooling rates intrinsic to gas atomization result in fine-scale microstructures. In NiAl and Ni₃Al powders, sonic gas atomized using nitrogen either dendritic or equiaxed structures depending on the particle size and consequently on the cooling rate were disclosed [79]. The Al₈₂Ni₁₀Y₈ alloy powder produced at a close-coupled nozzle

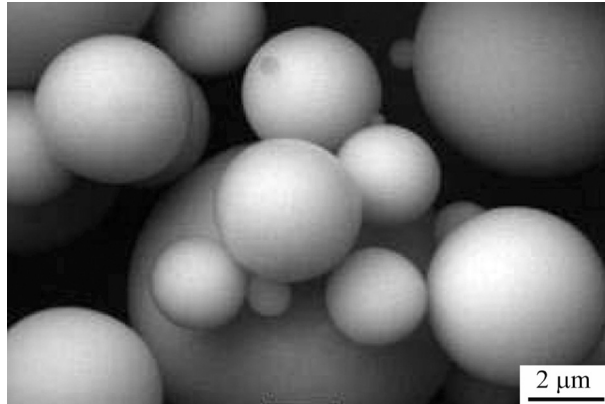


FIG. 4.45 Surface morphology of Al₈₂Ni₁₀Y₈ alloy powder with particle diameter below 15 μm. Liu Y, Guo Sh, Huang B, Liu Z, Du Y. *Densification behaviour of Al-Ni-Y powder containing amorphous and nanocrystalline phases*. In: *Proceedings PM2004 world congress, vol. 1*. Wien, Austria: European Powder Metallurgy Association; 2004. p. 425–30.

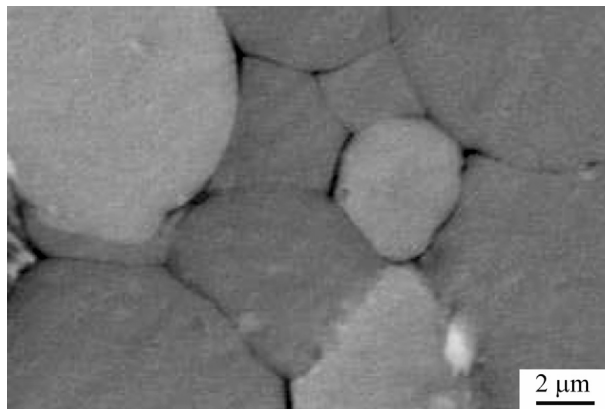


FIG. 4.46 SEM microstructure of Al₈₂Ni₁₀Y₈ alloy powder with particle diameter below 15 μm. Liu Y, Guo Sh, Huang B, Liu Z, Du Y. *Densification behaviour of Al-Ni-Y powder containing amorphous and nanocrystalline phases*. In: *Proceedings PM2004 world congress, vol. 1*. Wien, Austria: European Powder Metallurgy Association; 2004. p. 425–30.

atomizer unit at 3.03 MPa argon jet pressure has perfectly spherical and smooth particles (Fig. 4.45). In particles of several micrometers, the dendritic and cellular microstructures were not detected and they tend to be amorphous (Fig. 4.46).

Internal pores can be present in gas-atomized powder and may be detrimental in several respects. The effect of closed porosity leads to reduced apparent density, causes gas bubbling in thermal spray deposits, and gives rise to uncontrolled dimensional change during sintering. Internal pores are of the most concern in superalloy powders atomized with argon. The argon in the pores is insoluble in the alloy and this gives rise to the phenomenon of thermally induced porosity following densification by hot isostatic pressing with an attendant decrease in mechanical properties. From the study [80], it is concluded that internal closed porosity is a common phenomenon in gas atomization and that its extent increases with increasing particle size. A major source of internal porosity is gas entrapment, especially when the gas is insoluble in the solid powder particles.

Powder Cleanliness

Impurity control is of paramount importance for high-performance applications. Powder cleanliness is a major concern with atomized speciality alloys. These alloys are frequently used in applications with exacting combinations of strength, ductility, toughness, and fatigue resistance. In these conditions, there are nonmetallic inclusions in the powder that limit performance when the powder is consolidated. Inclusions may be introduced during melting and inert gas atomization; their source is the refractory tundish or pouring nozzle used in conventional gas atomization. The inclusions act as sites of stress concentration and can result in the initiation of fatigue cracks. This effect is of prime concern in components for aircraft engine applications.

Using a practicable induction melting technique, it is possible to closely replicate the composition of the melt stock in the resulting gas-atomized powder. Thus, speciality alloys based on aluminum, copper, nickel, cobalt, and titanium can be gas atomized to exacting compositional specifications. A partial loss of elements with a high vapor pressure or reactive elements can be quantitatively compensated for during melting prior to atomization. Primary sources of intermediate impurities are initial charge impurities, the melting atmosphere, the atomizing gas, and refractory ceramics (crucible, tundish, and tundish nozzle). In the case of the most critical superalloys, a bottom-pouring electroslag remelting furnace that discharges using a ceramic-free pouring nozzle to minimize all possibility of inclusion capture [81] has been developed. In the EIGA (Electrode Induction Melting Gas Atomization) process [82], prealloyed rods as an electrode are inductively melted without crucible. The metal liquid droplets from the electrode fall into atomization nozzle design and are atomized with inert gas jet. The EIGA process was used for titanium and niobium alloy powder production [83] and can also be applied to other alloys. Process developments in the EIGA technique [84] allow this process to be realized crucible- and ceramic-free, with larger electrode diameters up to 61 mm and increased melt flow rates of 26.4 kg/h. The optimized technique was applied for the atomization of pure Ti, Ti-6Al-7Nb, and gamma-TiAl based Ti-46Al-9Nb alloy powders. The oxygen level of the Ti-6Al-7Nb rod was about 1800 ppm; for the argon atomized powder, fraction $<20\ \mu\text{m}$, the oxygen content increases to 2300 ppm. The TiAl rod had an oxygen level of 560 ppm; for powder fraction $63\text{--}90\ \mu\text{m}$, this level was maintained.

The control of the interstitial level is very important, particularly in titanium alloys, titanium aluminides, and beryllium. The control of interstitial levels in titanium alloys and aluminides is particularly important because ductility is very sensitive to carbon, oxygen, nitrogen, and hydrogen impurities. Typical interstitial impurity contents of gas-atomized gamma titanium aluminide, alpha two titanium aluminide, and alpha titanium alloy powders are given by Lawley [13] and Yolton [85]. There is, in the main, no increase in carbon, nitrogen, and hydrogen over the starting material during atomization. The increase in oxygen content from the starting material to the $<500\ \mu\text{m}$ powder is typically 200 ppm [46, 85]. Nitrogen content appears to be independent of particle size but the oxygen content shows an increase from 800 ppm in $<500\ \mu\text{m}$ powder to 1020 ppm in $<45\ \mu\text{m}$ powder due to the large increase in surface area. In helium-atomized beryllium powder, it is possible to keep the oxide content to a relatively low level [13, 86].

Other Gas-Atomization Methods

Internal Mixing Nozzles

In an internal mixing atomizer, gas and liquid metal are mixed under pressure, and expansion and atomization occur at the nozzle exit into the chamber [87]. As shown in Fig. 4.47, the gas enters with high velocity through tangential inlets into a nozzle to which the liquid metal flows axially and is carried by the rotational gas flow in film form on the inner surface of the nozzle walls to the outlet in the bottom. The narrowing of the lower nozzle part forces the gas to accelerate so that the liquid film becomes thinner. At the outlet, the film breaks into small droplets. Concerning its working principle, this nozzle design is termed a prefilming spin nozzle. The lab melt feeding unit allowed the control of melt flow rates between 0.4 and

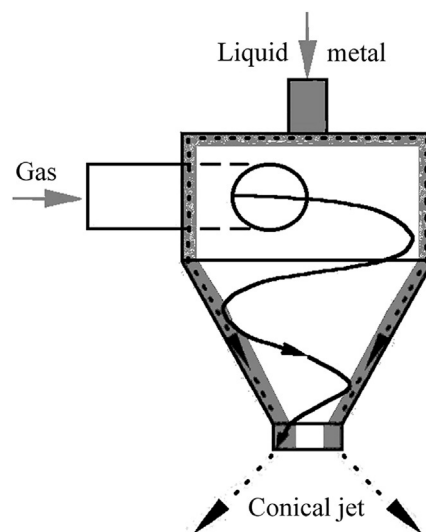


FIG. 4.47 Principle of the internal mixing nozzle.

5 mL/min for temperatures up to 473 K. The atomization conditions were as follows: atomizing gas was argon, gas pressure max 0.6 MPa, and initial metal was 62Bi-38Sn (weight). Its physical data were as follows: melting point 417 K, viscosity 2.2 MPa s at 473 K, surface tension 0.41 N/m at 423 K, and density 8.7 g/m³. The average particle diameters range from 14 to 25 μm . The pressure swirl hybrid-prefilming atomizer, described in Fig. 4.29, contains an internal mixing nozzle in combination with a ring gas atomizer.

The fundamental disadvantage of the internal mixing technique is the engineering difficulty of arranging to pressurize the melt to the same pressure as the gas. There are also problems with erosion of the ceramic nozzles employed because of the metal velocity. Normally only 1–3 m/s in a pouring nozzle could be expected to rise to the same order of magnitude as the gas velocities, that is, possibly about 100 m/s. Thus, applications are so far very limited.

Soluble Gas Atomization Process

The soluble gas-atomization process is also known as vacuum atomization (see Fig. 4.1K). This process [88] is based on the rapid expansion of gas-saturated molten metal, resulting in a fine atomization of molten droplets that forms as the dissolved gas, usually hydrogen or an argon hydrogen mixture, is suddenly released in an evacuated powder collection tank (Fig. 4.48). The droplets solidify at a rate of about 1000 K/s. The powder collection tank is cooled under vacuum while the powder is sealed and then backfilled with an inert gas. This technique is capable of atomization up to 1000 kg of superalloy in one fusion and produces spherical powder. This process has been employed on a commercial scale for LC Astroloy, MERL 76, and IN-100 production.

Ultrasonic Gas Atomization

Lierke and Griesshammeer seem to have been the first to report the experimental production of metal powders by ultrasonic atomization in 1967 [89]. Later, they achieved atomization of silver [90]. Many experimental studies have been carried out to evaluate particle size distributions. There are differences between low- (20–100 kHz) and high-frequency (up to 3 MHz) atomizers. Analytical studies work on two assumptions: either the breakup mechanism results from growing instabilities in a capillary wave pattern created at the surface of the liquid film, or it derives from cavitation phenomena [91].

According to capillary-wave hypothesis (Fig. 4.49), a thin layer of a liquid wetting the surface of a solid resonator that vibrates vertically to its surface plan forms a chessboard-like pattern of stationary capillary waves. This occurs when the vibration amplitude exceeds a threshold value. On further increase of the amplitude, ligament breakup of the liquid follows and droplets are hurled from the crests of the capillary waves. The key parameter is λ , the capillary wavelength.

Rayleigh [92] stated that

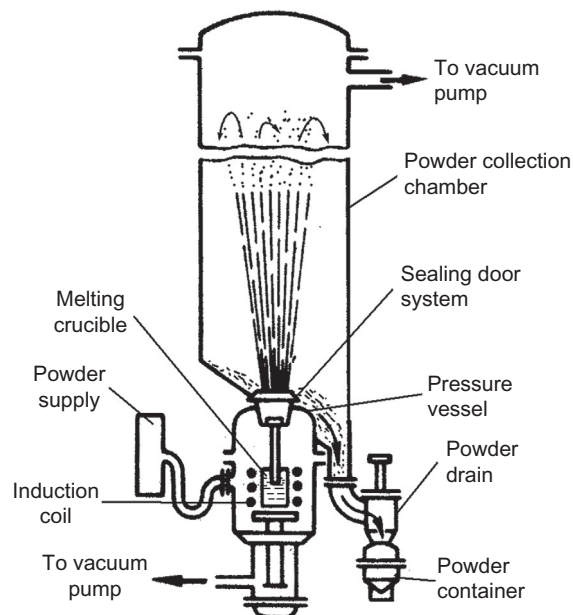


FIG. 4.48 Soluble gas atomization system.

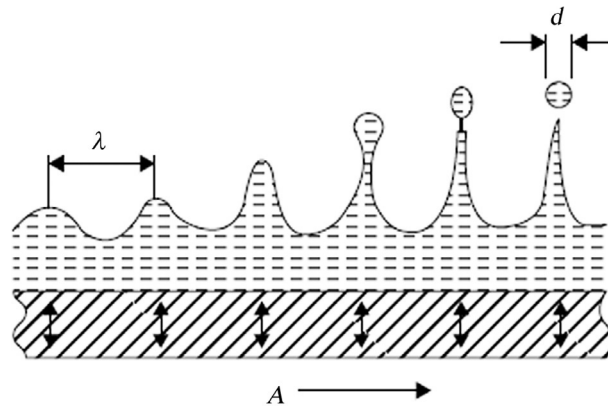


FIG. 4.49 Capillary wave atomization model.

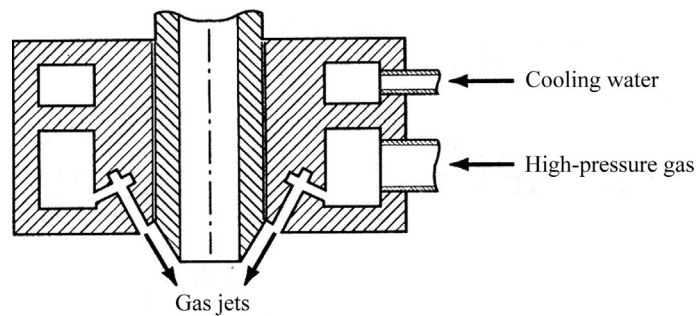


FIG. 4.50 Confined ultrasonic atomizer.

$$\lambda = \left(\frac{2\pi\sigma}{\rho v^2} \right)^{1/3}$$

where σ is the liquid surface tension; ρ is the liquid density; and v is the oscillation frequency. If the oscillation frequency in the liquid is half that in the solid resonator, then

$$\lambda = \left(\frac{8\pi\sigma}{\rho f^2} \right)^{1/3}$$

where f is the ultrasonic frequency.

Later, Ruthardt and Lierke [90] measured particle diameter amounting to 0.25λ for silver.

Theoretical predictions based on the capillary-wave hypothesis are numerous and essentially apply to low frequency, low flow rate atomizers whereas cavitation is supposed to occur at higher regimes [91, 93]. Yule [94, 95] has shown that capillary-wave atomization is not as orderly as foreseen theoretically. As an alternative, Dumouchel and Boyaval [96] used the maximum entropy formalism (MEF) to model size distribution. A detailed description of the MEF can be found in Kapur's paper [97]. In general, the MEF is a mathematical tool for the elaboration of probability distributions.

A confined ultrasonic atomizer is presented in Fig. 4.50. The ultrasonic designs use the Hartman tube principle to apply high-frequency pulsation to the gas stream, with gas exit velocities reported to be Mach 2–2.5 and the major pulsation frequency at about 100,000 Hz. The HEV's ultrasonic atomization unit includes an induction melting unit, atomizer, transducer, transfer tube, and tubular resonator [98]. Classification of the pneumoacoustic atomizers, the development of new devices, and procedures for ultrasonic gas atomization are given in the work [99, 100].

On HEV's (University of Applied Sciences of Western Switzerland) ultrasonic atomizer [98], a magnesium alloy, AZ63, and pure silver were atomized at 20 kHz. The atomizer, the induction melting unit, the transfer tube, the transducer, and the tubular resonator are the principal parts of HEV's ultrasonic atomizer. Experimental results show a spheroidal particle shape (Fig. 4.51); the powder fraction $<50 \mu\text{m}$ yields are about 65 and 71 vol% for magnesium alloy and silver powders, respectively.

Sono-Tek's founder, Dr. Harvey Berger, was the inventor of ultrasonic atomization technology, commercializing his patented invention in the late 1970s [101]. Early applications were the development of ultrasonic nozzles for use in home

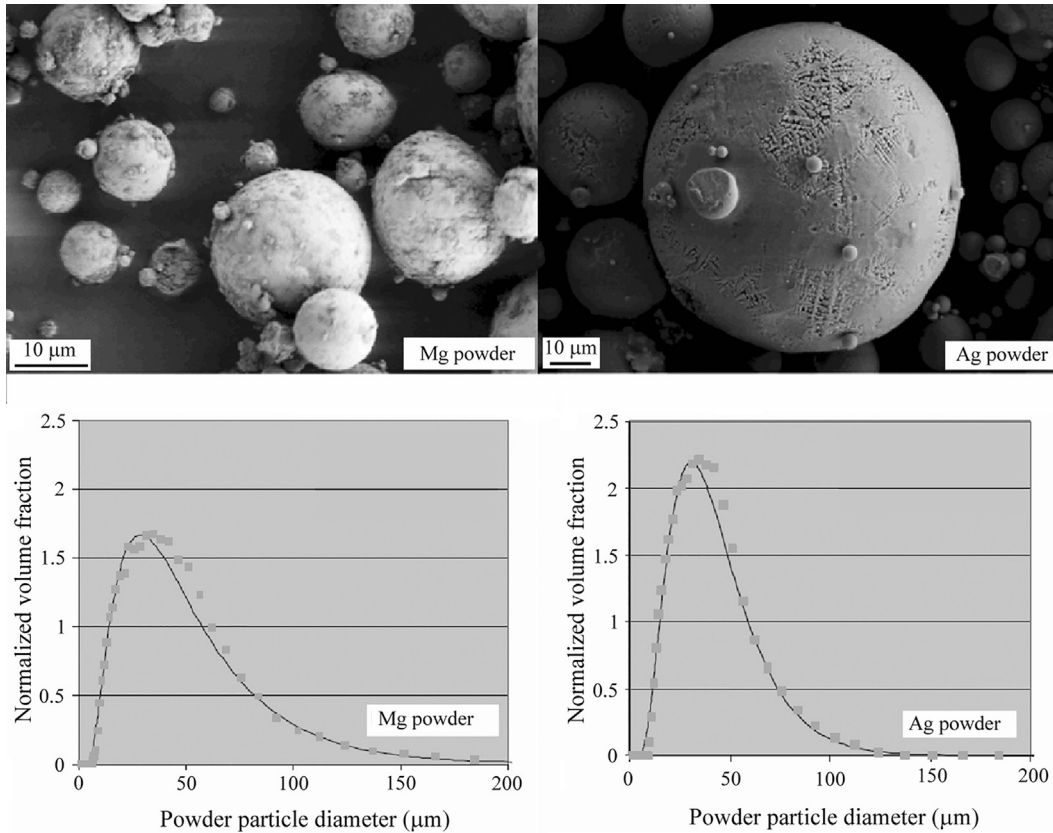


FIG. 4.51 Scanning electron micrographs of the ultrasonic atomized magnesium alloy and silver powders, and their size distribution. *Reproduced with modification from Cacciopoli G, Clausen B, Bonjour Ch, Hofman H. Ultrasonic atomization of metallic melts: modelling and case studies. In: Proceedings of PM2004 world congress, vol. 1. Shrewsbury, UK: European Powder Metallurgy Association; 2004. p. 59–64.*

heating oil burners and liquid fuel burners in portable power generation equipment. Currently, commercially available ultrasonic nozzles [102] have found wide application for molten metals atomization, especially when a precise particle size, such as for solder powder, is required.

Hot Gas Atomization

In practice, the hot-gas process has been partly motivated by an appreciation of the fact that it allowed the production of finer powders, and partly by the fact that it reduced or avoided the problems of nozzle freezing when processing lower melting point alloys (e.g., Li, Sn, Bi, Cd, Pb, Zn, and Al). This allows the use of smaller nozzles and pouring rates, which in turn allows convenient continuous production as well as the production of finer powders than is possible at higher melt flow rates.

The effect of gas temperature on particle size by constant gas mass flow is shown in Fig. 4.52. These data are the result of computation [103] based on dependence of the decrease in the median size of the powder on the square root of gas absolute temperature. In this case, a gas temperature to 473 K reduces the size by 11% and 673 K by 19%. The effect of gas temperature on gas consumption for constant particle size is shown in Fig. 4.53.

A calculation of the economic effect in the case of steel powder production [103] shows that going from 293 K to 473 K reduces costs by 16% and 673 K by 34% (this calculation assumes a gas cost of 0.14 €/m³ for nitrogen and an electricity cost for heating of 0.14 €/kWh). Heating gas to 473 K or even 673 K is not very demanding technically while reaching 1273 K is far more difficult. Besides that, savings from going from 772 to 1273 K are only a further 18%.

Hot-gas atomization was applied for the production of inexpensive copper powder for metal injection molding where powder costs currently form a high component part [2]. The powder with median diameter about 10 μm was produced by the following process parameters: pouring temperature 1673 K (melting point 1356 K) and atomization gas temperature 773 K. In the study [104], Zr-based (Zr₄₈Cu₃₆Ag₈Al₈) glassy powders are formed through both ambient and high temperatures up to 571 K inert gas atomization at various melt flow rates. Particles atomized under an ambient temperature were

FIG. 4.52 Effect of gas temperature on particle size. *Reproduced with modification from Dunkley JJ. Hot gas atomization—economic and engineering aspects. In: Proceedings PM2004 world, vol. 1. Wien, Austria: European Powder Metallurgy Association; 2004. p. 13–8.*

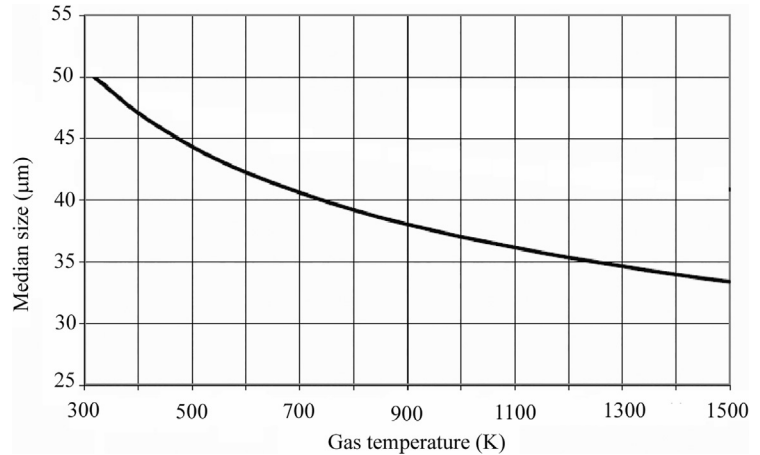
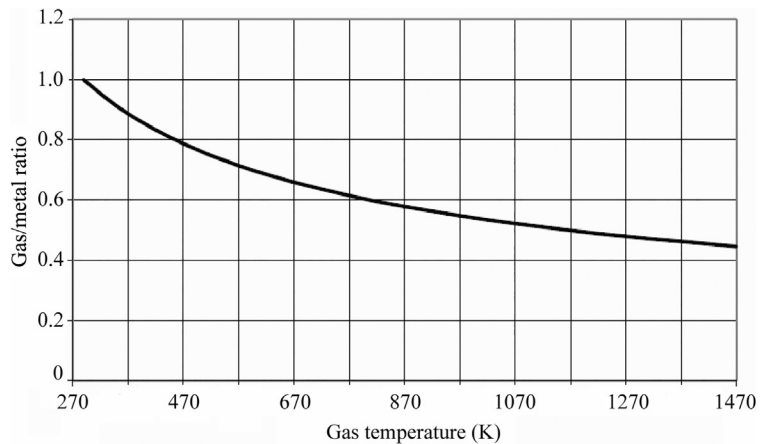


FIG. 4.53 Effect of gas temperature on gas consumption for constant particle size. *Dunkley JJ. Hot gas atomization—economic and engineering aspects. In: Proceedings PM2004 world, vol. 1. Wien, Austria: European Powder Metallurgy Association; 2004. p. 13–8.*



fully amorphous up to a particle size class of 90 µm for glass-forming alloys. It was confirmed that the smaller the particle diameter, the higher the amorphous fraction formed. However, the use of hot gas has not shown a great impact on the Zr-based glass-forming alloy regarding the mass median particle diameter δ_{50} and geometric standard deviation with a free-fall atomizer. Because of the small amount of fine powders generated with a free-fall atomizer (the amount of amorphous powder below 90 µm is in this study <20%), the closed-coupled atomizer offers advantages over the free-fall atomizer with regards to a higher output of fine and amorphous powders. Hot-gas atomization results in a higher output of fine powders, a smaller mass median particle diameter, a smaller gas-to-melt flow ratio (GMR), and constant amorphous fraction but to a lower sphericity.

However, hot-gas atomization leads to an increase in the time needed for solidification rather than to a decrease in median diameter, and that necessitates an increase in the size of the atomizer chamber.

Liquefied Gas Atomization

The atomization of melts with liquefied and cryogenic gases seems to have been developed in 1988 [105]. The so-termed liquefied gas atomization (LGA) is, in principle, similar to the well-established WA technique and results in comparable or even higher cooling rates than WA. During LGA, no oxidation occurs between the atomizing fluid and melt. Materials exhibiting high sensitivity to oxidation have been atomized via LGA, such as the rare earth NdFeB [106] and NiLa or special solder alloys. Starting with atomizing arrangements similar to WA (free-fall design), the technique has been further developed for the use of confined nozzles, similar or identical to the one used for GA.

Two identical inert gas-atomization units at ATZ-EVUS, a laboratory unit up to 30 kg and a pilot unit of 100 kg per batch, have been used for GA and LGA powder production [107]. Melting is done by inductive heating. The melt orifice diameters range from 1.7 to 4 mm, the melt superheat temperatures are typically 100–200 K, and the atomizing pressures

range from 1.0–25 MPa. Liquefied gas after cooling to cryogenic temperatures flows to the atomizer when the flow of the superheated melt begins. The mass median diameters range from 30 to 80 μm for NdFeB alloy, copper, and Sn-37Pb alloy. The cooling rate achieved is $>10^6$ K/s in the above laboratory size unit by melt flow rates up to 20 kg/min [106].

No commercial operator is known to use this method. More detailed data, including powder characteristics, economic effect, and safety engineering aspects, are necessary to evaluate the liquefied gas-atomization process.

Vacuum-Dynamic Atomization

This method is based on the use of the energy of two contrary rotating gas flows (Fig. 4.54) with the initiation of a tornado result (USSR Patent 1,082,566, Jan., 1984). However, the evaluations of vacuum level and the rapid expansion of gas-saturated molten metal are not known.

CENTRIFUGAL ATOMIZATION

Models of Centrifugal Atomization

According to the studies of Hinze [108], Tanasawa [109], Champagne and Angers [110, 111], and Halada [112] in centrifugal atomization, there are three basic droplet formation modes. These models conform to the rotating electrode process and are shown in Fig. 4.55. Their analysis is applicable to centrifugal atomization in general.

The direct drop formation (DDF) mode occurs at relatively small rotating speeds and small rates of liquid supply. In this mode, a lot of protuberances grow under the balance between centrifugal force and surface tension. When surface tension is lower than the centrifugal force, droplets are separated and ejected from the protuberances. The major part of every protuberance forms the main drops in large sizes. Its tail usually becomes satellites. Therefore, the typical powder size distribution in this mode has two peaks with equal numbers of large and small droplets.

The ligament formation (LF) mode occurs when the rate of supply of molten metal at the periphery of the electrode increases. Here the protuberances develop a larger amplitude than in the DDP mode before the Rayleigh instability breaks up the elongated ligaments. Droplet size increases and, though still bimodal, the weight fraction of the small and large droplets becomes similar as the liquid supply rate increases.

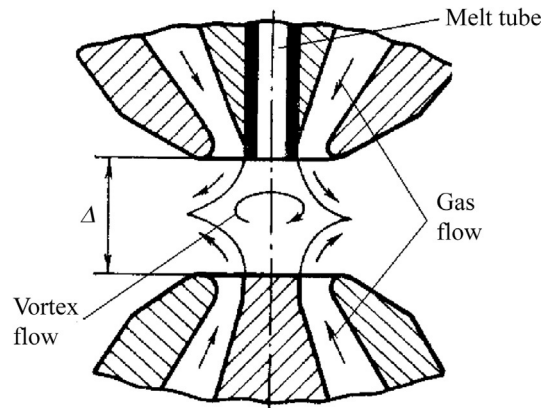


FIG. 4.54 Vacuum-dynamic atomization.

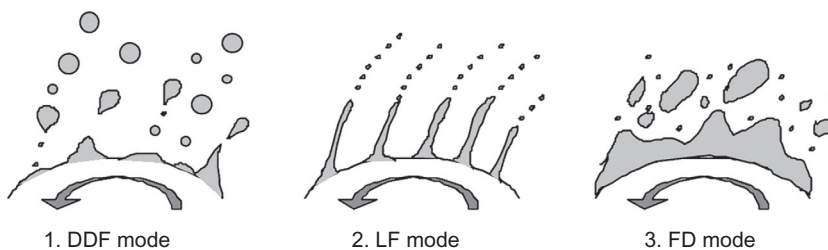


FIG. 4.55 Three disintegration modes in centrifugal atomization.

When the liquid flow rates are very high, ligaments become unstable and the disintegration mode changes gradually to formation disintegration (FD). The transition conditions among these modes have been studied experimentally in a broad range: $10^3 < We < 10^7$ and $10^2 < Re < 10^6$ by Masumoto [113]. The condition range for metal centrifugal atomization is Weber number 10^4 – 10^5 and Reynolds number 10^5 – 10^6 .

Champagne and Angers [110, 111] observed that, for various metals (e.g., Al, Cu, and Zn), the final droplet shape seen in the DDF mode is spherical. In the LF mode a more ellipsoidal shape is formed. Champagne and Angers [110, 111] discovered that the ratio of two parameters determines the transitions from the DDF to the LF and the LF to the FD modes:

$$X = \frac{\left(\frac{Q\omega^{0.60}}{D^{0.68}} \right)}{\left(\frac{\sigma^{0.88}}{\eta_L^{0.17} \rho_L^{0.71}} \right)}$$

where Q is the liquid supply rate (m^3/s); ω is the angular velocity of the anode (rad/s); D is the anode diameter (m); σ is the surface tension (N/m); η_L is the dynamic liquid metal viscosity (Pa·s); and ρ_L is the density of the liquid (kg/m^3).

The numerator includes only process variables while the denominator includes only the material variables. Using the above units for the process and material variables, the DDF to LF mode change occurs when $X = 0.07$. The second mode change to FD mode occurs when $X = 1.33$. These relations are plotted in Fig. 4.56. Thus, an increase in melting rate and angular velocity and a decrease in rotating anode diameter favor a transition from the DDF to the LF mode, and finally to the FD mode. Close agreement exists between model predictions of the transitions in atomization modes for various metals (Fig. 4.55).

Centrifugal atomization generally leads to a narrower spread in particle size than does gas atomization. The analysis of centrifugal atomization developed by Champagne and Angers allows for a quantitative prediction of mean particle diameter in the direct droplet formation mode. In its present form, the model gives no indication of the extent of droplet sizes. The median particle size δ_{50} for the rotating electrode process is approximately defined [114] by

$$\delta_{50} = \frac{K}{\omega\sqrt{D}}$$

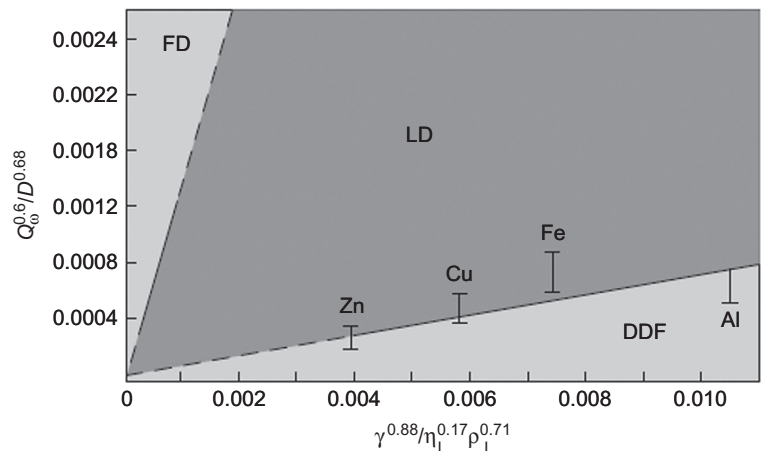
where K is a constant for a given alloy for a limited range of arc power.

In a simple model [115] that considers force balance between centrifugal force and surface tension forces, the particle size is expressed as:

$$\delta_{50} = \sqrt{\frac{A\sigma}{\rho_m\omega^2 R}} \quad (4.15)$$

where ω is the angular velocity (rad/s) of the rotating disc (or the electrode); R is the radius of the atomizer (or electrode) (m); ρ_m is the liquid density (kg/m^3); and σ is the surface tension (N/m). A is a constant with value 6 in the elementary case (spheroidal particle shape).

FIG. 4.56 Atomization mechanism domains in centrifugal atomization. Lawley A. *Atomization*. Princeton: Metal Powder Industries Federation Publishers; 2003.



Actual powder sizes are coarser than those predicted [91], which may be explained by the influence of viscosity, particularly at higher speeds. In effect, the molten film is “slipping” on the disc surface, making its speed less than the peripheral speed of the disc. If a term that is counteracting the centrifugal acceleration and that includes both the viscosity and the speed at the rim of the disc is added to the basic model (Eq. 4.15), the following relationship is suggested by Tornberg [41]:

$$\delta_{50} = \sqrt{\frac{A\sigma}{\rho_m \omega^2 R (1 - (\omega R)^n \eta)}}$$

where the constant $A = 4.8$ and the exponent $n = 0.93$.

Centrifugal Atomization Methods

There are several different types of the centrifugal atomization process (Fig. 4.1), which are discussed. In general, centrifugal atomization methods are far more energy efficient than gas and water atomization, where only about 1% of the jet energy is used in the disintegration of the metal stream [13]. In contrast, the energy used in centrifugal methods is low as it all goes into the acceleration of the metal droplets instead of into the atomizing fluid, as in the case of the two-fluid techniques. Centrifugal atomization also generally leads to a narrower spread in particle size than does gas atomization (see Fig. 4.2), with σ_g as low as about 1.4 in some cases.

As the process depends on the solution to the problem of finding a compatible material for the spinning disc or cup, the applications that have been and are currently used on a significant industrial scale are quite distinct. They are selected in order of ascending melting point of alloy.

Spinning Disc Atomization

Solder powder for electronic applications has a very demanding specification: it must be perfectly spherical and satellite-free, it must be very low in oxygen content (~ 100 ppm), and it must have a very narrow size distribution. Attempts to make this product with inert gas atomization have practically ceased as yields are as little as 5% and the avoidance of satellites is very difficult.

In the United States, Europe, and Japan, there are many producers using spinning disc methods to make this product. This is possible because a steel disc is well wetted by ordinary Sn63Pb37 solder and is not very quickly eroded. A disc with a diameter of 40–100 mm running at speeds of 30,000–60,000 rpm can produce this material with good yields of 30%–70% and at rates of 50–100 kg/h.

When used with higher melting point metals, it is difficult to run at the level of speeds that are used on solder because of the need to increase the plant diameter. However, there are markets for coarser powders of zinc (alkaline batteries), aluminum (chemical), and magnesium (flares) that are made by this process. In all cases, the cup is 100–200 mm diameter, running at moderately high speeds from 3000 to 10,000 rpm. The chamber size needed is very large, up to 12 m in diameter, but productivity can be very high. Battery applications commonly require $-600 + 100 \mu\text{m}$ zinc powder. Using a 5 kW spinning cup, 98% can be achieved at outputs of several tons per hour and with compressed air costs.

Course aluminum powder is also produced in this way, but because of the large size of plant needed to freeze large droplets, it is done in open air, which produces a needle-shaped powder. In this case, a perforated steel or cast iron cup is used to make a series of streams of metal, which break up into needles due to the oxide film on them. Production is probably thousands of tons per year.

The spinning cup water granulation process [116] allows an increase in the cooling rate and a notable decrease of the size of plant, owing to cooling the molten droplets in water. Thus, the chiller chamber size is only 1.2–1.5 m in diameter in comparison with 12 m in diameter in the open-air granulation. chapter 16 includes more detailed information about this technique.

Sheikhaliev et al. studied the influence of melt flow rate, melt feeding modes, and environment properties on the quality of the finished solder powder [117]. Experiments were carried out on Sn-39Pb and Sn-3Cu solder alloys in the plant using both melt feeding by a free fall 1–2 mm diameter melt stream and a prefilming nozzle generating a hollow cone melt film (Fig. 4.57). This nozzle function on the centrifugal effect is named the “pressure-centrifugal-atomizer” (PCA).

A scanning electron micrograph of the spinning disc atomized Sn-3Cu solder by free-fall melt feeding is represented in Fig. 4.58. The particles are spherical, satellite-free, and narrow in size.

Table 4.5 contains the data that characterize an effect of atomization conditions on the solder powder particle size. Powder produced by a PCA atomizer had a finer particle size distribution in comparison with one made by free-fall melt

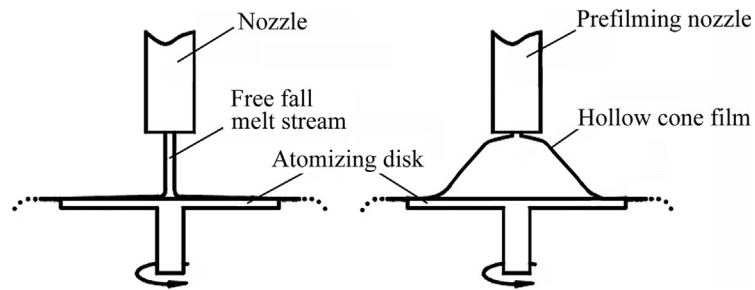


FIG. 4.57 Schemes of melt feeding on spinning atomizing disc.

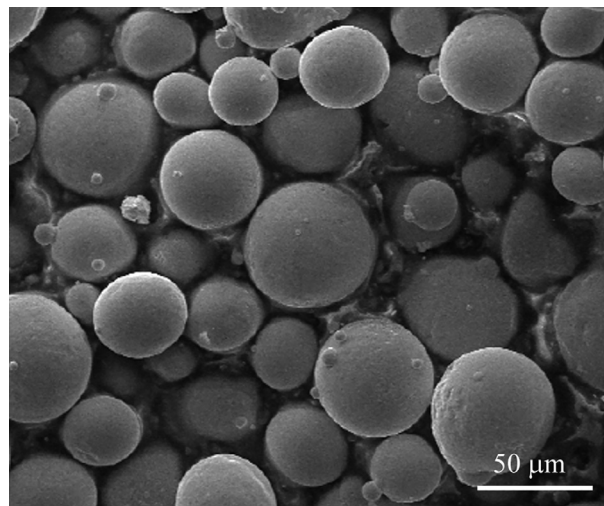


FIG. 4.58 Scanning electron micrograph of Sn-3Cu solder powder made by free fall melt feeding on spinning atomizing disc.

TABLE 4.5 Effect of Atomization Conditions on the Solder Powder Particle Size

Melt Feeding Mode	Gas Type	Gas Density (kg/m ³)	Rotation Speed (rpm)	Melt Flow (kg/h)	W _g /W _m (W/W)	Particle Size	
						δ ₅₀ (μm)	σ _g
Free fall	Nitrogen	1.25	50,000	60	—	60	—
Prefilming nozzle	Nitrogen	1.25	50,000	60	—	25	—
Free fall	Nitrogen	1.25	40,000	20	—	25.9	1.6
Free fall	Nitrogen	1.25	40,000	40	—	39	2.5
Free fall	Nitrogen	1.25	40,000	60	285/600	78	—
Free fall	Helium	0.18	60,000	40	110/—	—	—
—	Argon	1.8	40,000	—	365/—	—	—
—	Nitrogen ^a	0.1	60,000	—	80/—	—	—

^aAt pressure of 10³ Pa; W_g—consumption power by free running in gas environment; W_m—consumption power by melt atomization; σ_g—geometric standard deviation.

feeding mode. The authors [117] reported that the thickness of the PCA hollow cone melt film formed by contact with the disc becomes about 15 μm ; therefore, it will need less energy for atomization along with finer powder forming. Decreasing the melt flow rate from 40 to 20 kg/h results in increasing a finer particle yield, and particle size distribution becomes more narrowly describable by decreasing σ_g from 2.5 to 1.6. As is also seen, using a lighter gas allowed the production of finer powder. A powder made in a helium atmosphere had a granulometric composition with 38 μm median diameter while the powder manufactured in nitrogen had one with $\delta_g = 76 \mu\text{m}$. The authors also reported the calculation of consumption power by free running in various gas environments and consumption power by melt atomization.

Rapid Solidification Rate Process

The rapid solidification rate (RSR) process is another design of a centrifugal disc or cup atomization, which was developed for superalloy powder production. To overcome the problems of the material in handling high melting and aggressive alloys, the process [118] employs a high-speed, water-cooled rotating disc (20,000–50,000 rpm), which breaks up the molten metal stream. To enhance solidification rates, the resulting droplets are then struck by high-pressure helium gas as they leave the periphery of the rotating disc. Powders produced by the RSR process are spherical, satellite-free, and have smooth surfaces. Particle sizes are usually below about 200 μm with a mass median particle diameter $< 90 \mu\text{m}$ and a low standard deviation in the range 1.4–1.6.

RSR facilities currently in use incorporate closed-loop helium recirculation. Based on Ni-base alloys, the largest unit has a melt capacity of about 900 kg with an atomization chamber close to 5 m in diameter. In the intermediate size unit, melt sizes are 135 kg with an atomization chamber of about 2.3 m in diameter. Production rates can be varied between 0.05 and 0.3 kg/s for Ni-base alloys. Typically, RSR droplets smaller than 100 μm in diameter cool at rates of about 10^5 K/s . Apart from these operating variables, the superheat of the melt has a strong influence on particle size and hence the particle cooling rate. More detailed data can be found in chapters 15 and 16.

Melt Spinning Roller Technique

At present, the maximum melt cooling rate has been achieved under heat abstraction from a melt by means of a contact with metallic substrate. The main conditions for the advance of the high melt cooling rate due to heat conductivity are the following:

- Minimal loss of heat during carrying from furnace to cooling point.
- Minimal melt thickness in the line of the heat sink.
- High heat conductivity of freezing metallic material (substrate).
- Sufficiently high melting point of the substrate.
- Good heat contact (first of all, cleanness of the substrate surface) of the freezing and cooling materials.

As freezing material, pure copper or its alloys (e.g., beryllium bronze) mostly serve. For good heat contact, the substrate surface is thoroughly polished. The most advanced method of obtaining particles (ribbons, flakes) by means of their freezing on a substrate is the spinning roller technique [116]. A liquid metal stream (Fig. 4.59) collides with the surface of a rapidly rotating roller and wets it. At the contact point, a liquid metal bath is formed. The moving roller surface expands the bath into a ribbon, which begins to move with the same velocity as that of the roller surface. The solidified ribbon is released from the roller under the action of centrifugal force.

The cooling rate of liquid metals achieves 10^5 – 10^7 K/s , depending on ribbon thickness, which is changed from 20 to 80 μm ; the roller circumferential speed is $\sim 30 \text{ m/s}$ [115] and output of the Al alloy 4–6 kg/min.

The phenomenon of heightened solubility by such cooling rates becomes possible. Thus, for example in aluminum alloy ribbons, an increase of the nonequilibrium solubility of scandium up to 2 wt% was achieved [119]. Alloying of aluminum with scandium leads to hardnesses of 950, 1200, and 1800 MPa for scandium concentrations of 0.6, 1.0, and 2.0 wt%, respectively (significantly higher than the maximum hardness achieved for aluminum alloys by traditional technology, i.e., 800 MPa).

At the plant shown in Fig. 4.60, a flaky magnesium powder is manufactured [120]. A $\text{Mg}_{97}\text{Zn}_1\text{Y}_2$ alloy was melted by high-frequency induction heating in an argon atmosphere and a flaky powder was produced by spinning roller atomization. In the experiments, the distance between the melt nozzle end and copper roller surface was 0.3, 15, and 30 mm while the roller circumferential speed was 30, 40, and 50 m/s, respectively. As a result, the flaky powders ranged from 20 to 65 μm and the Vickers hardness from 104 to 134, depending on the experimental conditions produced.

FIG. 4.59 Aluminum alloy ribbon obtaining on melt spinning roller. *Courtesy of IPMS.*

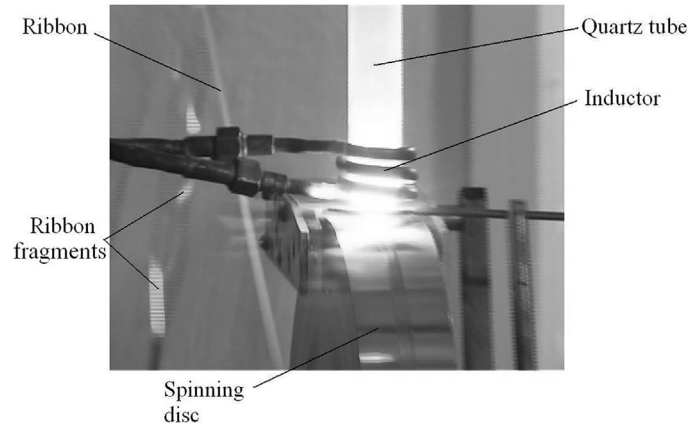
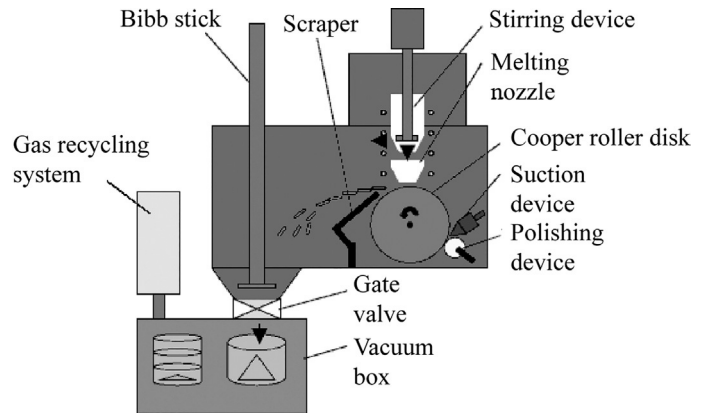


FIG. 4.60 The diagram of flaky powder production by melt spinning roller technique.



The melt spinning roller technique is widely used in laboratory studies. A closed processing system in an inert gas atmosphere (O_2 , $H_2O < 0.5$ ppm) is employed for high reactivity metals [121]. The details of this processing system realizing a single-roller melt spinning method are described in the article [122].

Rotating Electrode Atomization

In the rotating-electrode process (REP), one end of a metal bar is melted while it is rotated around its longitudinal axis (Fig. 4.1E). The molten metal is ejected by centrifugal force in the form of droplets from the periphery of the bar. The REP process was developed by Nuclear Metals, Inc. and patented [123, 124].

In the original process, the consumable rotating bar is the anode of direct current power circuit and the permanent (non-melted) stationary cathode is either a cooled tungsten-tipped device or a transferred-arc plasma torch. When the latter mode is used to melt the end of the rotating anode, the atomization process is termed the “plasma rotating electrode process” (PREP). A chamber of 2440 mm in diameter is used with the circular section oriented. Anode rotational speeds are normally 1570 rad/s. Melting of the anode is carried out in an inert atmosphere. Helium gas enhances both arc stability and the convective cooling efficiency of the atomized droplets.

Powder particles produced by REP and PREP are spherical with smooth, high-quality surfaces. The particle size range is typically from 50 to 400 μm with a mass median particle size around 200 μm [13]. Particle cooling rates are lower than in water or gas atomization. From secondary dendrite arm spacing measurements, the cooling rate is $\leq 10^2$ K/s, depending on the gas condition in the chamber and the particle size.

However, a major drawback is the mechanical limitations on rotational speed, which limit the minimum median particle size to about 50–150 μm [3]. Also, the cost of making a high-quality bar of metal is very significant while productivity is low and energy consumption high compared with other techniques.

OTHER METHODS

Impact Atomization

Impact atomization was developed [125] for producing rapidly solidified particulates. In this method, a molten alloy and volatile liquid coolant are fed simultaneously to a rapidly rotating impeller. As the molten alloy is atomized, the coolant vaporizes; the necessary heat of vaporization of the coolant is taken from the droplets as they solidify. Patents covering this process were issued to the Dow Corning Corporation [126, 127]. Powders have been prepared from a variety of stainless steels, nickel, copper, and a glass-forming alloy [125]. Coolants used included water, liquid ammonia, methanol, and hexane at flow rates from 60 to 200 L/min, depending on the heat of solidification of the alloy, the heat of evaporation of the coolant, the degree of superheat, and the molten metal feed rate.

This process has been used in Argentina where, since 1997, two commercial plants have been operating using induction melting furnaces with 80 and 500 kg capacity, respectively [128]. Both plants include furnaces, tundishes, rotating impellers, atomization tanks with water, reservoirs of circulating water, and pumps feeding circulating water to the impeller. The speeds of impeller rotation are from 2000 to 3500 rpm depending on alloy type, required particle size distribution, and powder apparent density values. The commercial bronze (Cu-5Sn-5Zn-5Pb) powder contains the size fraction $\leq 44 \mu\text{m}$ up to 26 wt% and the size fraction $\geq 147 \mu\text{m}$ max 20 wt%. For the 2.2–2.5 t/h atomized powder yield, a 10 kW belted drive is used.

Vibrating Electrode Atomization

Powder is atomized at the molten end of a vibrating consumable electrode in rod form that is continuously fed between rollers into an atomization chamber. A water-cooled rotating electrode of copper or graphite is located opposite the end of the consumable electrode. The rollers are attached to an electrodynamic oscillator, which transfers vibration to the rod electrode. Thus, the electrode forms a resonant rod with one free and one fixed end. Atomization takes place in an inert atmosphere when the arc is struck between the rotating electrode and the vibrating end of the rod electrode.

In the facility described in the literature [129], currents between 600 and 1200 A were generated at a potential between 30 and 60 V. Electrode vibration frequencies up to 500 Hz were evaluated. Powder particles are spherical with mass median sizes typically in the range 300–500 μm . The vibrating rod diameter range is 1–4 mm and the feed rate 1.7–4.3 m/min. Disadvantages of the vibrating electrode atomization are that particles are coarse, productivity is low, and cost is high.

Melt Drop Orifice Technique

There are several types of such a technique, which include impulse atomization (IA), the melt drop vibrating orifice method, and the pulsated orifice ejection method.

Impulse Atomization Method

A schematic of the process is shown in Fig. 4.1J. This unit includes the impulse generator, the mechanical drive, a tundish, and a nozzle plate complete with orifices [130]. There are two modes of impulse atomization operation: the first (gravity impulse mode) is the generation of monosized granules larger than 1 mm in diameter, and the second (impulse mode) is the atomization of droplets with a narrow size distribution $< 1 \text{ mm}$ up to 150–180 μm . In the impulse mode of operation, by varying the plunger acceleration, orifice size, orifice shape, melt superheat temperature, and gas atmosphere type, the powder particle size, distribution, shape, and microstructure can be controlled to the required specifications. In gravity impulse mode, the melt stream free falls out through the orifice and impulses are applied to generate millimeter-sized droplets. The powders have been produced in an experimental tower 0.5 m in diameter and 4 m height. In the atomization chamber, the quiescent gas atmosphere into which the melt has been atomized includes helium, nitrogen, argon, and air. The nozzle plate contains > 500 orifices. Standard refractory materials are used for the tundish, plunger, and orifice plate. There are no temperature limitations to the use of impulse atomization, provided an appropriate refractory material is available for use. For example, a nickel-aluminum alloy was atomized at 1873 K.

Table 4.6 includes a summary of the materials and range of particle size data reported in Ref. [130]. The powders have a narrow particle size distribution; the geometric standard deviation is in the 1.1–1.6 range, typically 1.4, for the impulse mode.

In the impulse mode of operation, mass flow rates of 225 kg/h have been attained in pilot scale tests with, to date, 2.5 h of continuous operation with zinc. This corresponds to a mass throughput of 7300 kg/(m² h) based on the area of orifices in the

TABLE 4.6 Powders and Granules Produced Using Impulse Atomization Method

Metal or Alloy	Atomization Mode	Average Particle Sizes	
		Unit	Value
Aluminum	Impulse mode	μm	310
Aluminum	Gravity impulse mode	mm	2–10
Al-(5–24wt%)Cu alloys	Impulse mode	μm	250–710
Al 6061 alloy and Al 6111 alloys	Impulse mode	μm	250–850
Al 357 alloy	Impulse mode	μm	560–700
Al-(0.1–8.0wt%)Fe alloys	Impulse mode	μm	400
Al-(10–24wt%)Sr alloys	Impulse mode	μm	1000
Al-Al ₂ O ₃ composite powders (5–20vol% of 35 μm reinforcement)	Impulse mode	μm	1000
Copper	Impulse mode	μm	200–1400
Bronze 90/10 and bronze 94/6	Impulse mode	μm	180–720
Pb-(10–12wt%)Sn alloys	Impulse mode	μm	200–1000
Magnesium	Impulse mode	μm	850–1000
Magnesium	Gravity impulse mode	mm	2 and 4
Mg-9Al-1Zr alloy	Impulse mode	μm	850–1000
AZ91D alloy	Impulse mode	μm	850
Knife alloy	Impulse mode	μm	1000
90Ni-10Al alloy	Impulse mode	μm	350
34Ti-45Cu-1Zr-8Ni alloy	Impulse mode	μm	350
Zinc	Impulse mode	μm	150
Zn-500ppm Pb	Impulse mode	μm	250

nozzle plate, while the mass throughput for aluminum ranges in these experiments from 2000 to 3000 kg/(m²·h). The mass flow rate attained with the gravity impulse mode was 15 kg/h for 2 mm magnesium granules. Alcoa has developed a forecast model for the conversion cost of a commercial gravity impulse unit [130].

In the work [131], a thermal model of melt droplet cooling coupled with the temperature of the primary phase in the impulse atomization system is considered. It is based on in situ measurements of droplet size, velocity, and temperature during moving of droplets with subsequent solidification.

Melt Drop Vibrating Orifice Method

In this method, molten metal contained in a pressurized crucible is subjected to vibratory oscillations. Forcing the metal through a nozzle at the bottom of the crucible and into a vacuum or inert gas chamber causes it to form a jet and break up into uniform droplets. The technique has been demonstrated with aluminum, beryllium, copper, lead, and some superalloys [132] and has been proposed for solder [133]. The technique was in limited industrial use in the 1990s, making precision solder balls for electronics with sizes in the range 500–1000 μm. It is limited as production is related to the square of particle size and nozzle blockage is a problem for orifices in the 200–20 μm range.

Pulsated Orifice Ejection Method

This method is intended for the production of monosized spherical particles [134]. Fig. 4.61 shows a schematic diagram of a pulsated orifice ejection method. A piezoelectric actuator was used as a driving device of a metal diaphragm, in which the

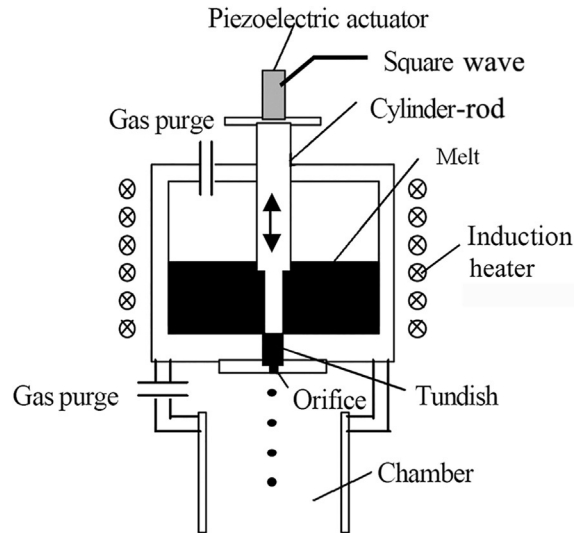


FIG. 4.61 Schematic illustration of pulsated orifice ejection apparatus.

maximum displacement was $14.7\ \mu\text{m}$ and the frequency was $69\ \text{kHz}$. Rectangular waves were generated by a function generator for controlling the output waveform of a power amplifier. A hole about $0.2\ \text{mm}$ in diameter, as an orifice, was machined at the center of the bottom of the tundish. Each pressure pulse produced one melt droplet. The apparatus allows the preparation of particles having a very narrow particle size distribution with size deviation $<2\%$ of mean particle size. It has been found that the pulsated orifice ejection method is applicable for preparing monosized particles of various metals and alloys. For example, the monosized Sn-3.5 wt%Ag powder with mean particle size of $187\ \mu\text{m}$ with 0.8% deviation was demonstrated.

Roller Atomization

In roller atomization, a molten metal stream is fed between rapidly rotating twin rollers (Fig. 4.1G). Its feature is that little conductive heat transfer between the liquid metal and the rolls takes place [135]. This distinguishes roller atomization from the spinning roller in which rapidly solidified ribbons or flaky particles are produced. Epoxy and phenolic resin coatings on the rolls were found to satisfy the heat transfer requirements for temperatures below $573\ \text{K}$ because of poor thermal stability. Epoxy/alumina roll coatings have been used for the atomization of higher melting point metals and alloys. The original atomization facility consisted of a pair of $150\ \text{mm}$ diameter rolls contrarotated at speeds up to $1250\ \text{rad/s}$ with a roll gap in the range $50\text{--}100\ \mu\text{m}$. The process has been used to atomize a range of metals including lead, tin, aluminum, and copper at metal flow rates up to $6\ \text{kg/min}$. The particle shapes can be irregular, acicular, spheroidal, or flaky, depending on the operating conditions and the metal properties. The spheroidal particles are relatively coarse; mass median particle diameters for Sn powder are in the range $250\text{--}680\ \mu\text{m}$. Primary operating variables are roll speed, roll gap, metal flow rate, metal stream velocity, and metal superheat.

Plasma Atomization Process

This process (Fig. 4.1C) was developed to produce fine spherical titanium powder using titanium wire as the starting material [136]. The wire is fed into the apex of three plasma torches, where it is melted and atomized in an argon atmosphere. Droplets are then cooled during flight in the argon atmosphere with a cooling rate in the range $10^2\text{--}10^3\ \text{K/s}$ and then solidify, forming spherical powder particles. Spherical titanium and Ti-6Al-4V alloy powders with diameters from 5 to $150\text{--}250\ \mu\text{m}$ have been produced commercially in four grades, differing as to particle sizes. The oxygen content depends on particle size and is in the range $0.1\text{--}0.3\ \text{wt}\%$. The flow rate varies depending on particle size up to $150\ \text{kg/day}$ [137]. PyroGenesis proposes the use of plasma-atomized titanium powders for producing porous filters, applications in injection molding and thermal spray processes, and biomedical applications.

Explosive Atomization

Electrical Explosion of Wires Technology

Electrical explosion of wires technology (EEW) is a process of explosive destruction of a metal wire under the action of great density current of 10^6 – 10^9 A/cm² [138]. EEW is characterized by the following peculiarities: time of explosion is 10^{-5} – 10^{-8} s; temperature at the moment of explosion can reach a value more than 10^4 K and pressure $\sim 10^9$ Pa; and velocity of the product recession is from 1 to 5 km/s. The material of the wire transmutes into particles of nanosized range (10–100 nm) in accordance with certain conditions. The process can be carried out either in a gas or liquid environment. More detailed EEW data can be found in Chapter 9.

Steam Explosion method

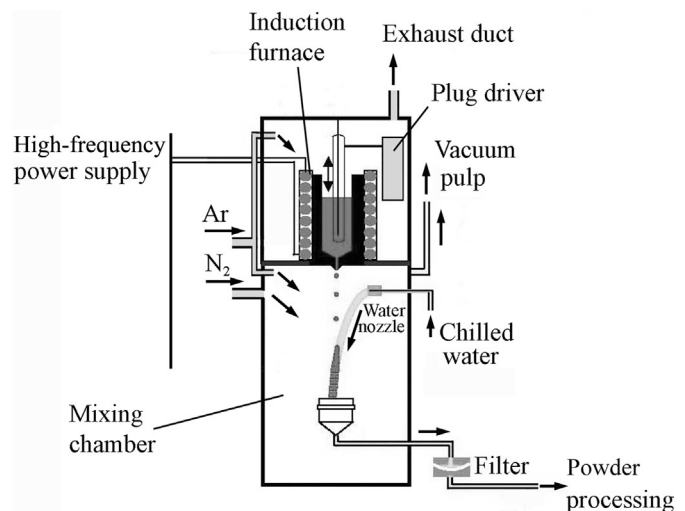
The atomization of melt by means of the steam explosion (CANOPUS) method allows, according to the data [139], an achievable cooling rate of the melt of 10^8 K/s. This method was achieved on a laboratory installation. Molten metal held in a crucible flows out through a small orifice in the base, drop by drop, at a set time interval. The drop of melt entering the stream of cooled water (or water salt solutions) causes an explosive formation of steam and results in melt atomization (Fig. 4.62). For the production of the Al₈₉Fe₁₁ alloy, the cooling liquid used was a 25% water solution of calcium chloride. Powder particle sizes obtained were in the range of 30–400 μ m. However, no commercial operator is known to use this technique.

Flame Spray Pyrolysis

The synthesis of nanoparticles by flame spray pyrolysis (FSP) is a newer but already well-developed process in terms of product diversity. Many elements of the periodic table can be turned into oxides, salts, or even metal nanoparticles in laboratory-scale reactors with production rates of a few grams per hour [140–143]. In these reactors, low-cost metallic precursors (e.g., hexamethyldisiloxane) dissolved in a liquid fuel (e.g., xylene) are supplied into a two-substance nozzle. Pure oxygen is utilized as the dispersion gas and atomizes the liquid precursor in fine droplets with a mass median diameter of ~ 10 μ m. Flamelets feed by a mixture of methane and oxygen allow a permanent ignition of the spray. Droplet evaporation, nucleation, cluster formation, coalescence, and finally agglomeration of product nanoparticles are determined as respective process steps in FSP. The combustion of organic solvents and precursors causes a huge release of thermal energy with temperature > 2300 K within the flame.

It is supposed that correlation between product quality (particle size, purity, etc.) and production rate can be considered as a trade-off in large-scale production facilities [144]. For industrial large-scale nanoparticle production via FSP, a new precursor atomization concept consisting of a combination of a liquid hollow cone (pressure swirl nozzle) and a dispersion gas nozzle (discrete jet nozzle) was presented [145]. Experiments were done under nonburning conditions with water and compressed air to gain impressions of the spray pattern and nozzle functionality (Fig. 4.63). Based on the experimental data

FIG. 4.62 Schematic of steam explosion CANOPUS experimental installation.



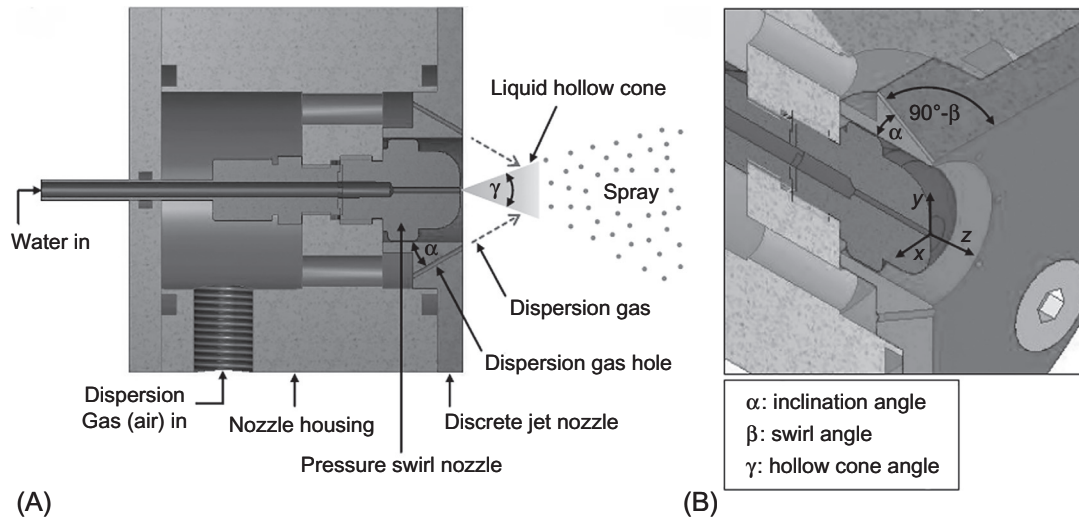


FIG. 4.63 Liquid hollow cone nozzle (pressure swirl nozzle) adapted with custom-made dispersion gas nozzle (discrete jet nozzle); view onto cross-sectional plane (A) and cross-sectional plane as well as sectional plane under inclination angle α to illustrate swirl angle β (B). *Courtesy of Universität Bremen.*

in terms of mass median droplet diameter δ_{50} and spray angle, a combination of the pressure swirl nozzle (γ) and the discrete jet nozzle (number of holes/ α/δ) as $\gamma = 70$ degrees and $8/30^\circ/15^\circ$ was optimized.

GRANULATION

Granulation is a term that is used to define two dissimilar processes. In one definition, granulation is defined as the production of metal by the atomization of molten metal. These processes have been discussed above. The other definition is the most commonly used spray drying and spray granulation techniques. Granulation is the purposeful agglomeration of fine particles into larger clusters to improve certain powder properties. For example, bulk powders characteristically have low density, do not readily flow, are dusty, and have low thermal conductivity. When properly granulated, the same powder pours easily, exhibits a high and uniform bulk density, does not “dust,” and more efficiently transfers thermal energy.

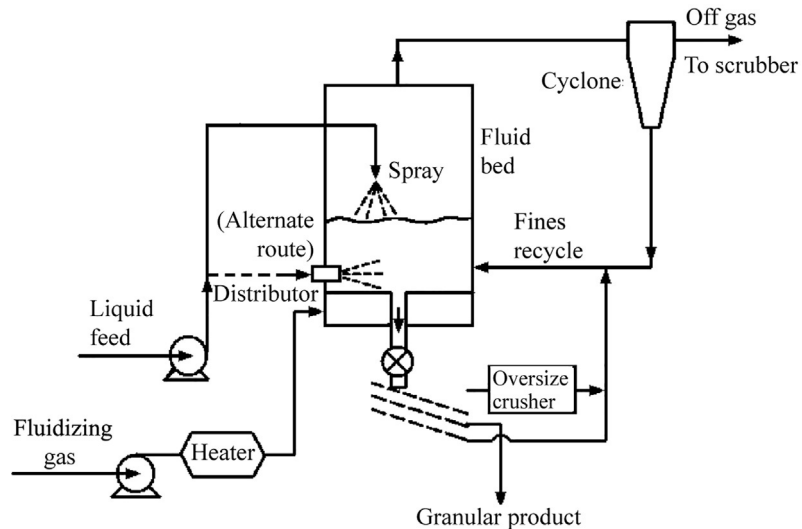
Spray Granulation

The basic method for making granules in a fluidized bed can be by the combination of the hot gaseous fluidized bed and a two-fluid spray nozzle. A binding liquid or solution is spread onto a bed surface of fluidized particles or is sprayed directly into the bed (Fig. 4.64). It tends to show that, compared to seed particles, larger spray droplets generally result in the formation of agglomerates, which is influenced by the variation of operating conditions. In relation to granule growth of simultaneous coating and agglomeration in a hot fluidized bed, the size distribution and growth rate of granules under continuous operation can be derived from the material balance of the bed particles. Granule size increases as the fraction of the bed exposed to the binding liquid is reduced and the spray nozzles are adjusted to give coarser droplets. Increasing the intensity of bed agitation (with higher velocity) decreases the size of granules. There is an upper limit on granule size because of the tendency of the powder bed to defluidize. However, spray granulation can form larger granules than are usually possible by spray drying because of a longer residence time.

Both spray granulation and spray drying are scalable technologies and provides the means for producing bulk quantities of nanophase composite powders at a low manufacturing cost.

A direct current plasma-heated fluidized bed was applied to the granulation of spheroidal alloy grains from metal powder mixtures [146]. From a mixture of aluminum powder (74–88 and 125–149 μm) and iron powder (149–210 μm), alloy grains from 1 to 5 mm in diameter were produced. The grains exhibited a dense homogeneous core and a porous nonhomogeneous shell structure. A fluidized bed process facilitates the production of contamination-free pyrophoric rare earths and abrasive ceramic powders [147]. The production of exactly limited particle fractions is an important process for rare earths (Sm-Co, Nd-Fe-B) and ceramic oxides (oxides, carbides, nitrides, and borides) products.

FIG. 4.64 Fluidized bed spray granulator.



Spray Drying

Spray drying is a powder production process in which a slurry or a solution is atomized into droplets in a chamber through which heated gases, usually air, are passed. A typical spray dryer utilizes a disc atomized with cocurrent air flow. This process is described in [chapter 14](#). Spray drying offers several advantages over other powder-processing techniques, particularly in applications requiring agglomerates for subsequent pressing and sintering operations. Spray drying also is one of the most economical ways of drying slurries.

Control of Powder Properties

Most of the applications of spray drying in the PM industry require the formation of free-flowing agglomerates, including the powder injection molding process. Many of these powders are used for producing pressed parts. Therefore, the agglomerate size distribution and bulk density are the two most important properties of spray-dried powders. Agglomeration is achieved by using a binder.

Agglomerate size distribution is a function of atomization conditions and properties of slurry. Commonly, a lower solid content yields a finer average agglomerate size. The maximum attainable solid content varies with the material, but usually can be increased by using deflocculating or suspending agents.

Bulk density is a function of the solid content of the slurry additives. Lower bulk densities are generally achieved from slurries with low solid contents. Also, excessive inlet temperatures can cause lower bulk densities. Rapid evaporation of the liquids causes the partially dried droplets to expand rapidly, thus decreasing density. Introduction of frothing agents may draw air into the slurry, which also leads to lower bulk densities. Typically, frothing agents are not added in PM applications.

The moisture content of a powder can be controlled by the inlet and outlet temperature of the spray dryer in conjunction with the slurry feed rate. Moisture levels below 0.1% are possible. For a given airflow and inlet temperature, outlet temperature is controlled by the rate of slurry feed and the solid content. With a higher percentages of solids, less water will be evaporated, which leads to higher throughput of dry product.

Binders for agglomeration. Suitable binder materials must be homogeneously dispersed (preferably soluble) in the liquid introduced to form the slurry. When dry, binders must form a coating and/or adhere to the material being agglomerated. They must impart the required strength and crush resistance to the granule for subsequent handling. In addition to the liquids, solids, and binders used to formulate a slurry, various other additives may be necessary. [Table 4.7](#) includes typical components of spray-dried slurries.

Plasticizers may be used with binding materials that are hard and that tend to crack during drying. Suspending agents may be needed to prevent solids from settling within the slurry. Deflocculating agents aid the formation of slurries by preventing the agglomeration of fine particles. Wetting agents also may be used to retain suspended-solid condition. Some slurries have a tendency to foam during mixing. Antifoaming agents or defoamers may be used to control this action. Chemical activators also may be used as additives to aid in subsequent sintering or processing of powders.

TABLE 4.7 Binders for Agglomeration of Spray Drying Slurries

Binder Classification	Binder
Organic binders	Polyvinyl alcohol, gum arabic, other natural gums, carboxy-methyl cellulose salts, polyvinyl acetate, methyl cellulose, ethyl cellulose, polyvinyl butyral dispersions, protein colloids, acrylic resin emulsion, ethylene oxide polymers, water-soluble phenolics, lignin sulfonates, propylene glycol alginates, flour, starches
Inorganic binders	Sodium silicate, boric acid, borax, carbonates, nitrates, oxylates, oxychlorides
Plasticizers	Glycerine, ethylene glycol, triethylene glycol, dibutyl phthalate, ethanolamines, propylene glycol, glycenol monochlorhydrin, polyoxyethylene arylether
Deflocculating agents	Sodium hexametaphosphate, sodium molybdenate, tetrasodium pyrophosphate, ammonium citrate, ammonium oxalate, ammonium tartrate, ammonium chloride, monoethylamine
Wetting agents	Synthetic detergents, alkylaryl sulfonates, alkylaryl sulfates, soaps

Water Granulation

Water granulation is a process for producing metal granules by pouring molten metals through a screen into water or by agitating molten metals into droplets with subsequent water quenching. Granulation of liquid metal offers a simple technique for solidification of metals, but pouring liquid metal into water has always been regarded as hazardous. In order to prevent a steam explosion as ignition and explosion of reactive metals like aluminum a large water tank must be used.

An improved technique called the “spinning water atomization process” (SWAP) was used for manufacturing rapidly solidified magnesium alloy granules [148]. In SWAP installation, the outlet molten through nozzle plug in crucible bottom is dispersed by gas atomizer. Molten metal particles entered in the rotatable water stream on the inner surface of chamber walls are rapidly crystallized. The magnesium alloy (6.01Al-0.26Mn-2.09Ca-0.038Si-0.004Cu-0.002Fe-0.007Zn-Mg Bal/mass%) granules are 1–5 mm size. It was previously verified that the coarse Mg powders of these sizes were noncombustible. Added data about SWAP process can be found in [chapter 17](#).

The spinning cup water granulation process [116] allows an increase of the cooling rate and a notable decrease of the size of plant, owing to cooling the molten granules in water. Thus, the chiller chamber size is only 1.2–1.5 m in diameter in comparison with 12 m in diameter in open-air granulation. A spinning cup water granulator, which was used in VILS, is shown in [Fig. 4.65](#). The cup with apertures in the walls is made from ceramics, which are nonwetttable by aluminum while possessing high resistance and low heat conductivity. The rotating disc sets the water in the atomizing chamber in rotation and under centrifugal force, the water is thrown away to the atomizing chamber walls and flows down to the overflow apertures. Thus, a mobile layer of water is formed on the inner surface housing walls. The liquid metal flows onto the rotating cup and is subjected to centrifugal force in the cup wall apertures in the form of droplets, with such droplets being force cooled by contact with the annular wall of water. The solidified granules are carried from the atomizing chamber together with the cooling water through the suspended granule discharge.

The following conventional atomization processes are used to atomize slurries for spray drying:

- Melt drop orifice atomization.
- Centrifugal (rotating disc) atomization.
- Two fluid jets atomization.

[Table 4.8](#) includes data about the size ranges of powders produced by the above atomization processes. As shown, the largest agglomerate sizes (600 μm) are achieved by melt drop orifice atomization. However, recently this agglomerate size level has been raised to 2 and 4 mm by using the impulse atomization method [130].

Applications

Spray-drying applications include the production of cemented carbides, mineral processing, the production of oxide-dispersion-strengthened alloys, and the production of powders for thermal spraying applications.

Closed-cycle spray drying is required for most cemented carbide powders because the binders that are used are soluble only in volatile organic fluids. The nitrogen drying gas that is used in the spray drying of cemented carbides is heated to

FIG. 4.65 Schematic of spinning cup water granulator.

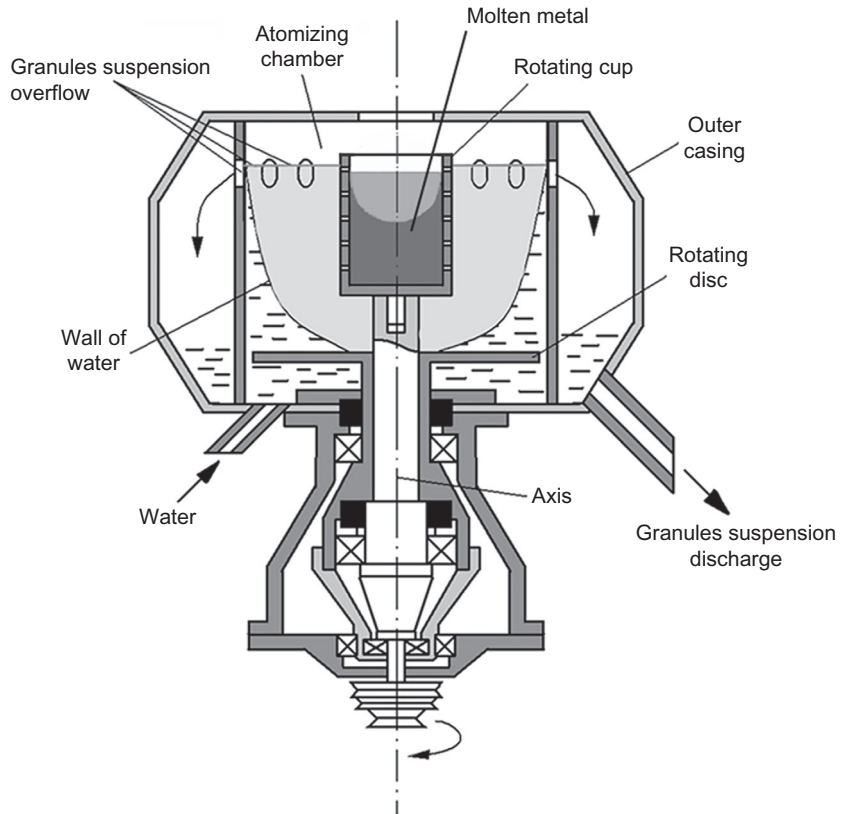


TABLE 4.8 The Size Ranges of Powders Produced by Several Atomization Processes

Atomization Method	Average Agglomerate Size (μm)
Centrifugal atomization (rotating disc)	
High speed	25–100
Medium speed	50–200
Low speed	100–300
Melt drop orifice atomization	
High pressure	25–100
Medium pressure	50–200
Low pressure	100–300
Very low pressure	200–600
Two fluid jets atomization	
High pressure	10–50
Medium pressure	25–100
Low pressure	50–200

348–373 K. Viscosity of milled slurries is sometimes modified with stabilizers such as stearic acid (0.3–0.5 wt%). Pressures for melt drop orifice atomization range from 590 to 1470 kPa. A more detailed description of this is given in [chapter 23](#).

Multicomponent oxide powders for plasma spraying is an other area of spray drying. The concept of multicomponent powders consists of two steps. The first step is the agglomeration of the starting powder by the drying process. The second

step involves plasma densification [149, 150]. The plasma-densified powder obtained has a spheroidal smooth surface, a high density, and a porosity approaching zero. Experience in this technique concerning the plasma densification of metals, metallic hard materials, and ceramics shows that the multicomponent powder concept is practicable for nearly all materials. It has been shown that coatings of plasma-densified powders show better resistance to wear than coatings of agglomerated powders.

Amastan Technologies [151] developed a powder densification/spheroidization microwave-based plasma process that improves powder flowability while increasing particle density, overall powder tap density, and purity. Its main features include axial injection of feedstock into an axisymmetric hot zone with a high and uniform profile plasma temperature, laminar gas flows, and high heating rates. The hot zone is electrode-free, which eliminates the presence of contaminants in the final product. This technique is capable for the production of uniform diameter, dense, and spherical powder particles. These droplets undergo rapid pyrolysis, followed by melting and then solidification in one step. This rapid processing could be of interest to the coating industry and other PM technologies as well, especially when uniformly sized and dense powder particles are desired.

REFERENCES

- [1] Dunkley JJ. Atomization of metals—craft or science? In: Proceedings of 2nd international conference on spray deposition and melt atomization. Bremen Universität; 2003. p. 3–11.
- [2] Hopkins WG. Hot gas atomization. In: European congress and exhibition on powder metallurgy, vol. 4. European Powder Metallurgy Association; 2001. p. 194–200.
- [3] Dunkley JJ. Atomization. In: ASM handbook, vol. 7. ASM International Publishers; 1998. p. 35–52.
- [4] Neikov OD, et al. Effect of atomization parameters on the physical properties of water atomized aluminum powders. In: Compiled by Russell A, Chernenkoff W, Brian J. Proceedings of 2014 powder metallurgy world congress. Orlando, FL, USA: Metal Powder Industries Federation; 2014, p. 02-85–94.
- [5] Neikov OD, Vasilieva GI, Sameljuk AV, Krajnikov AV. Water atomized aluminum alloy powders. *Mater Sci Eng A* 2004;383:7–13.
- [6] Seki Y, Takigawa H, Kawai N. Effect of atomization variables on powder characteristics. *Met Powder Rep* 1990;38–40.
- [7] Kikukawa M, Matsunaga S, Inaba T, Iwatsu O, Takeda T. Development of spherical fine powders by high-pressure water atomization using swirl water jet. In: Proceedings of 2000 powder metallurgy world congress. Kyoto: Japan Society of Powder and Powder Metallurgy; 2000. p. 363–6.
- [8] Terai S, Kikukawa M, Inaba T, Koyata T. Development of spherical fine powders by high-pressure water atomization using swirl water jet. In: Proceedings of 2006 powder metallurgy world congress. Korean Powder Metallurgy Institute; 2006. p. 18–9.
- [9] Russian Federation Patent 1,812,731. May 1990.
- [10] Grandzol RJ, Tallmadge JA. Water jet atomization of molten steel. *Am Inst Chem Eng J* 1973;19(6):1149–58.
- [11] Klar E, Fesko J. On the particle shape of atomized metal powders. *Prog Powder Metall* 1981;37:47–66.
- [12] Grandzol RJ, Tallmadge JA. Effect of jet angle of water atomization. *Int J Powder Metall Powder Technol* 1975;11(2):103–16.
- [13] Lawley A. Atomization. Princeton: Metal Powder Industries Federation Publishers; 2003.
- [14] Dunkley JJ. The production of metal powders by water atomization. *Powder Metall Int* 1978;10(1):38–41.
- [15] Small S, Bruce TJ. The comparison of characteristics of water and inert gas atomized powders. *Int J Powder Metall* 1968;4(3):7–17.
- [16] Levich VG. Physicochemical hydrodynamics. Moscow: Phizmatgiz Publishers; 1958 [in Russian].
- [17] Ternovoy YF, Kudyevskiy SS, Pashetneva NR. Engineering accounts of technological processes of melt metals atomization. Zaporozhye, Ukraine: Zaporozhskoy Inzhenernoy Academy Publisher; 2005 [in Russian].
- [18] Yule AJ, Dunkley JJ. Atomization of melts. Oxford: Oxford University Press Publishers; 1994.
- [19] Nichiporenko OS. Shaping of powder particles during the atomization of a melt with water. *Powder Metall Met Ceram* 1976;15(9):665–9.
- [20] Ternovoy YF. Theoretical bases of metal melt atomization processes. Zaporozhye, Ukraine: Zaporozhskoy Inzhenernoy Academy Publisher; 2008 [in Russian].
- [21] Grant NJ. The scope and trends of developments in rapid solidification technology. In: Rapidly quenched metals proceedings of the fifth international conference on rapidly quenched metals 1, Wurzburg, Germany, 1984. Elsevier Science Publishers; 1985. p. 3–34.
- [22] Mikheev MA, Mikheeva IM. Bases of heat transfer. Moscow: Energyja; 2010 [in Russian].
- [23] Kutateladze SS. Bases of theoretics of heat transfer. Athomizdat: Moscow; 2014 [in Russian].
- [24] Bechke KV, Sanin AF. Structure and properties of water-atomized aluminum powder alloy. *Powder Metall Met Ceram* 2010;49(5):266–71.
- [25] Dobatkin VI, Elagin VI, Fedorov VM. Rapidly solidified aluminum alloys. Moscow: All-Russian Institute of Light Alloys Publishers; 1995 [in Russian].
- [26] Neikov OD, Krajnikov AV, Milman YV, Thompson G, Sameljuk AV, Sirko AI, Chaykina NG. Advanced PM aluminium alloys produced by new rapid solidification technology. In: Proceedings PM2004 world congress, vol. 1. Shrewsbury, UK: European Powder Metallurgy Association; 2004. p. 237–42.
- [27] Neikov OD, Milman YV, Sirko AI, Sameljuk AV, Krajnikov AV. Elevated temperature aluminium alloys produced by water atomization. *Mater Sci Eng A* 2008;477(1–2):80–5.
- [28] Dunkley JJ. An assessment of atomization with hydrocarbon. *Met Powder Rep* 1992;22–3.

- [29] Williams B. Powder metallurgy—a global market review. In: *International Powder Metallurgy Directory & Yearbook*. 12th ed., vol. 1; 2012/2013. p. 5–16.
- [30] US Patent 1,659,291, 1917, Feb. 1928.
- [31] Wiggers H, Koster S, Walzel P. Experiments to liquid metal atomization with a new prefilming nozzle. In: *Proceedings of international conference on spray deposition and melt forming*. Bremen Universität; 2000. p. 569–78.
- [32] Dunkley JJ. *Atomization of metal powders in powder metallurgy*. Institute of Metals Publishers; 1991.
- [33] US Patent 6,481, 638, Nov 2002.
- [34] Schulz G. Concepts for a continuous operation of a WIDEFLOW gas atomizer. In: *Proceedings of 2nd international conference on spray deposition and melt atomization*, vol. 2. Bremen Universität; 2003. p. 59–66.
- [35] Ünal A. Flow separation and liquid rundown in a gas atomization process. *Metall Trans B* 1989;20B(10):613–21.
- [36] Ünal A. Influence of nozzle geometry in gas atomization of rapidly solidified aluminium alloy. *Mater Sci Technol* 1988;4:909–15.
- [37] Stobik M. Nanoval atomizing—superior flow design for finer powder. In: *Proceedings of international conference on spray deposition and melt atomization*. Bremen Universität; 2000. p. 511–20.
- [38] Germany Patent DE 102 37 213.6, August 2002.
- [39] Achelis L, Uhlenwinkel V. Characterization of metal powders generated by pressure-gas-atomizer. *Mater Sci Eng A* 2008;447(1–2):15–20.
- [40] Czisch C, Fritsching U. Atomizer design for viscous-melt atomization. *Mater Sci Eng A* 2008;477(1–2):21–5.
- [41] Tomberg C. Gas efficiency in different atomization system. In: *Proceedings powder production and spray forming*, vol. 2. Metal Powder Industries Federation; 1992. p. 127–35.
- [42] Dombrowski N, Johns WR. The aerodynamic instability and disintegration of viscous liquid sheets. *Chem Eng Sci* 1963;18:203–14.
- [43] Bradley D. On the atomization of a liquid by high velocity gases: I. *J Phys D Appl Phys* 1973;6:1724–36.
- [44] Bradley D. On the atomization of a liquid by high velocity gases: II. *J Phys D Appl Phys* 1973;6:2267–72.
- [45] Allen T. *Particle size measurement*. 3rd ed. Chapman and Hall Publishers; 1981.
- [46] See JB, Johnston GH. Interactions between nitrogen jets and liquid lead and tin streams. *Powder Technol* 1978;21:119–25.
- [47] Ingebo RD. Capillary and acceleration wave breakup of liquid jets in axial-flow airstreams. In: *NASA Technical Paper*. National Aeronautics and Space Administration, Scientific Technical Information Branch; 1981. p. 1791.
- [48] Sheichaliev SM, Sharonov IV, Karpov MP. Centrifugal-hydraulic method of powder production. *Sov Powder Metall Met Ceram* 1989;6:16–21 [in Russian].
- [49] Ternovoy YF, Pashetneva NN, Manegin YV. Physicomathematical model of the process of gas spraying of the melt jet. *Sov Powder Metall Met Ceram* 1992;3:11–5 [in Russian].
- [50] Mates SP, Biancanello FS, Ridder SD. An alternative view of close-coupled gas atomization of liquid metals. In: *Proceedings of 2002 world congress of PM and particulate materials*, vol. 3. Princeton, NJ: Metal Powder Industries Federation; 2002. p. 178–87.
- [51] Lagutkin S, Uhlenwinkel V, Achelis L, Pulbere S, Sheikhaliev S. Centrifugal Gas atomization: preliminary investigation of the method. In: *Proceedings PM 2004 World Congress*. Wien (Austria): EPMA; 2004. p. 71–6.
- [52] Ünal A. Effect of processing variables on particle size in gas atomization of rapidly solidified aluminium powders. *Mater Sci Technol* 1987;3:1029–39.
- [53] Mates SP, Ridder SD, Biancanello FS. Comparison of the supersonic length and dynamic pressure characteristics of discrete-jet and annular close-coupled nozzles used to produce fine metal powders. In: *Proceedings liquid metal atomization: fundamentals and practice*. Warrendale, PA: The Minerals, Metals and Materials Society; 2000. p. 71–81.
- [54] Ting J, Peretti MW, Eisen WB. Control of fine powder production and melt flow rate using gas dynamics. In: *Proceedings of world congress of PM and particulate materials*, vol. 2. Princeton, NJ: Metal Powder Industries Federation; 2000. p. 27–40.
- [55] Anderson IE, Terpsta RI, Figliola R. Gas recirculation flow in the melt feeding zone of a close-coupled gas atomization nozzle: modelling and measurement. In: *Proceedings of 2nd international conference on spray deposition and melt atomization*, vol. 2. Bremen: Bremen Universität; 2003. p. 19–30.
- [56] Mi J, Figliola RS, Anderson IE. A numerical investigation of gas flow effects on high pressure gas atomization due to melt tip geometry variation. *Metall Mat Trans B* 1997;28B(10):935–41.
- [57] Ting J, Peretti MW, Eisen WB. The effect of wake-closure phenomenon on gas atomization performance. *Mat Sci Eng* 2002;A326:110–21.
- [58] Ting J, Anderson IE. A computational fluid dynamic (CFD) investigation of the wake closure phenomenon. *Mat Sci Eng* 2004;A379:264–76.
- [59] Ting J. The close-coupled gas atomization: a quantitative analysis of the dynamic pressures of the pulsative atomization process. In: *Compiled by Russell A, Chernenkoff W, Brian J. Proceedings of 2014 powder metallurgy world congress*. Orlando, FL: Metal Powder Industries Federation; 2014: p. 02-76–84.
- [60] Ting J, Peretti MW, Eisen WB. Control of fine powder production and melt flow rate using gas dynamics. In: *Ferguson H, Whychell DT, editors. Advances in powder metallurgy & particulate materials*, vol. 2. Princeton, NJ: APMI-MPIF; 2000. p. 27–40.
- [61] Rieken JR, Heidloff AJ, Anderson IE, Mullis A. Development of close-coupled gas atomization process for fine metal powder production. In: *Compiled by Russell A, Chernenkoff W, Brian J. Proceedings of 2014 powder metallurgy world congress*. Orlando, FL: Metal Powder Industries Federation; 2014: p. 02-54–60.
- [62] Anderson IE, Figliola RS, Morton H. Flow mechanisms in high pressure atomization. *Mat Sci Eng* 1991;A148:101–14.
- [63] Lampa A, Fritsching U. Spray structure and propagation in confined atomization processes. In: *Uhlenwinkel V, Fritsching U, Ellendt M, editors. Proceedings of 5th international conference on spray of spray deposition and melt atomization*. Bremen, Germany: Universität Bremen; 2013. p. 1–14.
- [64] Bouffanais R. Advances and challenges of applied large-eddy simulation. *Comput Fluids* 2010;39(5):735–8.
- [65] Li D, et al. Direct numerical simulation of a particle-laden low Reynolds number turbulent round jet. *Int J Multiphase Flow* 2011;37(6):539–54.
- [66] Strauss JT. Lick back in close-coupled atomization: a phenomenological study. In: *Compiled by Russell A, Chernenkoff W, Brian J. Proceedings of 2014 powder metallurgy world congress*. Orlando, FL: Metal Powder Industries Federation; 2014: p. 02-38–45.

- [67] Mullis AM, Dunkley JJ. Analysis of acoustic emissions from gas atomisation. In: Compiled by European powder metallurgy association, Bellstone Shrewsbury, UK. Proceedings of PM 2016 world congress, Hamburg, Germany; 2016. p. 1–7.
- [68] Motaman S, Mullis AM, Cochrane RF, Borman DJ. Numerical and experimental investigations of the effect of melt delivery nozzle design on the open- to closed-wake transition in closed-coupled gas atomization. *Metall Mater Trans B* 2015;46:1990–2004. <https://doi.org/10.1007/s11663-015-0346-6>.
- [69] Gowid S, Dixon R, Ghani S. A novel robust automated FFT-based segmentation and features selection algorithm for acoustic emission condition based monitoring. *Appl Acoust* 2015;88:66–74.
- [70] Klar E, Shafer WM. High-pressure gas atomization of metals. *Powder Metallurgy for High-Performance Applications*. Syracuse, NY: Syracuse University Press; 1972.
- [71] Anderson IE, Filial R, Teresa RI, Rau S, Rauscher B. Progress in experimental analysis of gas atomization process physics. In: Proceedings of world congress of PM and particulate materials, vol. vol. 3. Princeton, NJ: Metal Powder Industries Federation; 2002. p. 150–62.
- [72] Rai G, Lavernia E, Grant NJ. Powder size distribution in ultrasonic gas atomization. *J Met* 1985;37(8):22–9.
- [73] Lubanska H. Correlation of spray ring data for gas atomization of liquid metals. *J Met* 1970;22(2):45–9.
- [74] Wigg LD. Drop-size prediction for twin-fluid atomizers. *J Inst Fuel* 1964;500–5.
- [75] Beddov JK. The production of metal powders by atomization. Philadelphia: Heyden Press Publishers; 1978.
- [76] Dunkley JJ, Telford B. Control of “satellite” particles in gas atomization. In: Proceedings of world congress of PM and particulate materials, vol. 3. Princeton, NJ: Metal Powder Industries Federation; 2002. p. 103–10.
- [77] Nichiporenko OS. On the effect of blast energy on the formation process of melt drops during atomization. *Soviet Powder Metall Ceram* 1974;6:1–7 [in Russian].
- [78] Rao P, Tallmudge JA. Change of shape of metal droplets in quench atomization. In: Proceedings of 1971 powder metallurgy conference. New York: Metal Powder Industries Federation; 1972. p. 251–8.
- [79] Zambon A, Badan B, Ramous E. Gas atomization of nickel aluminides powders. In: Proceedings PM1998 world congress, vol. 1. United Kingdom: European Powder Metallurgy Association; 1998. p. 173–8.
- [80] L'Estrada L, Hallén H, Ljunggren R. Internal porosity of gas atomized powders. In: Proceedings modern developments in powder metallurgy, vol. 20. Princeton, NJ: Metal Powder Industries Federation; 1988. p. 187–95.
- [81] US Patent 5,310,165, May, 1994.
- [82] German Patent DE 4,102,101 A1, 1991.
- [83] Pleier S, Hohmann M, Goy W, Schaub B. Actual improvements of ceramic-free metal powder production. In: Proceedings PM2004 world congress, vol. 1. Wien, Austria: European Powder Metallurgy Association; 2004. p. 89–90.
- [84] Gerling R, Schimansky FP. Crucible- and ceramic-free melting and atomization of Ti-based alloys. In: Proceedings PM 2004 world congress, vol. 1. Wien, Austria: European Powder Metallurgy Association; 2004. p. 77–82.
- [85] Yolton CF. Gas atomized titanium and titanium aluminide alloys. In: P/M in aerospace and defence technologies. Princeton, NJ: Metal Powder Industries Federation; 1989. p. 128–36.
- [86] Babun AV, Neklyudov IM, Azhazha VM, Kovtun KV, Vasiliev AA, Bobylev GG. Beryllium powder metallurgy: developments of the National Scientific Centre “Kharkov Physicotechnical Institute”. *Powder Metall Met Ceram* 2006;(3/4):118–25.
- [87] Wiggers H, Köster S, Walzel P. Experiments to liquid metal atomization with a new prefilming nozzle. In: Proceedings of SDMA 2000 international conference on spray deposition and melt atomization, vol. 2. Bremen: Bremen Universität; 2000. p. 569–78.
- [88] Reichman S, Chang DS. *Superalloys II*. John Wiley & Sons Publishers; 1987.
- [89] Lierke EG, Griesshammer G. The formation of metal powders by ultrasonic atomization of molten metal. *Ultrasonics* 1967;5:224–8.
- [90] Ruthardt R, Lierke EG. A new ultrasonic atomization technique for the production of metal powder. In: Proceedings modern developments in powder metallurgy, vol. 12. Princeton, NJ: Metal Powder Industries Federation; 1980. p. 105–11.
- [91] Rajan R, Pandit AB. Correlation to predict droplet size in ultrasonic atomization. *Ultrasonics* 2001;39:235–55.
- [92] Rayleigh JWS. *The theory of sound*. vol. 2. New York: Dover Publishers; 1945.
- [93] Barreras F, Amaveda H, Lozano A. Transient high-frequency ultrasonic water atomization. *Exp Fluids* 2002;33:405–13.
- [94] Yule AJ, Al-Suleimani Y. On droplet formation from capillary waves on a vibrating surface. In: Proceedings of the Royal Society. London; 2000. p. 1069–85.
- [95] Al-Suleimani Y, Yule AJ. A CFD prediction of wave development and droplet production on surface under ultrasonic excitation. In: Proceedings ILASS-Europe 2002; 2002. p. 9–11.
- [96] Dumouchel C, Boyaval S. Use of the maximum entropy formalism to determine drop size distribution characteristics. *Part Part Syst Charact* 1999;16:177–84.
- [97] Kapur JN. Twenty-five years of maximum entropy principle. *J Math Phys Sci* 1983;17:103–56.
- [98] Caccioppoli G, Clausen B, Bonjour C, Hofman H. Ultrasonic atomization of metallic melts: modelling and case studies. In: Proceedings of PM2004 world congress, vol. 1. Shrewsbury, UK: European Powder Metallurgy Association; 2004. p. 59–64.
- [99] Sparchez Z. Development of new procedures and devices for ultrasonic gas atomization of metallic melts using specific methods of engineering creativity. In: Proceedings of PM2004 world congress, vol. 1. Wien, Austria: European Powder Metallurgy Association; 2004. p. 25–32.
- [100] Eskin GI, Eskin DG. *Ultrasonic treatment of light alloy melts*. 2nd ed. CRC Press; 2014.
- [101] Ultrasonic atomization technology. <<http://www.sono-tek.com/ultrasonic-nozzle-technologies>> [accessed 31.01.18].
- [102] MoltenMist technology for solder paste manufacturers. <<http://www.sono-tek.com/moltenmist/>>; [accessed 31.01.18].
- [103] Dunkley JJ. Hot gas atomization—economic and engineering aspects. In: Proceedings PM2004 world, vol. 1. Wien, Austria: European Powder Metallurgy Association; 2004. p. 13–8.

- [104] Ciftcia N, Ellennda N, Mädlera L, Uhlenwinkel V. Impact of hot gas atomization on glass forming alloys. In: Compiled by European powder metallurgy association, Bellstone Shrewsbury, UK. Proceedings of PM 2016 world congress, Hamburg, Germany; 2016. p. 1–7.
- [105] Bergmann HW, Vetter J, Cai Q. Die Erzeugung von Metallpulvern durch Verdünnung ihrer Schmelzen mit flüssigen Gasen. *Steels Met Mag* 1988;26(10):985–1003.
- [106] Wolf G, Nöth M, Schubert, Martin VE, Bergmann HW. Production and characterization of liquid gas atomized hard magnetic NdFeB alloy powders for bonded isotropic magnets. In: Proceedings of the powder metallurgy world congress, vol. 3. 1994. p. 1745–53.
- [107] Wolf G, Lang A, Bergmann HW. Investigations on melt atomization with gas and liquefied cryogenic gas. In: Proceedings of international conference on spray deposition and melt forming. Bremen, Germany: Bremen Universität; 2000. p. 535–47.
- [108] Hinze H, Milborn H. Atomization of liquids by means of rotating cup. *J Appl Mech* 1950;17(2):145–53.
- [109] Tanasawa Y, Miyasaka Y, Umehara M. On the filamentation of liquid by means of rotating discs. *J Jpn Mech Soc* 1959;25(156):879–97.
- [110] Champagne B, Angers R. Fabrication of powder by rotating electrode process. *Int J Powder Metall Powder Technol* 1980;16(4):359–64.
- [111] Champagne B, Angers R. REP atomization mechanism. *Powder Metall Int* 1984;16(3):125–8.
- [112] Halada K, Suga H. Theoretical investigation on parameters of centrifugal atomization of metal powder. *Powder Powder Metall* 1990;37(4):492–9 [in Japanese].
- [113] Matsumoto S, Saito K, Takashima Y. Disintegration modes of centrifugal atomization. *J Eng Japan* 1974;7(1):13–5.
- [114] Angers R, Dube C, Tremblay R. Inverted disk centrifugal atomization of 2024. *Int J Powder Metall* 1994;30(44):429–34.
- [115] Dunkley JJ, Aderhold D. Centrifugal atomization of metal powders. In: Proceedings of international conference on spray deposition and melt forming. Bremen, Germany: Bremen Universität; 2006. p. 1–6.
- [116] Bondarev BI, Shmakov YV. Technology of rapidly solidified Al alloy production. Moscow: All-Russian Institute of Light Alloys Publishers; 1997 [in Russian].
- [117] Sheikhaliev S, Moscvitin V, Zibin V, Sheikhalieva Z, Dunkley JJ. Characterization of metal powder production by a pressure-centrifugal-atomizer. In: Proceedings of 2nd international conference on spray deposition and melt atomization. Bremen, Germany: Bremen Universität; 2009. p. 3–11.
- [118] US Patent 4,343,750, August 10, 1982.
- [119] Pan SV, Slypenyuk OM, Kuprin VV, Milman YV, Troy Tacke V. Influence of scandium concentration on structure peculiarities and hardness of the rapidly-quenched Al–Sc alloys. *Met Phys Adv Technol* 1999;18:452–5.
- [120] Hitoshi O, Takashi O, Nobuyuki I, Motonori N. Development of safe production system for Mg–Zn–Re rapidly solidified powders. In: Proceedings of PM2004 world congress, vol. 1. Wien, Austria: European Powder Metallurgy Association; 2004. p. 111–5.
- [121] Kawamura Y, Inoue A. Rapidly solidified powder metallurgy Mg₉₇Zn₁Y₂ alloys with tensile yield strength of 610 MPa and elongation of 5%. In: Kaplan HI, editor. Magnesium technology. TMS (The Minerals, Metals & Materials Society); 2002. p. 2002.
- [122] Kawamura Y, Inoue A, Masumoto T. Mechanical properties of amorphous alloy compacts prepared by a closed processing system. *Scripta Metall Mater* 1993;29:25–30.
- [123] US Patent 3,099,041, July, 1963.
- [124] US Patent 3,802,816, April, 1974.
- [125] Liles DT, Deleeuw DC. Rapid solidification via centrifugal atomization with a volatile liquid coolant. In: Das SK, Kear BH, Adam CM, editors. Proceedings rapidly solidified crystalline alloys. Warrendale, PA: The Metallurgical Society; 1985. p. 285–90.
- [126] US Patent 4,347,199, August, 1985.
- [127] US Patent 4,419,060, December, 1983.
- [128] Naida YI, Stepanchuk AN, Naida AY. Industrial production of copper alloys powders using impact atomization method. *Powder Metall Met Ceram* 2006;(1/2):112–7.
- [129] Matei G, Bicsak E, Huppmann WJ, Claussen N. Atomization of metal powders using the vibrating electrode method. In: Proceedings modern development in powder metallurgy, vol. 9. Metal Powder Industries Federation; 1977. p. 153–60.
- [130] Henein H. Impulse atomization: as innovative approach for the generation of powders and spray deposits. In: Proceedings of 2nd international conference on spray deposition and melt atomization, vol. 1. Bremen: Bremen Universität; 2003. p. 31–9.
- [131] Khatibi PD, Henein H. In-situ measurement of droplet size, velocity and temperature in a drop tube-impulse system. In: Uhlenwinkel V, Fritsching U, Ellendt M, editors. Proceedings of 5th international conference on spray of spray deposition and melt atomization. Bremen, Germany: Universität Bremen; 2013. p. 1–13.
- [132] Aldinger F, Linck L, Claussen N. A melt drop technique for the production of high-purity metal powder. *Mod Dev P/M* 1977;9:141–51.
- [133] Yim P, et al. Production and characterisation of mono-sized Sn38Pb alloy balls. *Int Metall Powder Technol* 1996;32(2):155–64.
- [134] Kawasaki A, Watanebe R. Preparation of monosized spherical particles of metals and alloys by POEM process. In: Proceedings of 2002 world congress of PM and particulate materials, vol. 3. Princeton, NJ: Metal Powder Ind. Fed; 2002. p. 96–102.
- [135] Singer ARE, Roche AD, Day L. Atomization of liquid metals using twin roller technique. *Powder Metall* 1980;(2):81–5.
- [136] Smagorinski ME, Tsantrizos PG. Production of spherical titanium powder by plasma atomization. In: Proceedings of 2002 world congress of PM and particulate materials, vol. 3. Orlando, FL: Metal Powder Industries Federation; 2002. p. 248–60.
- [137] Advanced powders & coatings. Division of Raymor Industries Inc. <www.raymor.com>. [accessed 31.01.18].
- [138] Teoh WY, Amal R, Madler L. Flame spray pyrolysis: an enabling technology for nanoparticles design and fabrication. *Nanoscale* 2010;2(8):1324–47.
- [139] Furuya M, Arai T. Innovative ultra rapid cooling and atomizing process utilizing vapor explosion and production of new functional powders. Compiled by European powder metallurgy association, Bellstone Shrewsbury, UK. In: Proceedings of PM 2010 world congress, Florence, vol. 1. 2010. p. 33–8.
- [140] Wegner K, et al. Pilot plants for industrial nanoparticle production by flame spray pyrolysis. *Kona Powder Part J* 2011;29:251–65.

- [141] Meierhofer F, et al. Investigation of atomization concepts for large-scale nanoparticle production by flame spray pyrolysis (FSP). In: Uhlenvinkel V, Fritsching U, Ellendt M, editors. Proceedings of 5th international conference on spray of spray deposition and melt atomization. Bremen, Germany: Universität Bremen; 2013. p. 1–13.
- [142] Mueller R, Jossen R, Pratsinis SE, Watson M, Akhtar MK. Zirconia nanoparticles made in spray flames at high production rates. *J Am Ceram Soc* 2004;87(2):197–202.
- [143] Mädler L, Kammler HK, Mueller R, Pratsinis SE. Controlled synthesis of nanostructured particles by flame spray pyrolysis. *J Aerosol Sci* 2002;33(2):369–89.
- [144] Wegner K, et al. Pilot plants for industrial nanoparticle production by flame spray pyrolysis. *Kona Powder Part J* 2011;29:251–65.
- [145] Meierhofer F, et al. Investigation of atomization concepts for large-scale nanoparticle production by flame spray pyrolysis (FSP). In: Uhlenvinkel V, Fritsching U, Ellendt M, editors. Proceedings of 5th international conference on spray of spray deposition and melt atomization. Bremen, Germany: Universität Bremen; 2013. p. 1–13.
- [146] Tsukada M, Goto K, Yamamoto RH, Horio M. Metal powder granulation in a plasma-spouted/fluidized bed. *Powder Technol* 1995;82(3):347–53.
- [147] Prem H, Eddington DJ. Contamination-free processing of pyrophoric rare earths and abrasive ceramic powders. *Powder Handl Process* 1989;1(1):101–7.
- [148] Jones T, Kondoh K. Ballistic analysis of new military grade magnesium alloys for armor applications, *Magnesium technology*. TMS (The Minerals, Metals and Materials Society); 2011. p. 425–30.
- [149] Luo P, Strutt PR, Xiao TD. Synthesis of chromium silicide–silicon carbide composite powders. *Mater Sci Eng B* 1993;17(1–3):126–30.
- [150] Lugscheider E, Loch M, Suk HG. Powder technology—state of the art. In: Proceedings of thermal spray: int. advances in coatings technology. ASM international; 1992. p. 552–9.
- [151] Hadidi K, Redjda M. Powder densification and spheroidization using an axisymmetric microwave generated plasma. In: Conference paper of Aeromat 25 conference and exposition American Society for Metals. 2014. <https://www.researchgate.net/publication/267901747_Powder_Densification_and_Spheroidization> [accessed 31.01.18].

FURTHER READING

- [152] Levis GC, et al. Atomization of liquids in high velocity gas streams. *Ind Eng Chem* 1948;40(1):67–74.
- [153] Ünal R. Effect of the pressure formation at the tip of the melt delivery tube in close-coupled nozzles in gas atomization process. In: Proceedings of 2006 powder metallurgy world congress. Busan, Korea: Korean Powder Metallurgy Institute; 2006. p. 562–3.
- [154] Liu Y, Guo S, Huang B, Liu Z, Du Y. Densification behaviour of Al-Ni-Y powder containing amorphous and nanocrystalline phases. In: Proceedings PM2004 world congress, vol. 1. Wien, Austria: European Powder Metallurgy Association; 2004. p. 425–30.
- [155] Capes CE. Particle size enlargement. In: Handbook of powder technology. Elsevier Scientific Publishers; 1980.